

**UNIVERSITÀ DEGLI STUDI DI NAPOLI  
“FEDERICO II”**



**Scuola Politecnica e delle Scienze di Base  
Area Didattica di Scienze Matematiche Fisiche e Naturali**

**Dipartimento di Fisica “Ettore Pancini”**

*Laurea Magistrale in Fisica*

**Decoherence in superconducting qubits: measurements  
and analysis of coherence times in transmon devices**

**Relatori:**

Francesco Tafuri  
Davide Massarotti  
Halima Giovanna Ahmad

**Candidato:**

Francesca D’Esposito  
Matr. N94000714

**Anno Accademico 2021/2022**

# Contents

<b>1</b>	<b>Introduction</b>	<b>3</b>
<b>2</b>	<b>Superconducting qubits</b>	<b>6</b>
2.1	Qubits and DiVincenzo criteria . . . . .	6
2.2	Superconductors . . . . .	8
2.3	Josephson effect . . . . .	10
2.4	SQUID and flux quantization . . . . .	14
2.5	Circuit Quantum Electrodynamics . . . . .	17
2.6	A charge-noise protected qubit: the transmon . . . . .	21
2.7	Tunability and Control . . . . .	23
2.8	Readout . . . . .	26
2.9	Coupled qubits . . . . .	28
<b>3</b>	<b>Noise and decoherence in superconducting qubits</b>	<b>31</b>
3.1	Bloch-Redfield model for noise . . . . .	31
3.2	Noise power spectral density . . . . .	33
3.3	Effect of noise sources in superconducting qubit relaxation . . . . .	36
3.4	Effect of noise sources in superconducting qubit dephasing . . . . .	41
3.5	Summary . . . . .	46
<b>4</b>	<b>Experimental setup</b>	<b>48</b>
4.1	Chip design . . . . .	48
4.2	Dilution refrigerator . . . . .	50
4.3	Electronics and measurement protocols . . . . .	54
4.3.1	Cryogenic electronic setup . . . . .	54
4.3.2	Room temperature electronics setup . . . . .	56
4.3.3	Spectroscopy measurements . . . . .	58
4.3.4	Time domain measurements . . . . .	63
<b>5</b>	<b>Measurements and data analysis</b>	<b>68</b>
5.1	Spectroscopy measurements . . . . .	68
5.1.1	Readout resonator spectroscopy . . . . .	68
5.1.2	Qubit spectroscopy . . . . .	72
5.2	Time evolution measurements . . . . .	76
5.2.1	Rabi oscillations . . . . .	76
5.2.2	Relaxation time . . . . .	78
5.2.3	Ramsey interferometry . . . . .	80
5.2.4	Hahn Echo . . . . .	82

5.3	Avoided level crossing as noise spectroscopy . . . . .	85
<b>6</b>	<b>Conclusions</b>	<b>89</b>

# 1 Introduction

Today, quantum computers are gaining more and more popularity in the scientific community. One of the reasons of this strong interest is their ability to solve hard problems which could not be solved by classical computers (in reasonable times) [1]. Some examples of these problems are the study of large molecules for medical applications [2], the prime factorization of large numbers [3], which is largely used by modern cryptography [4], and finally financial systems modelling [5].

The operations of a quantum computers are based on Quantum Mechanics (QM). This is a very interesting aspect because, by studying a qubit, we are able to inspect the behaviour of a quantum two-level system, such as an atom, and observe its behaviour. Thus, quantum computation is also an inspiring platform where to test fundamental notions of QM and where to test the most advanced protocols of information technology.

One of the greatest challenges in realizing quantum computers is controlling and fighting decoherence. According to QM, a quantum object is described by a wavefunction, which is characterized both by a density of probability and a phase [6]. This description introduces a series of quantum phenomena, such as interference and entanglement, the very essence of quantum physics. However, the system can undergo through dephasing if exposed to an external perturbation [7]. Moreover, a quantum system may be very sensitive to environmental noise and can easily switch between the ground and excited states by adsorption or emission. As a matter of fact, any interaction between a quantum system and the external world can introduce a perturbation and destroy the coherence. Because of these, scientists are trying to find a good candidate for engineering qubits whose coherence times are sufficiently longer than the desired computational times.

In particular, today's most studied quantum computers are based on superconducting quantum processors. The superconducting quantum computer is currently the only one able to operate with more than 100 qubits [8], [9]. The outstanding result of such devices is the possibility to control the quantum state of the qubit by tuning the circuit parameters by means of macroscopic quantities, like the voltage, the current, the magnetic flux. Moreover, the reduction of decoherence sources for each qubit allows an overall enhancement of the control of the computer architecture, which is a mandatory step towards scalability [9].

All superconducting qubits are based on the Josephson effect [10], in this thesis we will consider the most common one: the transmon [11]. Since superconducting qubits are based on solid state circuits, the sources of decoherence are also determined by the control electronics and the intrinsic properties of the materials. Typical noise sources are the coupling with the readout and control circuits, the charge offset in the Josephson junctions (JJs), which are the building elements of

the transmon qubit, the dielectric losses in the substrate. By changing the qubit design, the scientists tried to suppress one or more decoherence channels in order to enhance coherence times. The transmon qubit reduces decoherence induced by charge offset noise, as will be discussed in this work.

In chapter 2, we will describe the basic principles of superconducting qubits. After having introduced the concept of quantum bit and the basic requirements for quantum computation (section 2.1), we will describe the phenomenology of superconductors, in section 2.2, and the Josephson effect, in section 2.3. A special focus will be given to the phenomenon of flux quantization and its manifestation in the SQUIDs (section 2.4), which are fundamental for tuning and control of most qubits. In section 2.5, we will demonstrate that a superconducting qubit with a JJ can be described by a QM model, based on the circuit Quantum Electrodynamics. We will introduce the transmon qubit circuit and its main features (section 2.6), and point out how to tune its parameters through an external flux bias (section 2.7). In order to perform quantum algorithms, we must be able to initialise and control the qubit state, as discussed in section 2.7. As in any classical computer, it is mandatory to read and write the qubit state, but, according to QM, measuring the state of a quantum system implies its destruction. Therefore, in section 2.8, we will describe how to perform Quantum Non Demolitive measurements. We will also study the coupling between two qubits (section 2.9), which is the basic request for quantum computation.

In chapter 3, we will discuss noise and decoherence for a single tunable transmon qubit. In view of the final target of understanding the principal sources of decoherence in such systems, providing a self-consistent method for the identification of these sources in real qubits measurements. We will use the Bloch-Redfield model for noise in a two level system, and the noise power spectral density as a fingerprint of its behaviour and effect. We will focus on the energy relaxation processes in section 3.3, and on the dephasing channels in section 3.4, then summarized in section 3.5, respectively.

Afterwards, in chapter 4, we will describe the experimental setup. We will start from the design of the multi-qubit measured in this work (section 4.1), then we will focus on the dilution cryostat (section 4.2), and the electronics at cryogenic temperatures 4.3. In section 4.3.2, we will give an overview on the room temperature electronics used for qubit measurements. The principal protocols for qubit characterization are reported in section 4.3.3. We will give a particular focus on the time evolution measurements (section 4.3.4), which allow evaluating the coherence times of the qubit, i.e. the relaxation and dephasing rates.

Finally, in chapter 5, we will report the measurements and the analysis performed in this work. In sections 5.1.1 and 5.1.2, we will measure the characteristic parameters of two coupled split-transmon qubits, as well as their readout resonators.

Then, in section 5.2, we will focus on the time evolution of our systems by performing the Rabi protocol (section 5.2.1). In order to understand the contribution to decoherence of the noise sources previously described, we will compare the experimental relaxation time, in section 5.2.2 with the decoherence times simulated with the Python library *scqubits* [12]. This package is based on the noise analysis reported in section 3.1. Then, by observing the Ramsey fringes measured in section 5.2.3, we will give a first estimation of the dephasing time of the qubits. Thanks to the Hahn Echo protocol (section 5.2.4), we will measure the coherence times of the two qubits. By comparing the experimental results with *scqubits* [12] simulations, we will provide a self-consistent evaluation of the flux noise amplitude, and the resulting theoretical dephasing time.

In section 5.3, we will report on two-qubits coupling measurements, thus demonstrating that as the coupling became relevant, novel noise sources arise when the two qubits enter an entangled state.

## 2 Superconducting qubits

### 2.1 Qubits and DiVincenzo criteria

Quantum bits, or qubits, are a unit of computational information, based on a quantum two-level system, with eigenstates  $|0\rangle$  and  $|1\rangle$  [13]. The state  $|0\rangle$  is called ground state, while  $|1\rangle$  is the excited state. Unlike classical bits, which are binary systems where the information is encoded in just two possible values, for qubits the quantum superposition is a powerful way to encode the information in a quantum state of the type [7]:

$$|\psi\rangle = \alpha |0\rangle + \beta |1\rangle, \quad |\alpha|^2 + |\beta|^2 = 1. \quad (1)$$

Indeed, the main difference between classical computers and quantum processors is that, because of the probabilistic nature of QM, qubits allow for an infinite superposition of the two states  $|0\rangle$  and  $|1\rangle$ , thus making quantum computation much more efficient than the classical one.

A qubit can be represented as a vector on the Bloch sphere in figure 1, where the Dirac notation is used as a set of orthonormal basis [13], [7]:

$$|0\rangle \equiv \begin{pmatrix} 1 \\ 0 \end{pmatrix} \quad |1\rangle \equiv \begin{pmatrix} 0 \\ 1 \end{pmatrix}. \quad (2)$$

In this representation, a generic state of the qubit is a point of the Bloch sphere,

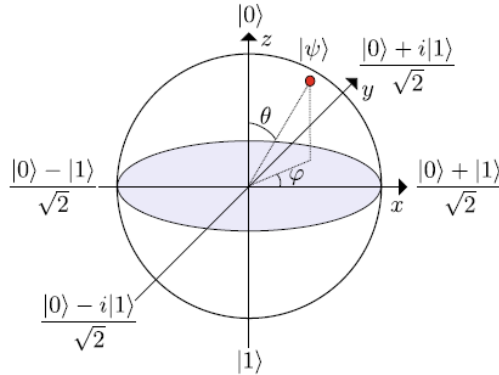


**Figure 1:** Bloch sphere representation: the generic quantum state  $|\phi\rangle$  is a point on the sphere with coordinates  $\phi$  and  $\theta$  [13]

defined by a combination of  $|1\rangle$  and  $|0\rangle$ :

$$|\psi\rangle = \cos \frac{\theta}{2} |0\rangle + \sin \frac{\theta}{2} e^{i\phi} |1\rangle, \quad (3)$$

where the angles  $\theta$  and  $\phi$  define the position on the Bloch sphere. The ground state  $|0\rangle$  corresponds to the North Pole while the excited state  $|1\rangle$  is the South Pole.

In 1996–2000, scientists questioned what basic criteria the qubit had to satisfy in order to work and to build a quantum computer [1], [13]. In particular, coherence, isolation from the environment and ability to control the qubit state with an external degree of freedom became the most interesting topics in the field. The theoretical physicist DiVincenzo proposed a list of requirements necessary to build a quantum computer [13], [1]. Firstly, it must be possible to fabricate registers with several qubits, i.e. the qubits must be scalable. As in a classical computer, it must be possible to read the state of the qubit. As will be discussed in section 2.8, it is not a simple request because it is often required to measure the qubit state without destroying it, but from the QM principles, any measure of a quantum object will make it collapse. Because of this, it is mandatory to find an indirect way to measure the qubit state, also known as Quantum Non Demolitive Readout, which will be discussed in section 2.8. In order to control the qubit state, it must be possible to initialise it. Moreover, the requirement for quantum algorithms, makes mandatory to implement multi-qubits gates with a high fidelity. Finally, in order to be able to implement several single and two qubits gates, the coherence time of our system must exceed the duration of a large number of gates. One of the main problems that the scientists had to face in order to build a quantum computer, in fact, was finding a compromise between the need to use a quantum two-level system, such as an atom, a very sensitive object, with the fundamental requirement to easily control and readout its state, and the difficulties of maintaining it coherent during these processes.

Superconducting qubits, and in particular JJs-based qubits, satisfy these criteria to a reasonable degree. First, superconducting qubits chips are based on solid state physics and semiconductors technology, just as the processors used in classical computers. This make superconducting qubits easy to fabricate and to scale up. Moreover, the circuital nature of these systems allows for a practical way to manipulate and read the qubit state, thus giving the possibility to implement actual quantum gates [7].

In section 2.2 and 2.3 we will point out the most important properties of superconductors and why they are so useful to build a quantum computer. We will

discuss under which circumstances a superconducting circuit can be exploited to build a computational space, and can be studied with a QM model through the circuit Quantum Electrodynamics (section 2.5). After having introduced the transmon qubit in section 2.6, which will be characterized in this thesis, in section 2.7, we will demonstrate that a superconducting qubit can be controlled and initialized with a drive signal, while in section 2.8, we will study a way to read the state of the qubit without destroying it, by coupling it with a readout resonator. Moreover, since a two-qubit coupling is required in future computational applications, we will also show a way to implement it and observe energy exchange between two qubits, in section 2.9.

## 2.2 Superconductors

Superconductors are special materials, which manifest particular macroscopic effects when they are cooled below a critical temperature  $T_C$ , like zero resistance and perfect diamagnetism [10], [14]. This means that below  $T_C$ , DC electrical resistance is experimentally zero, as we can see in figure 2 (a), and the external magnetic field, is completely expelled below a certain critical magnetic field threshold. This second phenomenon is called Meissner effect, and it is described in figure 2 (b). Critical temperatures of superconductors largely employed in quantum circuits,

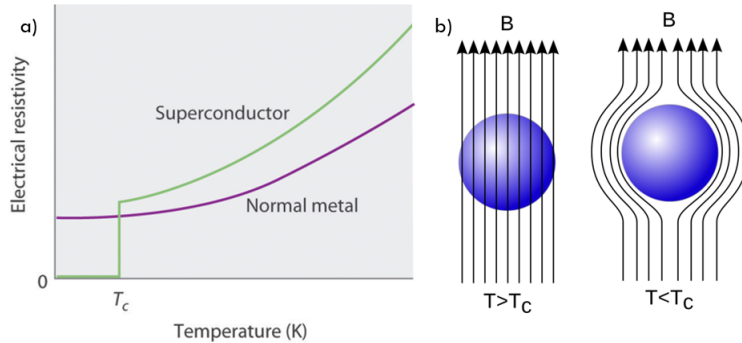


**Figure 2:** Empirical properties of superconducting materials. a) The electrical resistivity as a function of the temperature for a superconductor (green) and a normal metal (purple). Above the critical temperature  $T_c$  of the superconductor, the electrical resistivity follows an ohmic behaviour, while for  $T < T_c$  it abruptly goes to zero. b) Pictorial representation of the Meissner effect: in the superconducting state ( $T < T_c$ ), the magnetic field  $B$  is completely expelled from the superconductor.

like Aluminium or Niobium compounds, range from 1 K to 10 K, respectively. Superconductors can be described microscopically by the Bardeen-Cooper-Schrieffer theory [15]. At sufficiently low temperature, electrons near the Fermi surface become unstable and tend to form correlated pairs called Cooper pairs, cou-

ples of electrons in a singlet state, with an effective mass  $m^* = 2m_e$  and charge  $e^* = 2e$  [15]. This behaviour occurs because there is an attraction between the electrons in the pair that is able to overcome Coulombian repulsion. Cooper pairs behave like bosons, i.e. they can form a Bose-Einstein condensate below  $T_C$ . They are described by [14], [15]:

$$|\psi\rangle_{\text{BCS}} = \prod_k \left( u_k + v_k e^{i\theta_k} c_{k\uparrow}^\dagger c_{-k\downarrow}^\dagger \right), \quad (4)$$

where  $c_{k\uparrow}^\dagger$  and  $c_{-k\downarrow}^\dagger$  are the creation operators of the electrons,  $u_k$  and  $v_k$  are the probabilities to form or not a Cooper pair, related by the equation [15][14]:

$$u_k v_k = \frac{1}{2} \frac{E_k}{\Delta_k}. \quad (5)$$

Here  $\Delta_k$  is the superconductors' energy gap and  $E_k$  is the single-particle excitation energy [15], [14]:

$$E_k = \sqrt{\Delta_k^2 + \xi_k^2}, \quad (6)$$

where  $\xi_k$  is the energy of the non-interacting electrons. The energy gap in the excitation spectrum in equation 4 can be rewritten as a function of the temperature as [15], [14]:

$$\Delta_k = - \sum_l v_{kl} \frac{\Delta_l}{2E_l} \tanh \frac{E_l}{2k_B T}. \quad (7)$$

This means that if the energy of the system is lower than the energy gap  $\Delta$ , single-

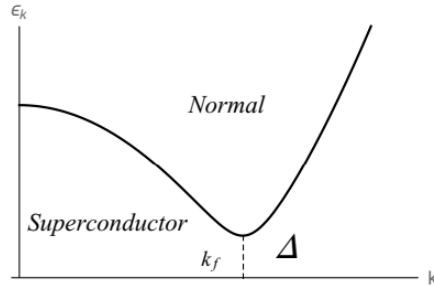


**Figure 3:** Single-particle excitation spectrum of a Bardeen-Cooper-Schrieffer superconductor: if single-particle energy  $\epsilon_k$  is below the superconducting energy gap  $\Delta$ , the system is superconducting.

particle excitations are forbidden and electrons remain in the condensate [15], [14]. Therefore, if a current of Cooper pairs is induced, there is no voltage drop across the system, i.e. below  $T_C$  the resistance of the superconductor is zero, and there is

no ohmic dissipation. On the contrary, if the energy overcomes this gap, single-particle excitations are allowed.

Superconductivity can also be described as a critical phenomenon, as discussed in the Ginzburg-Landau (GL) theory [14]. It derives from Landau's theory of second order phase transitions, in which the free energy  $F$  near the transition is expressed in terms of an order parameter. In the GL theory, the order parameter is the superconducting wavefunction:

$$\psi = |\psi| e^{i\phi}, \quad (8)$$

where  $|\psi|^2$  is the density of superconducting particles and  $\phi$  is the superconducting phase. The important result of this theory is that we can access QM properties like the wavefunctions with macroscopic parameters, such as the density of Cooper pairs and the macroscopic phase of the superconductor [14]. Starting from this expression, we can derive other properties of superconductors, such as the Josephson effect, described in section 2.3, and the flux quantization, as discussed in section 2.4.

### 2.3 Josephson effect

The Josephson effect is a macroscopic quantum phenomenon that occurs when two superconductors are separated by a thin barrier of around 1 nm [10] (figure 4). The current through the junction depends on the phase difference of the superconductors. The two Josephson equations are [10]:

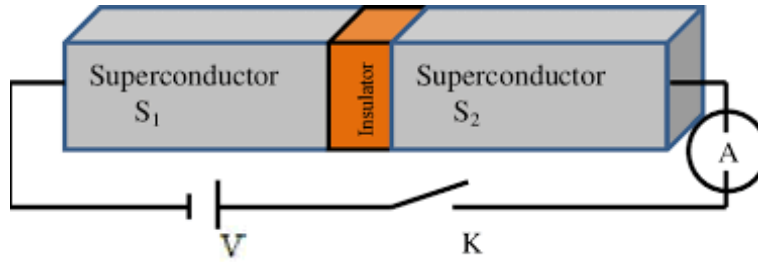


**Figure 4:** Schematic representation of a JJ: the superconducting electrodes,  $S_1$  and  $S_2$  in grey, are separated by an insulating barrier, in orange. Both electrodes are connected to an external conventional circuit, represented by a voltage multimeter V and a current generator A [16].

$$I_S(t) = I_C \sin \phi, \quad (9)$$

$$\frac{\partial \phi}{\partial t} = \frac{2eV(t)}{\hbar}, \quad (10)$$

where  $\phi = \phi_1 - \phi_2$  is the difference between the two macroscopic phases of the superconductors, while  $V(t)$  is the potential across the junction. The first equation 9 states that the superconducting current is nonlinear as a function of the superconducting phase difference. When current-biasing the Josephson junction (JJ) with a current  $I > I_C$ , namely the critical current, a voltage appears across the junction, while for  $I < I_C$  it becomes superconducting [10].

Equation 10 states that the time evolution of the phase difference is linked to the voltage. We observe that if the phase is constant,  $V = 0$  and the non-dissipative behaviour is confirmed.

By applying the chain rule to the second Josephson equation, 10, we obtain:

$$\frac{\partial I}{\partial t} = \frac{\partial \phi}{\partial t} \frac{\partial I}{\partial \phi} = \frac{2eV(t)}{\hbar} I_C \cos \phi, \quad (11)$$

i.e. the junction is a non-linear inductance:

$$L(\phi) = \frac{L_J}{\cos \phi}, \quad (12)$$

where:

$$L_J = \frac{\hbar}{2eI_C}. \quad (13)$$

We can describe a Josephson junction with several models, like the tunnel junction microscopic (TJM [17]) model or the Resistively Capacitance Shunted Junction (RCSJ model [17]), according to which we can associate the junction with a circuit like the one in figure 5. The Josephson junction can be seen as a non-linear inductor in parallel with a parallel plate capacitance  $C$ , which forms due to the presence of a non-superconducting barrier between the two superconducting electrodes. The resulting charge energy will be:

$$E_C = \frac{e^2}{2C}. \quad (14)$$

At the same time, the resistance  $R$  in the circuit 5 is due to an ohmic and dissipative term, which relates to the formation of the so-called quasiparticles in the junctions. Depending on the interplay between capacitive and dissipative elements in the junctions, we can distinguish between different transport regimes fundamental for the understanding of the main noise sources in Josephson devices [10]. If the junction is current-biased, from the circuit in figure 5 we obtain [17]:

$$I = I_C \sin \phi + \frac{V}{R} + C \frac{dV}{dt}. \quad (15)$$

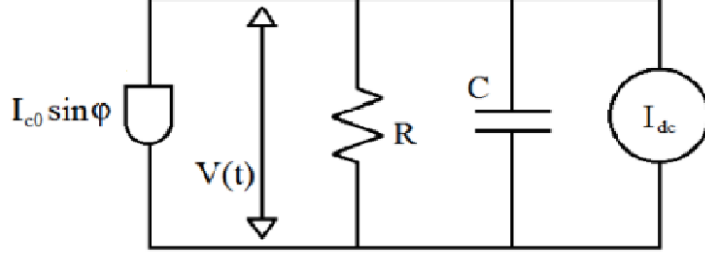


**Figure 5:** Current-biased Josephson junction equivalent circuit scheme according to the Resistively and Capacitively Shunted Junction model [10], whose elements are: the Josephson current  $I_{C0}$ , resistance  $R$ , capacitance  $C$  and bias current  $I_{dc}$

If we use the second Josephson equation 10 for the voltage, the circuit equation describes the phase dynamics, and reads as:

$$C \left( \frac{\phi_0}{2\pi} \right)^2 \frac{\partial^2 \phi}{\partial t^2} + \frac{1}{R} \left( \frac{\phi_0}{2\pi} \right)^2 \frac{\partial \phi}{\partial t} + \frac{\partial U}{\partial t} = 0, \quad (16)$$

where the potential  $U$ , known as washboard potential, describes the energy stored in the junction [18] (figure 6):

$$U = -E_J \left( \cos \phi + \frac{I}{I_C} \phi \right), \quad (17)$$

with

$$E_J = \frac{\hbar}{2e} I_C, \quad (18)$$

is the energy associated to the junction, called Josephson energy.

The capacitance  $C$  is related to the inertia of a particle associated to the phase difference  $\phi$ . The motion of the phase particle along the washboard potential determines the state of the junction: resistive and superconducting, depending on the ratio  $\alpha = \frac{I}{I_C}$ . If the bias current is small compared to the critical current ( $\alpha < 1$ ), the phase of the junction is trapped in a potential minimum and the state is superconducting. For  $\alpha > 1$ , the washboard potential will bend and let the phase escape from the well, so the regime will be resistive [10].

These escaping events also occur stochastically for bias-currents  $I$  close to  $I_C$ , but not necessarily larger ( $I \lesssim I_C$ ), induced by both Macroscopic Quantum Tunnelling (MQT) of the phase and thermal fluctuations [17], [10], and represent a noise

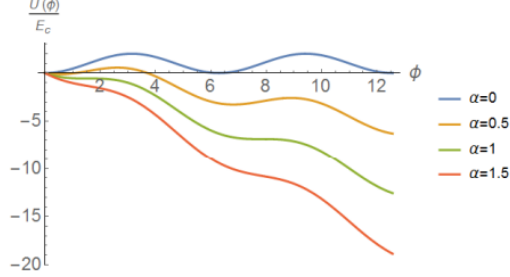


**Figure 6:** Washboard potential: as the ratio  $\alpha = I/I_C$  increases, the potential starts to bend and the phase can escape from the well, determining the voltage state. On the contrary, if the phase remains trapped in a minimum of the potential energy, the junction is in the superconducting state [17].

source for the junction.

In order to characterize dissipative effects in a Josephson junction, we introduce the dimensionless Stewart-McCumber parameter [10]:

$$\beta_J = \frac{1}{\omega_J RC}, \quad (19)$$

where:

$$\omega_J = \frac{1}{\sqrt{L_J C}}, \quad (20)$$

is the plasma frequency of the circuit, i.e. the oscillation frequency of the phase-particle in the superconducting state on the washboard potential. For  $\beta \gg 1$ , i.e. for metallic-like barriers with small capacitance, we are in the so called overdamped regime. For large capacitance,  $\beta \ll 1$  and we are in the underdamped regime. As a matter of fact, the Stewart-McCumber parameter is strictly connected to the quality factor of the circuit as  $\beta = \frac{1}{Q^2}$ . In qubit circuits, underdamped Josephson junctions are a strong requirement because their quality factor is larger compared to overdamped junctions. This guarantees lower dissipation related to quasiparticles formation, and reasonable coherence times [11] (section 3.1).

Quasiparticles currents can be generated by means of two main mechanisms: i) thermal breaking of Cooper pairs for thermal energies  $k_B T > \Delta_1 + \Delta_2$ , where  $\Delta_1$  and  $\Delta_2$  are the energy gaps of the superconducting electrodes in the junction; ii) high-energy  $eV > \Delta_1 + \Delta_2$ . While most of Josephson-based superconducting quantum circuits, such as qubits, are operated at temperatures much smaller than the superconducting gap electrodes, quasiparticles can still arise because of point ii). An experimental footprint able to quantify the quasiparticles dissipation is the IV curve of the JJ, shown in figure. 7. By current-biasing a JJ with a current

$I > I_C$ , the IV curve follows a standard ohmic behaviour with normal resistance  $R_N$  [10], [17]. Therefore, the dissipation can be quantified in terms of the ohmic parameter  $R_N$ . However, by ramping the bias current below  $I_C$ , it is still possible to recover a finite voltage across the device. This indicates the presence of dissipative quasiparticles term that strongly depends on the shape of the IV curve below the superconducting gap (subgap region with resistance  $R_{subgap}$ ) [10]. Specifically speaking, the subgap IV curve shape is intrinsically related to the barrier charging energy. In the case of overdamped junction, the path from superconducting

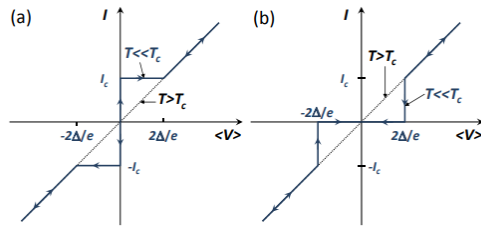


**Figure 7:** Josephson current for a JJ with two identical superconductors ( $\Delta_1 = \Delta_2 = \Delta$ ): in a) we highlight the transition (in blue) from superconducting to ohmic states, in b) from ohmic back to superconducting (in blue). In black, we can see the normal ohmic I-V characteristic for a metallic junction, recovered for  $T > T_c$ .

to ohmic states, and back, is not hysteretic, thus the only dissipative contribution comes from the  $R_N$  value. For underdamped junctions, we observe hysteresis in the IV characteristics curve. This means that if the system goes from superconducting to ohmic states, the main dissipative contribution is given by  $R_N$  (figure 7 (a)). On the other hand, when it returns to the superconducting state, the dissipation is quantified by means of the subgap resistance (figure 7 (b)). The larger is the resistance of the dissipative quasiparticles channel, the smaller will be the probability for quasiparticles to induce tunnelling currents across the junction, and as a consequence dissipation in the system. As a matter of fact, JJs in superconducting qubits are typically required to have large subgap resistances [19], [20], [10].

## 2.4 SQUID and flux quantization

A superconducting loop with two JJs is called superconducting quantum interference device (SQUID) [10]. If a SQUID is exposed to a perpendicular magnetic field, the flux  $\Phi$  through the loop area is quantized. This behaviour is known as flux quantization. By applying the properties of zero resistance and perfect diamagnetism, we found that the magnetic flux calculated on a closed loop in a super-

conductor is a multiple of a flux quantum [14], [10]:

$$\Phi_S(B) = \int \mathbf{B} \cdot d\mathbf{S} = \int \nabla \times \mathbf{A} d\mathbf{S} = \frac{2m\pi\hbar}{2e} = m\Phi_0, \quad (21)$$

where  $\Phi_0 = \frac{h}{2e}$  is the superconducting flux quantum. From this result, by using and using the GL superconducting wavefunction 8, it can be proven that the phase difference across the loop is linked to the external flux as  $\phi = 2\pi\Phi/\Phi_0$  [10], [14]. In this way, the current, and thus the energy, of the SQUID can be easily controlled by an external flux bias.

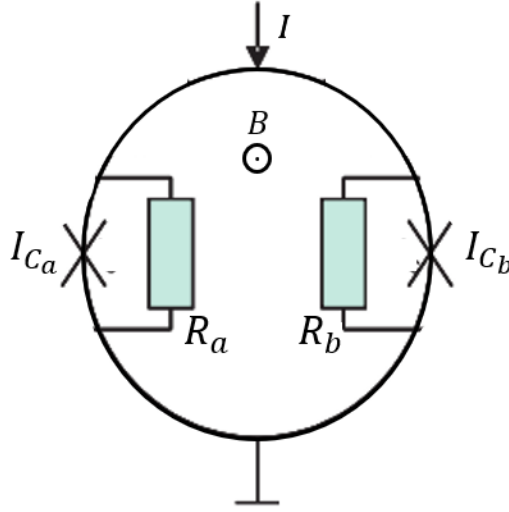


**Figure 8:** DC SQUID schematic representation [21]: the incoming current  $I$  splits in the two branches of the superconducting ring. There, it crosses two JJs, whose currents are  $I_{C_a}$  and  $I_{C_b}$ , with corresponding resistances  $R_a$  and  $R_b$ . The loop is exposed to a perpendicular magnetic flux  $\Phi_B$ .

As we did for the JJ, the equivalent circuit for the DC-SQUID in figure 8 is described by the circuit equation [21], [17]:

$$I = I_{C_a} \sin \phi_a + I_{C_b} \sin \phi_b + \frac{V}{R_a} + \frac{V}{R_b}. \quad (22)$$

By applying flux quantization and assuming that the two junctions are identical, we find that:

$$I = 2I_C \sin \phi \cos \frac{\pi\Phi}{\Phi_0} + \left( \frac{1}{R_a} + \frac{1}{R_b} \right) V, \quad (23)$$

where  $\phi = \phi_a - \phi_b$  is the phase difference,  $\Phi$  is the external magnetic field flux and  $\Phi_0$  its flux quantum. By means of the relation  $E \propto -dI/d\Phi$ , it is possible to recover the dependence on the external flux of the SQUID energy as [11]:

$$E_{J,SQUID} = E_J \left| \cos \frac{\pi\Phi}{\Phi_0} \right|. \quad (24)$$

This result is fundamental for the design of tunable superconducting qubits 2.6, as shown in section 2.7.

## 2.5 Circuit Quantum Electrodynamics

In this section, we will show that a circuit with a JJ can be studied with a QM model [7], [11]. In general, Josephson devices can be treated as binary system under particular circumstances, and therefore they can be used for qubits hardware. Let us start from the time-dependent Schrödinger equation [7]:

$$\hat{H} |\psi\rangle = i\hbar \frac{\partial}{\partial t} |\psi\rangle,$$

where  $|\psi\rangle$  is the state of the quantum system at time  $t$  and  $\hat{H}$  is the Hamiltonian that describes the total energy. To understand the dynamics of a superconducting qubit circuit, we can start with a linear LC resonant circuit (figure 9 (a)). The kinetic energy can be associated with the electrical energy of the circuit, while the potential energy with the magnetic energy. The elements of the circuit can be represented in terms of generalized circuit coordinates, charge and flux [7]. For the flux, we define the time integral of the voltage [7]:

$$\Phi_n(t) = \int_{-\infty}^t V_n(t') dt', \quad (25)$$

where  $V_n(t)$  are the voltages at the circuit nodes. For the charge, we have:

$$Q_n(t) = \int_{-\infty}^t I_n(t') dt', \quad (26)$$

where  $I_n(t)$  are the currents in the circuit branches. By using the classical relations  $V = L \frac{dI}{dt}$  and  $I = C \frac{dV}{dt}$ , the energy terms for the inductor and the capacitor in an LC circuit, as a function of the node flux, become:

$$T_C = \frac{C}{2} \dot{\Phi}^2, \quad (27)$$

and

$$U_L = \frac{C}{2} \Phi^2. \quad (28)$$

Thus, the Hamiltonian reads as:

$$H = \frac{Q^2}{2C} + \frac{\Phi^2}{2C} = \frac{CV^2}{2} + \frac{LI^2}{2}. \quad (29)$$

This Hamiltonian is analogous to the one of a mechanical harmonic oscillator with mass  $m = C$  and resonance frequency  $\omega = \frac{1}{\sqrt{LC}}$ , where the role of the position  $\hat{x}$  and momentum  $\hat{p}$  is played by  $\Phi$  and  $Q$ , respectively [7]. In order to describe a

quantum circuit, the flux and the charge must be promoted to quantum operators which satisfy the commutation relation [7]:

$$[\hat{\Phi}, \hat{Q}] = i\hbar, \quad (30)$$

and so the indetermination relation:

$$\Delta Q \Delta \Phi \geq 1. \quad (31)$$

Thus, if the charge is well-defined, the flux will not and vice versa.

From flux quantization (section 2.4), we observe that the flux and the phase operators are linked through the relation  $\hat{\phi} = \frac{2\pi\hat{\Phi}}{\Phi_0}$ . Defining the phase, or reduced flux, operator  $\hat{\phi}$  and the reduced charge operator  $\hat{n} = \frac{Q}{2e}$ , the Quantum Mechanical Hamiltonian for the circuit can be written as [7]:

$$H = 4E_C n^2 + \frac{\phi^2 E_L}{2}, \quad (32)$$

recovering the Hamiltonian of a particle in a one-dimensional quadratic potential, a quantum harmonic oscillator (QHO), as shown in figure 9 (b). Treating  $\phi$  as the generalized position coordinate, the solution to the eigenvalues problem gives an infinite series of eigenstates corresponding to eigenenergies equally spaced [7]. The plasma frequency of this harmonic oscillator is

$$\omega_r = \frac{1}{\sqrt{LC}} = \sqrt{\frac{8E_L E_C}{\hbar^2}}. \quad (33)$$

In second quantization, the QHO hamiltonian becomes [7]:

$$H = \hbar\omega_r \left( \hat{a}^\dagger \hat{a} + \frac{1}{2} \right). \quad (34)$$

The degeneration of the QHO energies does not allow building a quantum computational base set. However, by replacing the linear inductor with a non-linear element, like a JJ (figure 9 (c)), the functional form of the potential energy follows the nonlinear behaviour of the Josephson energy in equation 2.3, and H becomes:

$$H = 4E_C n^2 - E_J \cos \phi, \quad (35)$$

where the charge energy is:

$$E_C = \frac{e^2}{2C_\sigma}, \quad (36)$$

and  $C_\sigma = C_J + C_S$  is the total circuit capacitance, which includes shunt capacitance and Josephson capacitance. The JJ introduces the anharmonic element that

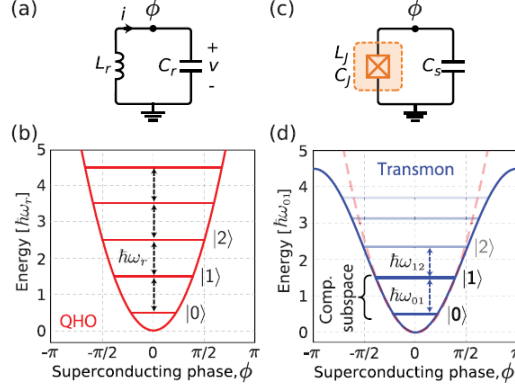


**Figure 9:** Comparison between an LC circuit (quantum harmonic oscillator, QHO), on the left, and a nonlinear anharmonic oscillator with a JJ (transmon), on the right [7]. In a) equivalent circuit of an LC oscillator with  $L_r$  and  $C_r$ ; b) energy potential for QHO, where energy levels are equidistantly spaced  $\hbar\omega_r$ ; c) Josephson qubit circuit, the non-linear inductance  $L_J$  represented by the JJ is shunted with a capacitance  $C_s$ ; d) energy potential of a transmon qubit in blue, compared to the quadratic one of a QHO (dashed red). We can isolate the ground state  $|0\rangle$  and the excited state  $|1\rangle$ , whose energy separation  $\hbar\omega_{01}$  is different from  $\hbar\omega_{12}$  [7].

ensures an inhomogeneous separation of the energy levels, thus the possibility to implement an artificial quasi-two-level system (Fig 9 (d)) [7].

Superconducting qubits are characterized in terms of the ratio  $\frac{E_J}{E_C}$  and the computational basis used for the two-level system implementation [13]. According to the indetermination principle in equation 31, for high values of the ratio  $\frac{E_J}{E_C}$  the phase is well-defined, while for low values of the  $\frac{E_J}{E_C}$  ratio the dynamics is determined by the number of Cooper pairs. Therefore, it is possible to define three main superconducting qubits archetypes: the phase, the flux and the charge qubits [11]. Minor or major modifications to one of these main circuits allows for the implementation of several other superconducting qubits. The main reason behind the searching of innovative designs is the need to fight decoherence, as we will see for the transmon qubit [11] (section 2.6, 3.1). We now summarize the main characteristics of the three superconducting qubit archetypes [13].

- **Phase qubit:** In a phase qubit, the two-level system is formed by the potential wells of a current-biased JJ [13] (10 (c)). This is based on the phase dynamics of the JJ (section 2.3). Specifically, the two-level system is obtained by taking the first two energy levels of a well of the washboard potential, discussed in equation 6 [13]. In this qubit, the ratio  $\frac{E_J}{E_C}$  is much larger than one, and this property protects this qubit from charge noise [11]. The main

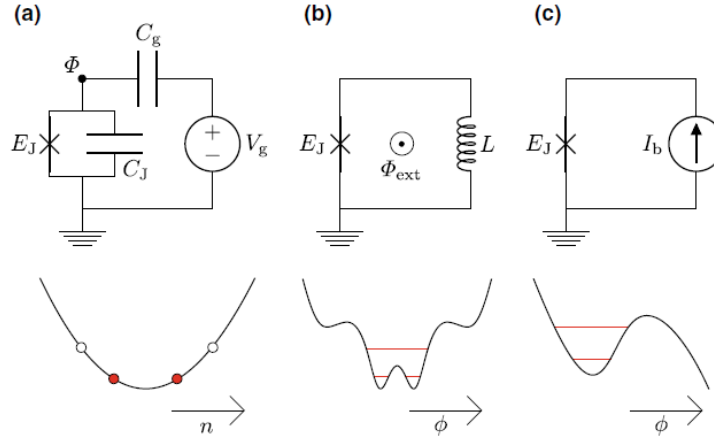


**Figure 10:** Circuitual representation and potential energy of a Cooper-Pair-Box (a), a flux-qubit and c) a phase qubit [13].

problem of the phase qubit is the fact that coherence times are too short [13]. In fact, they are very sensible to phase noise, induced by critical current fluctuations. This unavoidably introduces decoherence, as will be discussed in section 3.4.

- **Flux qubit:** In its simplest form, it consists of a SQUID controlled by an external flux [13]. The flux qubit Hamiltonian can be seen as the one describing a particle with an isotropic mass moving in a periodic two-dimensional potential [13]. It was observed that if  $\Phi_{\text{ext}}/\Phi_0 = 0.5$  the potential is symmetric and the states have a well-defined parity [13] (10 (b)). In addition, in order to create a two-level system, the circuit must have a large self-inductance, so the superconducting loop needs to be large [13]. This introduces a high sensitivity to flux noise [11]. On the other hand, if the external flux is near this sweet spot, the two lowest levels are well separated from the others, making the circuit a good qubit [13].
- **Charge qubit:** It is also known as Cooper pair box (CPB) [11], [13]. It consists of a superconducting island connected to a superconducting reservoir through a JJ [13]. It can be controlled by a voltage  $V_G$  through a gate capacitance, which determines a background charge  $n_g$ . The resulting Hamiltonian expressed in the basis of the number of Cooper pairs operator  $\hat{n}$  can be studied as a tight-binding Hamiltonian with  $E_C$  and  $n_g$  determining the on-site energy and  $E_J$  setting the tunnelling matrix element between neighbouring

states [11]. As we have seen for the flux qubit, there is a sweet spot for offset charge [13]. In fact, if  $n_g = m + \frac{1}{2}$ , we observe that the eigenstates have defined parity, and the first two of them are well separated from others (10 (a)). In addition, the energies of the states  $|m\rangle$  and  $|m+1\rangle$  are degenerate, and the transition frequency depends on  $E_J$  only [13]. Most importantly, at these points the qubit is less sensitive to charge noise, meaning that  $\partial H_{\text{CPB}}/\partial n_g = 0$ . If we are far from the sweet spots, this type of qubit is affected by charge noise [11].

## 2.6 A charge-noise protected qubit: the transmon

As discussed in the previous section, depending on the circuitual design of superconducting qubits, they may be very sensitive to environmental noise, and this can affect their performance. The transmon qubit was specifically designed to have a reduced sensibility to charge noise. Its name is an abbreviation of the term *transmission line shunted plasma oscillation qubit*. It is a CPB with a large shunt capacitance whose purpose is to lower charge energy and thus increase the ratio  $\frac{E_J}{E_C}$  [11], [13], as we can see from the equivalent circuit in figure 11. For readout, the transmon uses a superconducting resonator, which is represented in the microwave regime by a harmonic LC oscillator, as will be discussed in section 2.8.

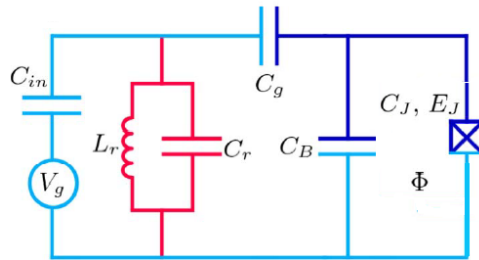


**Figure 11:** Transmon equivalent circuit: the JJ, identified by  $C_J$  and  $E_J$ , is shunted by the capacitance  $C_B$ , and capacitively coupled through  $C_g$  to the readout resonator, represented as an LC circuit ( $L_r$  and  $C_r$ ). The external electronics represented by  $V_g$  is capacitively coupled through  $C_{in}$  to the circuit. [7].

In order to study the transmon qubit Hamiltonian, we start with the one of the CPB with an additional parallel capacitance [7]. It can be proven that the effective Hamiltonian for a transmon qubit circuit in terms of the generalized coordinates number of Cooper pair  $\hat{n}$  and phase difference across the junction  $\hat{\phi}$  is:

$$\hat{H} = 4E_C (\hat{n} - n_g)^2 - E_J \cos \hat{\phi}. \quad (37)$$

Thanks to the shunt capacitance  $C_b$  the charge energy is:

$$E_C = \frac{e^2}{2C_\Sigma} \quad (C_\Sigma = C_g + C_b + C_{in}), \quad (38)$$

far smaller than  $E_J$ . This makes the phase a good quantum number, so the Hamiltonian can be solved in the  $\hat{\phi}$  basis in terms of the Mathieu function, thus giving the eigenvalues [11]:

$$E_m(n_g) = E_C a_{2[n_g+k(m,n_g)]}(-E_J/2E_C), \quad (39)$$

where  $a_\nu(q)$  is Mathieu's characteristic value and  $k(m, n_g)$  is an appropriate sorting function:

$$k(m, n_g) = \sum_{l=\pm 1} [\text{int}(2n_g + l/2) \bmod 2] \times \text{int}(n_g) + l(-1)^m [(m+1) \text{div} 2]. \quad (40)$$

From this we can evaluate the charge dispersion of the transmon  $\epsilon_m$ , which is

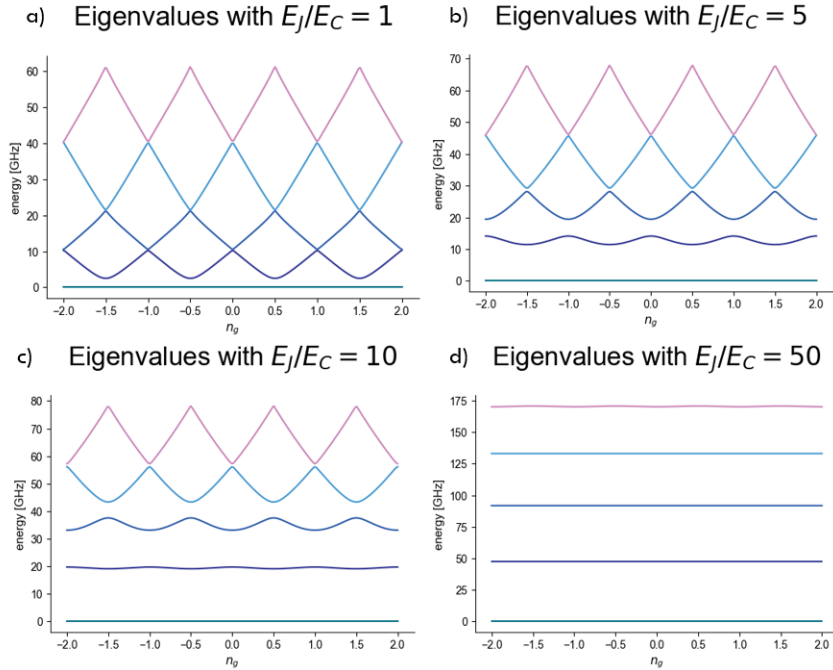


**Figure 12:** Energy spectrum as a function of the Cooper-pair offset charge  $n_g$  in a Cooper-pair box with: a)  $\frac{E_J}{E_C} = 1$ , b)  $\frac{E_J}{E_C} = 5$ , c)  $\frac{E_J}{E_C} = 10$ , d)  $\frac{E_J}{E_C} = 50$ . Plots produced with the Python library *scqubits* [12].

defined as the difference between the energy levels at  $n_g = 0$  and  $n_g = 0.5$ , i.e. in the sweet-spot and far from the sweet-spot of the circuit. If we study the asymptotics limits of the Mathieu's characteristic values, the charge dispersion is given by:

$$\begin{aligned}\epsilon_m &= E_m(n_g = 1/2) - E_m(n_g = 0) = \\ &= (-1)^m E_C \frac{2^{4m+5}}{m!} \sqrt{\frac{2}{\pi}} \left(\frac{E_J}{2E_C}\right)^{\frac{m}{2} + \frac{3}{4}} e^{-\sqrt{8E_J/E_C}}.\end{aligned}\quad (41)$$

The very crucial result is that the dispersion, which represents charge noise, decreases exponentially with the ratio  $\frac{E_J}{E_C}$ , as we can see from figure 12.

The major drawback of the increasing of the ratio  $E_J/E_C$  is the reduced anharmonicity of the circuit. We define the absolute and relative anharmonicity [11] as the energy difference between the computational base-set energy  $E_{10}$  and the first excited energies  $E_{12}$  as:

$$\alpha \equiv E_{12} - E_{01}, \quad \alpha_r \equiv \alpha/E_{01}.\quad (42)$$

It can be proven that, for  $E_J \gg E_C$ , the anharmonicities are approximately [7], [11]:

$$\alpha \simeq -E_C, \quad \alpha_r \simeq -(8E_J/E_C)^{-1/2}.\quad (43)$$

The relative anharmonicity  $\alpha_r$  only decreases as a power law when increasing  $E_J/E_C$ , compared to the exponential reduction of the charge dispersion. This makes the transmon circuit a good compromise to suppress charge noise while keeping the anharmonicity sufficiently high.

## 2.7 Tunability and Control

As pointed out by the DiVincenzo criteria, it must be possible to control (or drive) the state of the qubit. This means that we have to couple the qubit to opportunely chosen circuits in order to drive the qubit. Generally speaking, this occurs when the qubit interacts with control circuits, and the total Hamiltonian reads as [7]:

$$H = H_1 + H_2 + H_{\text{int}},\quad (44)$$

where  $H_1$  is the uncoupled qubit Hamiltonian,  $H_2$  is the Hamiltonian of the non-interactive circuit and  $H_{\text{int}}$  is the mutual interaction between the qubit and the control circuits, respectively.

In order to control the qubit and implement quantum logic, we need an external parameter that can tune the qubit frequency, defined as  $\omega_q = \sqrt{\frac{8E_J E_C}{\hbar^2}}$ . A widely

used technique is to replace the single JJ in the circuit in figure 11 with a DC-SQUID [7], also known as split-transmon. As we saw in section 2.3, the current in the ring depends on the external magnetic flux. By using the expression of  $E_J$  shown in equation 24, the effective Hamiltonian becomes [7]:

$$H = 4E_C n^2 - E_J \left| \cos\left(\frac{\pi\Phi_e}{\Phi_0}\right) \right| \cos(\phi). \quad (45)$$

This means that  $E_J(\Phi_e) = E_J \left| \cos\left(\frac{\pi\Phi_e}{\Phi_0}\right) \right|$  is tunable by the external magnetic flux  $\Phi_e$ . In order to achieve this goal, an inductive coupling is implemented, where mutual inductance  $M_{12}$  is shared by the qubit and the flux-bias circuitry, sustaining currents  $I_1$  and  $I_2$ , respectively. The interaction Hamiltonian reads as:

$$H_{\text{int}} = M_{12} I_1 I_2. \quad (46)$$

Here, flux lines are designed as coplanar waveguides (CPW) in proximity to the DC-SQUID in the transmon circuit. If a current is carried along the flux line, and an inductive coupling holds, the magnetic field that generates because of the Biot-Savart law concatenates to the SQUID loop. Therefore, a magnetic field flux perpendicular to the SQUID loop is generated.

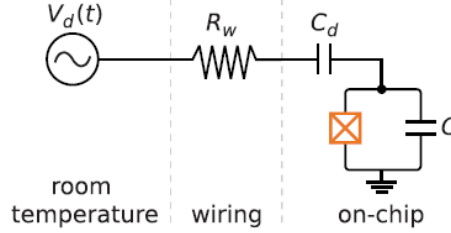


**Figure 13:** Circuit diagram of qubit capacitively coupled to a microwave drive circuit [7]: the qubit circuit is coupled to the drive signal  $V_d(t)$  through a shunt capacitance  $C_d$ , the wiring is represented by a resistance  $R_w$

Capacitive couplings, instead, are massively employed in transmon circuits for both readout and control mechanisms. In this case, a capacitor  $C_g$  is placed between the voltage nodes  $V_1$  and  $V_2$  of the qubit and the readout or the drive circuits, respectively, and we have:

$$H_{\text{int}} = C_g V_1 V_2. \quad (47)$$

An example of a capacitively coupled drive circuit is shown in figure 13. To control the qubit state, we must be able to excite it with a drive pulse. The

Hamiltonian of a qubit capacitively coupled with a drive signal is [7]:

$$H = H_0 + H_d = -\hbar\frac{\omega_q}{2}\sigma_z + \frac{C_d}{C_\Sigma^D}\sqrt{\frac{\hbar}{2Z}}V_D(t)\sigma_y, \quad (48)$$

where the first term is the qubit Hamiltonian with  $\omega_q = (E_1 - E_0)/\hbar$ , and the second is the drive signal with  $C_d$  the capacitance that couples the qubit with the RF electronics. Here,  $Z$  is the impedance of the circuit to the ground and  $C_\Sigma^D$  is the sum of  $C_d$  and the total capacitance of the transmon  $C_\Sigma$ .

In order to visualize the role of the drive, we move into a frame rotating with the qubit frequency  $\omega_q$  [7]. We consider a state  $|\psi_0\rangle$  evolving as:

$$|\psi_0(t)\rangle = U_{H_0}|\psi_0\rangle = \frac{1}{\sqrt{2}}\begin{pmatrix} e^{i\omega_q t/2} \\ e^{-i\omega_q t/2} \end{pmatrix}, \quad (49)$$

where  $U_{H_0}$  is the propagator corresponding to  $H_0$ . We define  $U_{rf} = U_{H_0}^\dagger = e^{iH_0 t}$  and the state  $|\psi_{rf}(t)\rangle = U_{rf}|\psi_0\rangle$ . By applying the Schrödinger equation with the total Hamiltonian to the new state in the rotating frame, we obtain the new  $H$  as  $\tilde{H}$ . We focus on the term which describes the signal  $\tilde{H}_d$  [7]:

$$\tilde{H}_d = \frac{C_d}{C_\Sigma^D}\sqrt{\frac{\hbar}{2Z}}V_D(t)(\cos(\omega_q t)\sigma_y - \sin(\omega_q t)\sigma_x). \quad (50)$$

We can assume that the time-dependent part of the voltage has the form [7]:

$$v(t) = s(t)\sin(\omega_d t + \phi) = s(t)(\cos(\phi)\sin(\omega_d t) + \sin(\phi)\cos(\omega_d t)). \quad (51)$$

Here,  $s(t)$  is a dimensionless envelope function. We define the *in phase* component  $I = \cos\phi$  and the *out of phase* component  $Q = \sin\phi$  and obtain the following expression for the voltage:

$$V_D(t) = V_0 s(t)(\sin(\omega_d t)I - \cos(\omega_d t)Q). \quad (52)$$

If we put these expressions in the Hamiltonian, and we use the Rotating Wave Approximation (RWA), i.e. we drop out the fast rotating terms with  $\omega_d + \omega_q$  that averages to zero, we obtain [7]:

$$\tilde{H}_d = \frac{C_d}{C_\Sigma^D}\sqrt{\frac{\hbar}{2Z}}\frac{V_0 s(t)}{2}(\sigma_x(Q\sin\delta\omega t - I\cos\delta\omega t) + \sigma_y(I\sin\delta\omega t - Q\cos\delta\omega t)), \quad (53)$$

where  $\delta\omega = \omega_q - \omega_d$ . If  $\omega_d = \omega_q$ , i.e. the drive signal is on resonance with the qubit frequency, the drive Hamiltonian reads as:

$$\tilde{H}_d = -\frac{C_d}{C_\Sigma^D} \sqrt{\frac{\hbar}{2Z}} \frac{V_0 s(t)}{2} (I\sigma_x + Q\sigma_y). \quad (54)$$

For example, from figure 14 we can see the effect of a  $X_{\frac{\pi}{2}}$ , i.e. a rotation of  $\pi/2$  around the x-axis, applied on the ground state on the Bloch sphere.

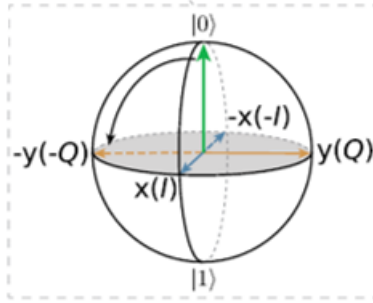


**Figure 14:** The action of a rotation of  $\pi/2$  around the x-axis, showing I (in blue) and Q (in yellow) components on the Bloch sphere [7].

## 2.8 Readout

In a superconducting qubit, it is mandatory to find a way to read the state of the qubit while preserving its quantum state. As a matter of fact, in QM the problem of the measurement of the quantum state is one of the most intriguing and challenging issues, directly related to the collapse of a quantum state when it is observed. However, in transmon qubits it has been proposed to use superconducting resonators to establish a quantum non demolitive (QND) readout of the qubit state.

A superconducting resonator is typically designed as a Coplanar Waveguide (CPW) capacitively coupled to the qubit. For RF frequencies and dimensions of the CPW much smaller than the RF wavelength, the CPW is nothing else than an LC circuit. The Hamiltonian of a superconducting resonator coupled to a qubit is described in equation 55. This Hamiltonian is also known as Jaynes-Cummings Hamiltonian and describes the interaction between a bosonic field and a two-level system [7]:

$$H = \omega_r \left( a^\dagger a + \frac{1}{2} \right) + \frac{\omega_q}{2} \sigma_z + g \left( \sigma_+ a + \sigma_- a^\dagger \right), \quad (55)$$

where  $\omega_r$  and  $\omega_q$  are the frequencies of the resonator and the qubit, while  $\sigma_+$  and  $\sigma_-$  are the exciting and de-exciting operators of the qubit, and finally  $a^\dagger$  and  $a$  are the creation and destruction operators of the photons in the resonator. In order to perform a quantum non-demolition readout, the system must be in the dispersive regime. In this limit, the detuning  $\Delta$  between  $\omega_r$  and  $\omega_q$  is large compared to the coupling  $g$  between the resonator and the qubit, i.e.  $\Delta = |\omega_q - \omega_r| \gg g$ . The Hamiltonian can be approximated using a second order perturbation theory, in terms of the rate  $\frac{g}{\Delta}$ , as:

$$H_{\text{disp}} = (\omega_r + \chi\sigma_z)(a^\dagger a + \frac{1}{2}) + \frac{\omega_q}{2}\sigma_z, \quad (56)$$

where  $\chi$  is known as dispersive shift [7]:

$$\chi = \frac{g_{01}^2}{\Delta}. \quad (57)$$

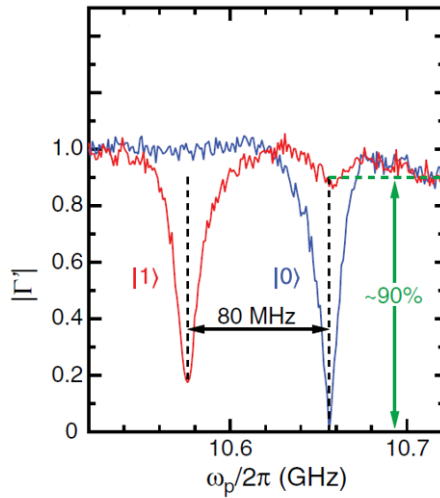


**Figure 15:** Quantum non demolitive readout [22]: the readout resonator shifts its frequency  $\tilde{\omega}_r$  as it couples with the qubit; when the qubit is in  $|0\rangle$ , we have the blue curve; when the qubit is in  $|1\rangle$ , then we observe the red curve.

In this way, the resonance frequency of the resonator is renormalized as a function of the dispersive shift  $\chi$  and the qubit state  $\sigma_z$  as:  $\tilde{\omega}_r = \omega_r + \chi\sigma_z$ , as shown in figure 15. In this way, we can read the qubit state by probing the resonator and measuring its shift but, since the detuning is large, we do not directly exchange energy with the qubit, thus providing a QND readout of the qubit state. Note that

the dispersive shift  $\chi$  depends on the detuning  $\Delta$ . Therefore, depending on the detuning sign, the shift related to each different initial state for the qubit can occur towards larger or smaller readout resonator frequencies, compared to the frequency that the resonator would have if not coupled to a two-level system.

## 2.9 Coupled qubits

As pointed out by the DiVincenzo criteria, in order to build a quantum computer, it must be possible to implement at least two qubits gates. In this section, we will describe qubit-qubit coupling, and then we will discuss the phenomenon of the avoided level crossing, which is the direct consequence of the energy exchange between coupled qubits [7], [23].

Coupling between superconducting transmon qubits can be achieved in several

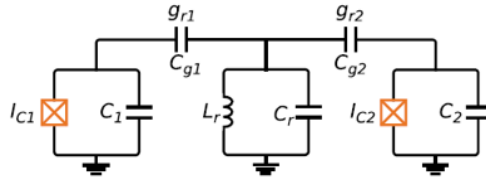


**Figure 16:** Two qubits coupled by means of coupling capacitances  $C_{g1}$  and  $C_{g2}$  to a superconducting resonator ( $L_r, C_r$ ) [7].

ways [7], [13]. However, in this work we will focus on a specific coupling design, in which qubits coupling is mediated by a superconducting resonator, also known as coupler [7]. An example is shown in figure 16, where two transmon qubits are both capacitively coupled to the central resonator. The two-level system Hamiltonian is [7]:

$$H = \sum_{i \in \{1,2\}} [\omega_i \hat{a}_i^\dagger \hat{a}_i + \frac{\alpha}{2} \hat{a}_i^\dagger \hat{a}_i^\dagger \hat{a}_i \hat{a}_i] + g_{1r} (a_1^\dagger a_r + a_1 a_r^\dagger) + g_{2r} (a_2^\dagger a_r + a_2 a_r^\dagger), \quad (58)$$

where  $g_{1r}$  and  $g_{2r}$  are the coupling energies mediated by the coupling resonator. It can be shown that in the dispersive limit, i.e. if  $g_{i_r} \ll |\omega_i - \omega_r|$ , the resonator can be treated as an isolated system, and the composite system can be simplified to two transversely coupled qubits. In this limit, if we ignore higher energy levels, we can write the Hamiltonian as [23]:

$$H_J = \hbar \sum_{i=1,2} \frac{\omega_{ge}^{(i)}}{2} \sigma_z^{(i)} + \hbar \sum_j \left( \omega_j + \chi_j^{(1)} + \chi_j^{(2)} \right) a_j^\dagger a_j + \hbar J \left( \sigma_+^{(1)} \sigma_-^{(2)} - \sigma_+^{(2)} \sigma_-^{(1)} \right), \quad (59)$$

which is obtained by using the renormalized frequencies in equation 56. The first term describes the energy of the single-qubits, the second term represents the resonators modes characterized by the dispersive shift due to the coupling with the qubits. Finally, the third term is the effective qubit-qubit coupling, which is characterized by the transverse exchange coupling  $J$  [23]:

$$J = \frac{1}{2} \sum_j g_j^{(i)} g_j^{(i)} \left( \frac{1}{\Delta_j^{(i)}} + \frac{1}{\Delta_J^{(i)}} \right). \quad (60)$$

This Hamiltonian leads to an avoided level crossing of the excited qubit state, i.e. the energy levels of two interacting qubits do not cross, and avoid each others when they approach the same value, i.e. when they go on resonance. If the two qubits are at the same frequency, the size of the splitting is [23]:

$$2J = \hbar \sum_j 2g_j^{(1)} g_j^{(2)} / \Delta_j. \quad (61)$$

Under these circumstances, the eigenstates of two coupled qubits, will be the symmetric triplet states  $|gg\rangle$ ,  $|ee\rangle$  and  $|\psi_s\rangle = (|ge\rangle + |eg\rangle) / \sqrt{2}$ , as well as the anti-symmetric singlet state  $|\psi_a\rangle = (|ge\rangle - |eg\rangle) / \sqrt{2}$ . In the cases of  $|\psi_s\rangle$  and  $|\psi_a\rangle$ , we note that the states are entangled, and a single excitation is shared between the two qubits, as in figure 17 (a). We can put the qubits into resonance by performing

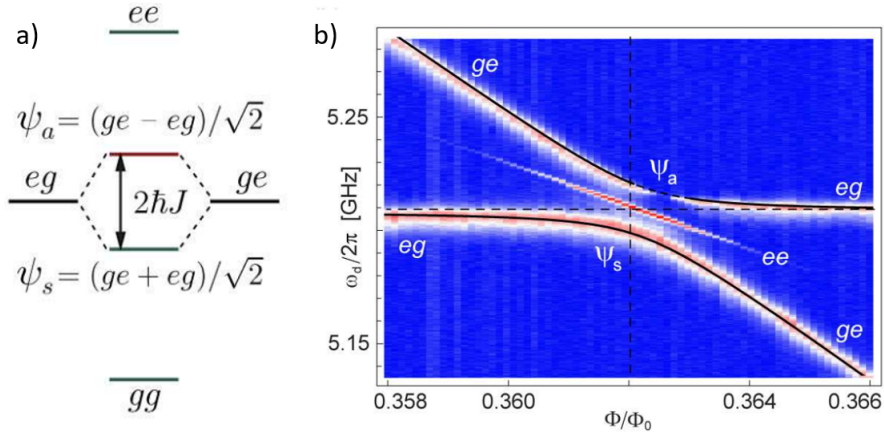


**Figure 17:** a) Energy level diagram of two transversely coupled transmon qubits, the energy separation between symmetric  $|\psi_s\rangle$  and antisymmetric  $|\psi_a\rangle$  states is proportional to the qubit coupling strength  $J$ . b) Flux spectroscopy measurement of the avoided level crossing as a function of the qubit drive frequency and the external flux in units of the flux quantum [23].

a flux spectroscopy, which will be discussed in chapter 3. The upper and lower

branches shown in figure 17 (b) can be fitted with the function [23]:

$$f(\omega; \omega_{ge}^{(1)}, J) = \left( \omega + \omega_{ge} \pm \sqrt{(\omega_{ge}^{(1)} - \omega)^2 + 4J^2/2} \right). \quad (62)$$

From this equation, we can evaluate the coupling strength  $J$ , which is typically of the order of tens of megahertz [23].

### 3 Noise and decoherence in superconducting qubits

Since superconducting qubits are quantum macroscopic objects easily interfaced with control and readout electronics, they are very sensitive to environmental noise, and having good coherence properties is a hard task. This thesis focuses on the understanding of which are the most important decoherence sources in a superconducting qubit, by means of a comparative and self-consistent analysis of experimental and theoretical relaxation and coherence times. Indeed, the high sensitivity to noise of a qubit can be exploited to understand the response of a generic system to unknown noise sources. In fact, qubits are often used as noise sensors to probe innovative devices [24]. In this chapter, we will show that superconducting qubits decoherence is strictly related to the qubit circuitual design, the readout and the control circuits. Even though the peculiar circuitual design of transmon qubits has contributed to the improvement of coherence times towards values of the order of tens to hundreds of microseconds [11], the understanding of the physical processes limiting coherence is of fundamental importance.

In order to visualize the decoherence times linked to the main noise sources as a function of circuitual parameters defined by design, and the effect of tunable and externally controllable parameters, we will use the Python library *scqubits* [12]. This package provides a user-friendly, object-oriented Python library of the most common superconducting qubits. It facilitates automatic construction of circuit Hamiltonians in an appropriate basis, provides high-level routines for finding eigenenergies, eigenstates, and matrix elements, and allows the user to quickly visualize these quantities as a function of external parameters. It also gives theoretical predictions of the coherence times, by using the model for noise described in this chapter [11], [7], [25], [26], [27].

#### 3.1 Bloch-Redfield model for noise

In an open system, the qubit interacts with unknown degrees of freedom in the environment, which we refer to as fluctuations or noise [7]. We can categorize the type of noise in two main types: systematic noise and stochastic noise [7]. Systematic noise arises from a control or readout error, while stochastic noise is related to random fluctuations of the parameters that are coupled to the qubit. The degree to which a qubit is affected by noise is related to the amount of fluctuations affecting it, and its susceptibility to them [7].

As introduced in section 2.1, an arbitrary state can be represented as a point of the Bloch sphere [7]:

$$|\psi\rangle = \alpha |0\rangle + \beta |1\rangle = \cos \frac{\theta}{2} |1\rangle + \sin \frac{\theta}{2} e^{i\phi} |1\rangle. \quad (63)$$

We note that the density matrix  $\rho = |\psi\rangle\langle\psi|$  for a pure state  $\psi$  is:

$$\rho \equiv \frac{1}{2} \begin{pmatrix} 1 + \cos \theta & e^{-i\phi} \sin \theta \\ e^{i\phi} \sin \theta & 1 - \cos \theta \end{pmatrix} = \begin{pmatrix} |\alpha|^2 & \alpha\beta^* \\ \alpha^*\beta & |\beta|^2 \end{pmatrix}. \quad (64)$$

However, fluctuations and noise introduce a spurious decay of the qubit state, characterised by two main decay rates: longitudinal relaxation rate,

$$\Gamma_1 \equiv 1/T_1, \quad (65)$$

and transverse relaxation rate,

$$\Gamma_2 \equiv 1/T_2 = \Gamma_1/2 + \Gamma_\phi. \quad (66)$$

- **Longitudinal relaxation:**  $\Gamma_1$  describes a depolarization along the qubit quantization axis, also known as energy relaxation. Longitudinal relaxation is caused by transversal noise, i.e. a noise source that couples to the qubit via x or y-axis, which are perpendicular to the quantization axis z (figure 18 (a)) [7]. This comes from the intuition that only off-diagonal matrix elements of the interaction Hamiltonian can induce transitions between states  $|0\rangle$  and  $|1\rangle$ . This typically causes both up transition and down transition, i.e. the qubit can go from a less energetic state to a more energetic one and vice versa. Only noise at the qubit frequency mediates qubit transitions, absorption or emission, i.e. it is a resonant phenomenon [7]. In transmon qubits, typical relaxation times are of the order of tens to hundreds of microseconds [7].
- **Pure dephasing:** it is described by the decay parameter  $\Gamma_\phi$ , which concerns depolarization in the x-y plane of the Bloch sphere, and it is caused by longitudinal noise, meaning that it couples with the qubit via the z-axis (figure 18 (b)) [7]. In terms of the interaction Hamiltonian, we are considering only the on-diagonal elements. This type of noise makes the Bloch vector precess in the rotating frame. We have a total depolarization of the azimuthal angle. This stochastic effect is captured in the transverse relaxation rate  $\Gamma_2$  [7]. Pure dephasing is not a resonant phenomenon, in fact, noise at any frequency can modify the qubit frequency. It is also elastic because there is no energy exchange with the environment, so it is reversible [7].
- **Transverse relaxation:** it is described by the decay parameter  $\Gamma_2 = \Gamma_1/2 + \Gamma_\phi$  [7], which corresponds to the loss of coherence of a superposition state, pointed along the x-axis on the equator of the Bloch sphere (figure 18 (c)). Decoherence is caused by both longitudinal and transverse noise [7].

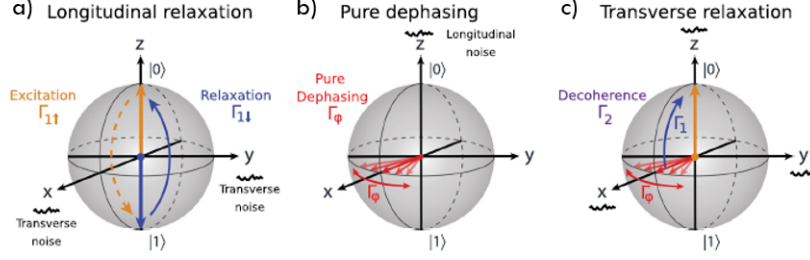


**Figure 18:** Transverse and longitudinal noise on the Bloch sphere: a) longitudinal relaxation due to transverse noise, b) pure dephasing due to longitudinal noise, c) transverse relaxation representation on the Bloch sphere [7]

Therefore, the density matrix for a qubit affected by noise becomes [7]:

$$\rho_{\text{BR}} \equiv \begin{pmatrix} 1 + (|\alpha|^2 - 1)e^{-\Gamma_1 t} & \alpha\beta^* e^{i\delta\omega t} e^{-\Gamma_2 t} \\ \alpha^*\beta e^{-i\delta\omega t} e^{-\Gamma_2 t} & |\beta|^2 e^{-\Gamma_1 t} \end{pmatrix}, \quad (67)$$

also known as Bloch-Redfield representation. We have introduced the longitudinal decay function  $e^{-\Gamma_1 t}$ , which is connected to longitudinal relaxation or excitation between the excited state  $|1\rangle$  to the ground state  $|0\rangle$ . This decay function only contributes to the on-diagonal terms of the density matrix because it determines the probability to find the qubit in the state  $|0\rangle$  or  $|1\rangle$ .

We also define the transverse relaxation function  $e^{-\Gamma_2 t}$ , which represents the transverse relaxation. Since transverse decay includes dephasing, we expect to find it only in the off-diagonal elements, which contains information about the phase  $\phi$ , as pointed out in equation 64. Moreover, it is fundamental to introduce the detuning parameter  $\delta\omega = \omega_q - \omega_d$ , which takes in account if the qubit frequency  $\omega_q$  differs from the one inducing the transition  $\omega_d$ .

### 3.2 Noise power spectral density

In order to understand the behaviour of a noise source, we must know its power spectral density. By analyzing the frequency dependency of the noise source and its coupling with the qubit, we can say if it induces relaxation or dephasing and evaluate the resulting rates  $\Gamma_1$ ,  $\Gamma_2$  and  $\Gamma_\phi$ .

The frequency distribution of the noise power for a stationary noise source  $\lambda$  is characterized by  $S_\lambda(\omega)$ , which is the Fourier transform of the noise correlation

function  $c_\lambda(\tau) = \langle \lambda(\tau)\lambda(0) \rangle$  [7]:

$$S_\lambda(\omega) = \int_{-\infty}^{\infty} \langle \lambda(\tau)\lambda(0) \rangle e^{-i\omega\tau} d\tau. \quad (68)$$

We can connect relaxation and dephasing to the spectral density  $S_\lambda(\omega)$ . The cou-

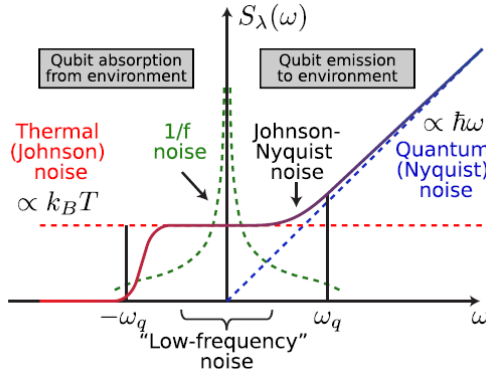


**Figure 19:** Noise power spectral density [7] as a function of the noise frequency: thermal noise proportional to temperature  $T$  in dashed red; Nyquist noise, which is proportional to  $\hbar\omega$  in blue;  $1/f$  noise in green.

pling between the qubit degrees of freedom  $\hat{O}_q$  and the ones of an external source of noise  $\lambda$  can be visualized as an interacting Hamiltonian [7]:

$$\hat{H}_{\text{int}} = \nu \hat{O}_q \hat{\lambda}. \quad (69)$$

Here,  $\nu$  is the coupling strength, linked to the sensitivity of the qubit to environmental noise ( $\partial \hat{H}_q / \partial \lambda$ ) [7]. By evaluating the matrix element corresponding to this derivative, we will be able to characterize the noise sources and their relaxation and dephasing rates. In particular, when the noise is resonant with the transition frequency of the qubit, it induces energy relaxation with a rate that is proportional to the spectral density at this particular frequency [7], [11].

For example, thermal noise proportional to temperature  $T$  with a white noise spectrum, when resonant with the qubit, will drive to both stimulated emission and absorption processes [7], as shown in figure 19. If the qubit spontaneously emits energy to the environment, we have quantum noise, which depends on the frequency as  $\hbar\omega$  [7].

A noise source  $\lambda$  can cause energy relaxation with a rate given by the Fermi's golden rule [7]:

$$\Gamma_1 = \frac{1}{\hbar^2} \left| \langle 0 | \hat{B}_\lambda | 1 \rangle \right|^2 S_\lambda(\omega_q), \quad (70)$$

where  $\omega_q$  is the transition frequency of the qubit,  $S_\lambda(\omega_q)$  is the noise spectral density evaluated at the qubit frequency and  $\hat{B}_\lambda$  is the operator corresponding to the noise source. From equation 70, we are able to evaluate the relaxation time associated to a particular noise source, if we know its spectrum and interaction term. Differently from relaxation, dephasing can be induced by longitudinal noise characterized by a frequency different from the transition frequency of the qubit. In order to relate the qubit decay rate due to dephasing to the noise spectrum, we can evaluate the off-diagonal term of the density matrix as (equation 68):

$$\rho_{01}(t) = e^{i\omega_{01}t} \langle e^{-i \int_0^t dt' v(t')} \rangle, \quad (71)$$

where  $v(t) = \sum_j \frac{\partial h_z(\lambda_i)}{\hbar \partial \lambda_j} \delta \lambda_j$ , with  $h_z(\lambda_i)$  the hamiltonian term of the interaction on the z-axis with the noise source  $\lambda_i$ . In terms of the noise power spectral density [11]:

$$S_v(\omega) = \int_{-\infty}^{\infty} d\tau \langle v(0)v(\tau) \rangle e^{-i\omega\tau} = \sum_j \frac{\partial h_z(\lambda_i)}{\hbar \partial \lambda_j} \delta \lambda_j S_{\lambda_j}(\omega). \quad (72)$$

Thus, the matrix element becomes:

$$\rho_{01}(t) = e^{i\omega_{01}t} \exp \left( -\frac{1}{2} \int_{-\infty}^{\infty} \frac{d\omega}{2\pi} S_v(\omega) \frac{\sin^2(\omega t/2)}{(\omega/2)^2} \right). \quad (73)$$

It can be proven [11] that for correlation times  $t_c$  small compared to the typical acquisition time  $t$ , the dephasing follows an exponential decay law and the corresponding line shape is Lorentzian:

$$\rho_{01}(t) \simeq e^{i\omega_{01}t} \exp \left[ -\frac{1}{2} |t| S_\nu(\omega = 0) \right]. \quad (74)$$

However, typical noise sources inducing dephasing have a 1/f spectrum [11], [7], which diverges at low frequencies, as shown in figure 19 in dashed green. This type of noise comes from recombination events, so it is a stochastic phenomenon [11]. For noise generated by a large number of fluctuators that are weakly coupled to the qubit, the spectral noise distribution is a Gaussian [7]. As a matter of fact, for noise spectra singular at  $\omega=0$ , like  $\frac{1}{f}$  noise, the power spectral density has the following expression [11]:

$$S_{\lambda_i} \simeq \frac{2\pi A^2}{|\omega|^\mu}, \quad (75)$$

where  $A$  is the noise amplitude, which determines the overall amplitude of the fluctuations [11]. For 1/f spectra, the transverse relaxation rate can be written as [11]:

$$\rho_{01}(t) \simeq e^{i\omega_{01}t} \exp \left[ -\frac{A^2}{\hbar^2} \left( \frac{\partial h}{\partial \lambda_i} \right)^2 t^2 |\ln(\omega_i t)| \right], \quad (76)$$

where  $\omega_i$  is the infrared cut-off frequency. Equation 76 shows that for this type of noise, the dephasing rate follows a Gaussian behaviour rather than a decaying function. Therefore, the experimental study of relaxation and coherence times provides a practical way to inspect the nature of the noise in terms of their spectral density, giving the possibility to distinguish between Lorentzian and singular  $1/f$  noise.

Finally, and most importantly, the noise power spectral density is nothing else than the fingerprint of a specific noise source. As follows, we will discuss on the relation between longitudinal and dephasing rates and the power spectrum density of the most important noise sources in superconducting qubits.

### 3.3 Effect of noise sources in superconducting qubit relaxation

As discussed in section 3.1, the longitudinal relaxation rate,  $\Gamma_1 = 1/T_1$ , describes depolarization along the qubit quantization axis, often referred to as “energy decay” or “energy relaxation”. It is caused by exchange of energy with the environ-

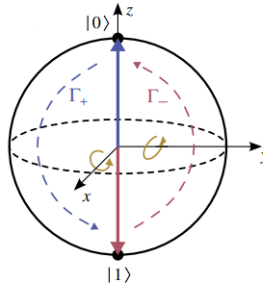


**Figure 20:** Longitudinal relaxation: excitation rate from  $|0\rangle$  to  $|1\rangle$  in dashed blue and relaxation rate from  $|1\rangle$  to  $|0\rangle$  in dashed red [28].

ment, leading both to excitation and relaxation of the qubits, i.e.:

$$\Gamma_1 = \Gamma_- + \Gamma_+. \quad (77)$$

Due to Boltzmann statistics and the fact that superconducting qubits are operated at low temperatures ( $T \leq 20 \text{ mK}$ ) and with a qubit frequency in the GHz regime, the excitation rate  $\Gamma_+$  is suppressed [28]. Starting from equation 70, we will now identify the principal noise sources, which induce relaxation and give an expression of their relaxation rates [11].

- **Spontaneous emission:** The first possible relaxation channel is through spontaneous emission due to the fact that the qubit is coupled with the elec-

tromagnetic field inside the transmission line resonator. The noise operator will be the electric dipole  $\hat{d}$  of the transmon, which can be evaluated as  $d = 2eL$ , where  $L$  is the distance between the two superconducting islands, typically  $15 \mu m$  ([11]). As a result, by applying equation 70, the decay rate for excited transmon level due to emission of radiation is:

$$\Gamma_1^{\text{rad}} = \left| \langle 0 | \hat{d} | 1 \rangle \right|^2 \frac{\omega_{01}^3}{12\pi\epsilon_0\hbar c^3} = \frac{d^2\omega_{01}^3}{12\pi\epsilon_0\hbar c^3}. \quad (78)$$

Typical relaxation times due to spontaneous emission are of the order of 0.3 ms ([11]).

- **Purcell noise:** When a system is placed inside a resonator, its spontaneous emission rate is altered. This effect is known as the Purcell effect. As pointed out in section 2.8, readout resonators in transmon qubits experiments are CPW, whose characteristics are determined by the material and geometry [29].

In the frame of the Purcell noise, a special role is played by the resonator quality factor  $Q$ . The quality factor is defined by the ratio of the energy stored in the resonator to the average energy loss per cycle times  $2\pi$  [30]. We can distinguish between internal and coupling losses, which correspond to the intrinsic quality factor  $Q_i$  and the external or coupling quality factor  $Q_c$ , respectively. [30]. The former is related to photon losses because of the superconducting material used, while the latter takes into account the coupling between the resonator and the external electronics [30], [29]. When evaluating the Purcell decay rate, we must consider the total loaded quality factor, obtained as [30]:

$$\frac{1}{Q_l} = \frac{1}{Q_i} + \frac{1}{Q_c}. \quad (79)$$

As a matter of fact, by using the expression in equation 70, we obtain the following decay rate due to Purcell effect:

$$\Gamma_{1,\kappa} = \kappa |\langle 0 | \hat{a} | 1 \rangle|^2, \quad (80)$$

where  $\hat{a}$  is the annihilation operator for the resonator and  $\kappa = 2\pi\hbar p(\omega_k) |\lambda_k|^2$  corresponds to the noise power spectral density. Here,  $p(\omega_k)$  is the state density of the reservoir and  $\lambda_k$  determines the coupling strength of the resonator to this bath mode. The factor  $\kappa$  can also be written as  $\kappa = \frac{\omega}{Q}$ , where  $Q$  the resonator total quality factor [30]. In the dispersive limit, discussed in section 2.8, the spontaneous emission rate due to Purcell effect is [11]:

$$\Gamma_{1,\kappa} = \kappa \frac{g_{01}^2}{\Delta_0^2}. \quad (81)$$

In transmon circuits, superconducting readout resonators are characterized by large intrinsic quality factors ( $Q_i = 10^6$ ) [30], [29]. Indeed, there is a strong effort in the search for novel materials to improve the quality of readout resonators. Niobium-based resonators, with  $Q_i \simeq 10^7$  [31], were proven to be more efficient than Aluminium-based ones, with  $Q_i \simeq 10^3$  [32]. Lately, new combination of these materials has been investigated [33], in particular with a new interest in Tantalum-based devices [34], [35].

However, the need for an external readout circuitry, like for multiplexed readout of multi-qubit systems [8], make the coupling quality factor  $Q_c$  order of magnitudes lower than  $Q_i$  [30]. Therefore, the resonator losses are typically dominated by  $Q_c$ , and the loaded quality factor is of the order of  $10^4$ , i.e.  $1/\kappa = 160ns$  [11]. In the dispersive regime, for typical values of the ratio  $\frac{g_{01}}{\Delta_0} = 0.1$ , Purcell effect results in a relaxation time of  $16 \mu s$  [11], thus being one of the most important noise sources in transmon qubits.

- **Dielectric losses:** This noise derives from the charge fluctuations present in the defects or charge traps that resides in interfacial dielectrics, the junction tunnel barrier and in the substrate of the qubit [11]. The electric field is transverse with respect to the quantization axis, so this type of noise is mainly responsible for energy relaxation ( $T_1$ ). The noise spectral density can be written as [27]:

$$S_{diel}(\omega) = \frac{\omega \hbar}{|\omega| C_J Q_{cap}(\omega)} \left( 1 + \coth \frac{\hbar |\omega|}{2k_B T} \right). \quad (82)$$

Here,  $C_J$  is the junction capacitance,  $T$  is the temperature and  $Q_{cap}(\omega)$  [26] is the dielectric quality factor.  $Q$  is linked to the loss tangent of the dielectric as [26], [27]:

$$Q_{cap} = 1 / \tan \delta_C. \quad (83)$$

The electric loss tangent  $\tan \delta_C$  is defined as the ratio between the real and the imaginary part of the electric permittivity  $\epsilon$  and quantifies the dielectric material's dissipation of electromagnetic energy [26]. Typically,  $Q_{cap} \approx 10^6$  [26].

From equation 70, we can evaluate the relaxation time as [26], [27]:

$$1/T_1(\omega) = \frac{1}{\hbar^2} |\langle 0 | 2e\hat{n} | 1 \rangle|^2 S_{diel}(\omega). \quad (84)$$

Depending on the dielectric loss tangent  $\tan \delta_C$ , the relaxation time due to dielectric losses goes from tens of  $\mu s$  to some  $ms$  [27].

- **Quasiparticle noise:** The presence of quasiparticles in the system, due to an overall odd number of electrons or thermal breaking of Cooper pairs, mentioned in section 2.3, leads to relaxation in qubits based on JJs. The corresponding noise operator is the tunnelling Hamiltonian  $\hat{H}_T$  [36], [37]. It can be proven that the number of quasiparticles for temperatures small compared to the superconducting gap  $\Delta$  may be obtained as [11]:

$$N_{qp} = 1 + \frac{3\sqrt{2\pi}}{2} N_e \frac{\sqrt{\Delta k_B T}}{E_F} \exp\left\{-\frac{\Delta}{k_B T}\right\}, \quad (85)$$

where  $N_e$  is the total number of quasiparticles with conduction density  $n$  in the superconducting electrodes volume  $V$ . The rate of tunnelling for one quasiparticle across the junction is given by  $\Gamma_{qp} = (1/\nu V)g/4\pi\hbar$ , where  $\nu$  is the energy density of state (DoS) and  $g$  is the quasiparticles tunnel probability, which can be quantified in terms of the tunnel conductivity of quasiparticles through the barrier of a JJ [38]. The smaller is the quasiparticles conductance, the smaller will be the quasiparticles decay rate, defined as [11]:

$$\Gamma_1 = 1/T_1 = \Gamma_{qp} N_{qp} \sqrt{\frac{k_B T}{\hbar\omega_{01}}} |\langle g, n_g \pm 1/2 | e, n_g \rangle|^2. \quad (86)$$

Here, the matrix element is the Franck-Condon factor, which accounts for the agitation of the transmon collective mode due to the tunnelling of one quasiparticle [11]. The quasiparticles conductance in typical tunnel aluminium JJs in transmon circuits can be calculated as  $1/R_{subgap}$ , where  $R_{subgap}$  has been defined in section 2.3.  $R_{subgap}$  is of the order of  $M\Omega$ , thus providing typical a relaxation time for a transmon qubit of  $T_1 \approx 1s$  [11]. In addition, from the temperature dependency of  $T_{1qp}$ , we observe that this noise source is negligible for temperatures below 100 mK. Therefore, at cryogenic temperatures, quasiparticles should not lead to significant contributions to relaxation [11] (figure 21).

- **Flux coupling noise:** The coupling of the transmon to an external magnetic flux bias allows for an *in situ* tuning of the Josephson coupling energy, but also opens up additional channels for energy relaxation if it is resonant with the transition frequency of the qubit. We can distinguish between two decay channels: the first one caused by the intentional coupling between the SQUID loop and the flux bias via the mutual inductance  $M$  and the second one related to the coupling between the entire transmon circuit and the flux bias via the mutual inductance  $M'$ . In the first case, by treating the noise perturbatively and applying equation 70, we can relate the relaxation rate to the

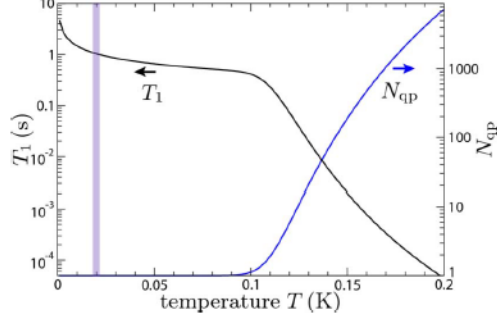


**Figure 21:** Number of quasiparticles and contributions to the relaxation time due to inelastic quasiparticle tunnelling as a function of temperature, the vertical line is the typical cryogenic temperature at which qubit measurements are made, i.e. 20 mK [11].

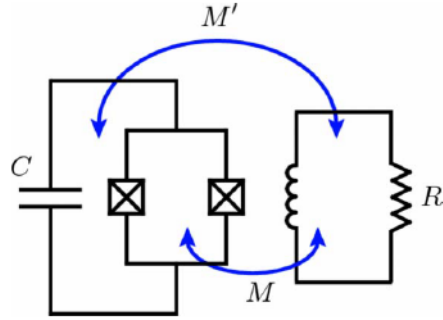


**Figure 22:** Circuit schematics for flux coupling [11]: flux coupling between the transmon's SQUID loop and the external flux bias with mutual inductance  $M$ , and flux coupling between the transmon circuit and an external flux bias circuit via the mutual inductance  $M'$ .

noise power spectrum, as [11]:

$$\Gamma_1 = \frac{1}{T_1} = \frac{1}{\hbar^2} \left| \langle 1 | \frac{\partial \hat{H}_J}{\partial \Phi} | 0 \rangle \right|^2 M^2 S_{I_n}(\omega_{01}), \quad (87)$$

where  $\hat{H}_J$  is the split-transmon Hamiltonian (equation 45), and we have used the relation between the flux noise and current noise  $S_{\Phi}(\omega) = M^2 S_{I_n}(\omega)$ . At low temperatures,  $k_B T \ll \hbar \omega_{01}$  the current quantum noise is given by [11]:

$$S_{I_n}(\omega) = 2\Theta(\omega)\hbar\omega/R, \quad (88)$$

where  $R$  is the environmental impedance of approximately  $50\Omega$ . The maxi-

mum  $T_1$  is reached for an integer number of flux quanta through the SQUID loop [11]. If  $E_J = 20 \text{ GHz}$ ,  $E_C = 0.35 \text{ GHz}$  and  $M = 140\Phi_0/A_\Phi$ , we obtain relaxation times between 20 ms and 1s [11]. For the second channel, the contribution to  $T_1$  can be calculated by evaluating the average power dissipated by the environmental impedance  $R$  and using a semi-classical approximation as [11]:

$$T_1 \simeq \frac{\hbar\omega}{P} = \frac{R}{M'^2\omega^2C} = \frac{RC}{\eta^2}. \quad (89)$$

Here,  $\eta = \frac{M'}{L}$  measures the effective coupling strength in units of the Josephson inductance. For  $R = 50 \Omega$ ,  $M' = 10\Phi_0/A_\Phi$  and the same values of  $E_J$  and  $E_C$  used before, we obtain times of the order of tens of ms [11]. In conclusion, relaxation by flux coupling does not usually limit the performance of a transmon qubit [11].

### 3.4 Effect of noise sources in superconducting qubit dephasing

In section 3.1, we defined the dephasing rate  $\Gamma_\phi$  as the rate of depolarization on the x-y plane induced by longitudinal coupled noise, as shown in figure 23. This

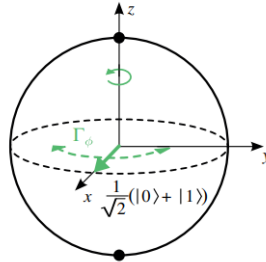


**Figure 23:** Pure dephasing rate induced by longitudinal noise: a state  $|\psi\rangle = \frac{1}{\sqrt{2}}(|0\rangle + |1\rangle)$  induced to rotate on the equatorial plane with the rate  $\Gamma_\phi$  [28].

section aims at introducing the noise sources which contributes to pure dephasing basing on their power spectrum.

As discussed in section 3.1, dephasing is due to the broadening of the transition frequency of the qubit, induced by noise sources longitudinally coupled to the qubit. Starting from this consideration, we will focus on the noise sources that can modify the transition frequency of a split-transmon, which depends on  $E_C$  and  $E_J$ . Given the tunability of  $E_J$  as a function of an external flux in split-transmon which is tuned by an external flux bias, the most important noise sources are related to

charge, current and flux noise.

It has been proven that in the case of the transmon qubit, charge, current and flux noise sources have a  $1/f$  spectrum and contributes to dephasing at low frequencies [11], see also equations 75, and 76 [11].

- **Charge noise:** It derives from fluctuations of the charge in the superconducting islands of a JJ. At low frequency, charge noise is a  $1/f$  type and its spectral density takes the form [11]:

$$S_Q(\omega) = A_Q^2 \frac{2\pi}{|\omega|}, \quad (90)$$

where  $A_Q$  is the charge noise amplitude, typically  $A_Q = 10^{-4} - 10^{-3}e$  in a transmon [11]. As a result, we derive the contribution to  $T_\phi$  from equation 76 as:

$$T_\phi \sim \frac{\hbar}{A_Q \pi |\epsilon_1|}. \quad (91)$$

For state-of-the-art transmon qubits, we expect the charge dispersion  $\epsilon_1$  to be small and the resulting  $T_2$  to be large [11]. For example, for  $E_J = 30 \text{ GHz}$ ,  $E_C = 0.35 \text{ GHz}$ ,  $A_Q = 10^{-4}$ , we obtain  $T_\phi = 8 \text{ s}$  [11], proving that the transverse decay rate is only determined by the longitudinal relaxation time (equation 66).

This statement is further proved considering the dependence of  $T_2$  as a function of the ratio  $E_J/E_C$  in figure 24, simulated by using the Python package *scqubits* [12]. By changing the ratio  $E_J/E_C$  from 10 to 100, we obtain that  $T_2$  due to charge noise spans from 10 to 60  $\mu\text{s}$ , as shown in the simulation in figure 24. Since we are in the transmon regime, i.e.  $E_J/E_C \simeq 50$ , the longitudinal decay time is of the order of tens of  $\mu\text{s}$ .

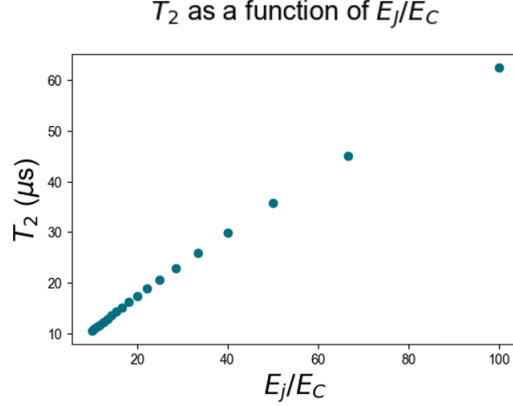


**Figure 24:** *Scqubits* [12] simulation of  $T_2 = 1/(1/(2T_1) + 1/T_{\phi,charge})$ , taking into account only charge noise for dephasing, as a function of the ratio  $\frac{E_J}{E_C}$

This proves that, thanks to the additional shunt capacitance, which makes the charge energy smaller and thus the ratio  $\frac{E_J}{E_C}$  larger, charge noise has been partially suppressed [11].

- **Flux noise:** It arises from the stochastic flipping of spins (magnetic dipoles) that reside on the surface of superconducting metals [11]. In the case of the tunable transmon qubit, the external magnetic field couples to the qubit and modulates the transition frequency. Typically, the flux noise is longitudinal to the transmon, so it contributes to pure dephasing ( $T_\phi$ ). At low frequency, it is a  $1/f$  noise and its spectral density is [11], [7]:

$$S_{\phi_{\text{ext}}} = A_{\phi_{\text{ext}}}^2 \left( \frac{2\pi}{|\omega|} \right)^{\gamma_{\phi_{\text{ext}}}}, \quad (92)$$

where  $\gamma_{\phi_{\text{ext}}} = 0.8 - 1$  [7]. By using the Mathieu's eigenvalues of the transmon Hamiltonian and equation 76, we find the resulting dephasing time [11]:

$$T_\phi = \frac{\hbar}{A_\Phi} \left| \frac{\partial E_{01}}{\partial \Phi} \right|^{-1} = \frac{\hbar \Phi_0}{A_\Phi \pi} \left( 2E_C E_{J\Sigma} \left| \sin \frac{\pi \Phi}{\Phi_0} \tan \frac{\pi \Phi}{\Phi_0} \right| \right)^{-1/2}, \quad (93)$$

valid for  $E_J \gg E_C$ , alias the transmon regime. For a flux bias of  $\Phi = \Phi_0/4$  and an amplitude of  $A_\Phi = 10^{-5}$ , we obtain a dephasing time of the order of approximately  $1 \mu s$  [11]. We note that for  $\Phi = n\Phi_0$ , with  $n$  integer, the dephasing time diverges. These points are known as sweet spots for the flux, where the slope  $\frac{\partial \omega}{\partial \Phi}$  is zero and second order transitions dominate. Here,  $T_\phi$

can be evaluated as [11]:

$$T_\phi \simeq \left| \frac{\pi^2 A^2}{\hbar} \frac{\partial^2 E_{01}}{\partial \Phi^2} \right|_{\Phi=0}^{-1} = \frac{\hbar \Phi_0^2}{A^2 \pi^4 \sqrt{2 E_{J\Sigma} E_C}}, \quad (94)$$

obtaining a dephasing time of some ms [11].

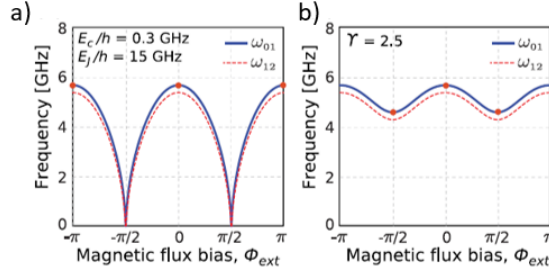


**Figure 25:** Comparison between the two first transition frequencies,  $\omega_{01}$  in blue and second transition frequency  $\omega_{12}$  in dashed red, as a function of the external magnetic flux  $\Phi_{ext}$ , in units of the flux quantum, for symmetric (a) and asymmetric (b) tunable transmon, with and  $\gamma = 2.5$ , both with  $E_J/EC = 50$  [7].

Although the possibility to operate the transmon in their sweet-spots in order to take advantage of the reduced sensitivity to flux noise is massively employed in the field [11], certain applications still require tuning the qubit far from the sweet-spots. For example, the typical protocol used in two-qubit systems coupled by fixed high-frequency bus resonators, as those used in advanced systems for Quantum Error Correction [39] and also in this work, requires putting on resonance two qubits by means of an external flux modulation. The drawback related to the tunability far from the sweet-spot is an increasing sensitivity to flux noise.

The transmon sensitivity to flux noise can be reduced, while maintaining the tunability, by making the two junctions of the SQUID asymmetric, i.e. by including in the DC SQUID two JJs with different critical currents  $I_{C_1}$  and  $I_{C_2}$  (figure 25). In this case, the SQUID Josephson energy reads as [7]:

$$E_J(\Phi) = E_{J\Sigma} \cos \frac{\pi\Phi}{\Phi_0} \sqrt{1 + d^2 \left( \tan \frac{\pi\Phi}{\Phi_0} \right)^2}, \quad (95)$$

where  $E_{J\Sigma} = E_{J_1} + E_{J_2}$  and  $d = \frac{\gamma-1}{\gamma+1}$ , with the SQUID asymmetry parameter  $\gamma = \frac{E_{J_1}}{E_{J_2}}$  [7]. As we can see from figure 25, both for symmetric and

asymmetric transmon the resonance frequency modulates as  $|\cos \phi|$ , but in the asymmetric case the slope at the semi-periods is reduced, and thus flux noise is minimized. In order to stress this point, we report, in figure 26, a simulation *scqubits* [12] of the dephasing time due to flux noise as a function of the flux bias, for a symmetric (a) and an asymmetric (b) split-transmon, with the following parameters:  $E_J = 30 \text{ GHz}$ ,  $E_C = 0.35 \text{ GHz}$  and  $A_\Phi = 10^{-5}$ .

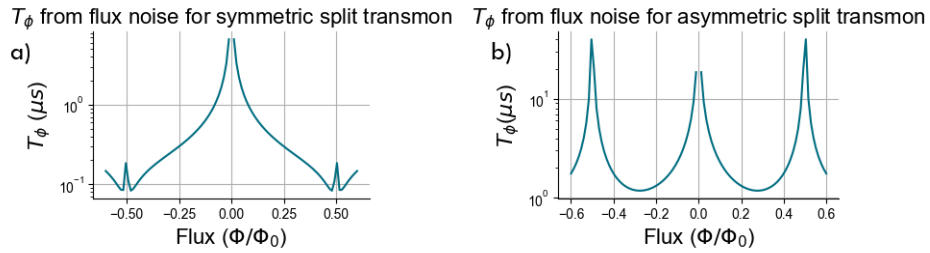


**Figure 26:** *scqubits* [12] simulation of the dephasing time due to flux noise as a function of the external flux in units of the flux quantum for a) symmetric split transmon, b) asymmetric split-transmon, with  $d = 0.6$ ,  $E_J = 30 \text{ GHz}$ ,  $E_C = 0.35 \text{ GHz}$  and  $A_\Phi = 10^{-5}$ .

The introduction of an asymmetry in the DC SQUID allows to reduce the effect of flux noise far from the sweet-spot, as can be observed in figure 26 (b). We can see that, at the semi-integer multiples of  $\Phi_0$ , the dephasing time is orders of magnitude larger than in the symmetric case, reported in 26 (a), and approximately the same of the one at integer multiples of  $\Phi_0$ . In this thesis, we will measure a symmetric transmon, so flux-noise is likely to be an important noise source.

- **Critical current noise:** Another source of fluctuations of the Josephson energy consists of noise in the critical current, which is generated by trapping and detrapping of charges associated with spatial reconfigurations of ions inside the tunneling junction [11]. This influences the critical current and hence the Josephson energy. By using equation 76, the resulting dephasing time can be evaluated as [11]:

$$T_\phi \approx \frac{2I_C \hbar}{A_{I_C} E_{01}}. \quad (96)$$

For  $A_{I_C} = 10^{-6} I_C$  [11] and the same values of charge and Josephson energy used before, we obtain typical dephasing times ranging from tens to hundreds of  $\mu\text{s}$ , depending on the external flux field [11], as pointed out in figure 27.

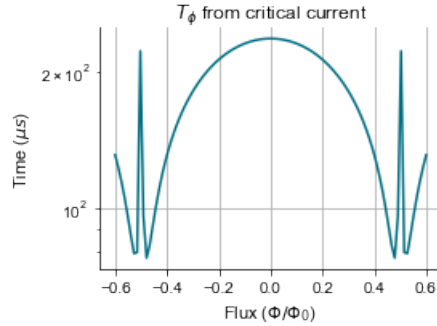


**Figure 27:** *scqubits* [12] simulation for dephasing due to critical current as a function of the external flux in units of the flux quantum with  $A_{I_C} = 10^{-6} I_C$ ,  $E_J = 30 \text{ GHz}$ ,  $E_C = 0.35 \text{ GHz}$ .

### 3.5 Summary

In conclusion, a qubit is exposed to various noise sources, and thanks to the Bloch-Redfield model we can understand how each of them contribute to decoherence, including both energy relaxation and dephasing. By studying the noise power spectral density, we are able to study a noise source and evaluate the resulting depolarization time.

Moreover, by using the typical parameters of a state-of-the-art split-transmon coupled to a superconducting readout resonator, we found that the relevant noise sources causing relaxation are Purcell noise and dielectric losses noise, as one can see from the summary table 1. For what concerns dephasing, we obtained that the main noise sources to take in consideration are flux noise and critical current noise. In chapter 5, we will apply these considerations to the noise analysis of single and coupled split-transmons.

Noise source	$\hat{O}_{\text{noise}}$	Noise spectral density	Decoherence time
<i>Relaxation</i>			
Spontaneous emission	$\hat{d}$	$\propto \frac{d^2 \omega_{01}^3 \hbar}{\pi \epsilon_0 c^3}$	$T_1 \simeq 0.3 \text{ ms}$ [11]
Purcell effect	$\hat{a}$	$\propto \frac{\omega}{Q_{\text{resonator}}}$	$T_1 \simeq 16 \mu\text{s}$ [11]
Dielectric losses	$2e\hat{n}$	$\propto \frac{\omega \hbar}{C_J Q_{\text{cap}}(\omega)}$	$T_1 \simeq 1 \mu\text{s} - 18 \text{ ms}$ [27]
Quasiparticle tunnelling	$\hat{H}_T$	$\propto \Gamma_{\text{qp}} N_{\text{qp}} \sqrt{\frac{k_B T}{\hbar \omega_{01}}}$	$T_1 \simeq \infty$ [11]
Flux bias line	$\frac{\partial \hat{H}_J}{\partial \Phi}$	$\propto M^2 \Theta(\omega) \hbar \omega / R$	$T_1 \simeq 20 \text{ ms}$ [11]
<i>Dephasing</i>			
Charge offset	$\frac{\partial \hat{H}}{\partial n_g}$	$\propto A_Q^2 \frac{1}{ \omega }$	$T_\phi \simeq 8 \text{ s}$ [11]
Flux	$\frac{\partial \hat{H}}{\partial \Phi}$	$\propto A_{\phi_{\text{ext}}}^2 \frac{1}{ \omega }$	$T_\phi \simeq 1 \mu\text{s} - 1 \text{ ms}$ [11]
Critical current	$\frac{\partial \hat{H}}{\partial I_C}$	$\propto A_{I_C}^2 \frac{1}{ \omega }$	$T_\phi \simeq 35 \mu\text{s}$ [11]

**Table 1:** Principal noise sources and their decoherence effect for a split-transmon qubit.

## 4 Experimental setup

The study of the decoherence processes in superconducting qubits requires an enormous care when dealing with the experimental setup and the measurements protocols. As a matter of fact, it is mandatory to provide an experimental platform able to protect the qubit from the environmental noise sources, while still being able to access their behaviour. We will first describe the device analyzed in this work (section 4.1). Then, in section 4.2, we will discuss on the working principle of dilution refrigerators, used to cool down transmon qubit devices down to few millikelvins. Finally, we will report the cryogenic and room-temperature electronics (sections 4.3.1 and 4.3.2) used to acquire the data reported in this work, and the characterization methods (sections 4.3.3 and 4.3.4).

### 4.1 Chip design

The chip we measured and characterized in this thesis is realized by Quantware in collaboration with the University of Napoli Federico II and Seeqc-EU company. It is made of 6 tunable transmons, 5 of them coupled and one single-qubit. Qubit 2 is coupled by a resonator with qubit 0, qubit 1, qubit 3 and qubit 4, as shown in figure 28 (a). Qubits 0 and 1 are designed to have the lowest frequencies, qubit 2 a medium frequency, and qubits 3 and 4 the highest frequencies. This schematic is typical of state-of-the-art devices, in particular quantum error correction systems [39].

The JJs in the qubit, figure 28 (c), are made of Aluminium electrodes and  $AlO_x$  barrier, while the resonators are Niobium-Titanium Nitride. The junctions are located in a DC SQUID and are made to be symmetric.

In section 2.6, we pointed out that the transmon circuit is characterized by a large shunt capacitance, in order to make the ratio  $\frac{E_J}{E_c}$ . This capacitance is represented by the pads in yellow in figure 28 (b).

In this work, we will focus on the characterization of qubit 2 and qubit 4. In particular, we will analyze the coherence properties of the single-qubits, starting from single-qubit measurements, which will be discussed in section 4.3.3. Then, we will observe the coupling between them through the avoided level crossing, described in section 2.9.

The RF lines on the chip are Coplanar Waveguide (CPW) and use Transverse Electromagnetic Modes (TEM). In order to apply an external flux to the DC SQUID and tune the qubit frequency, CPW flux lines in figure 28 (a) are inductively coupled to the DC-SQUID loop in the transmon. The drive lines and the resonators are capacitively coupled to the qubits.

As we can see from figure 28 (a), all the qubits are equipped with a readout res-

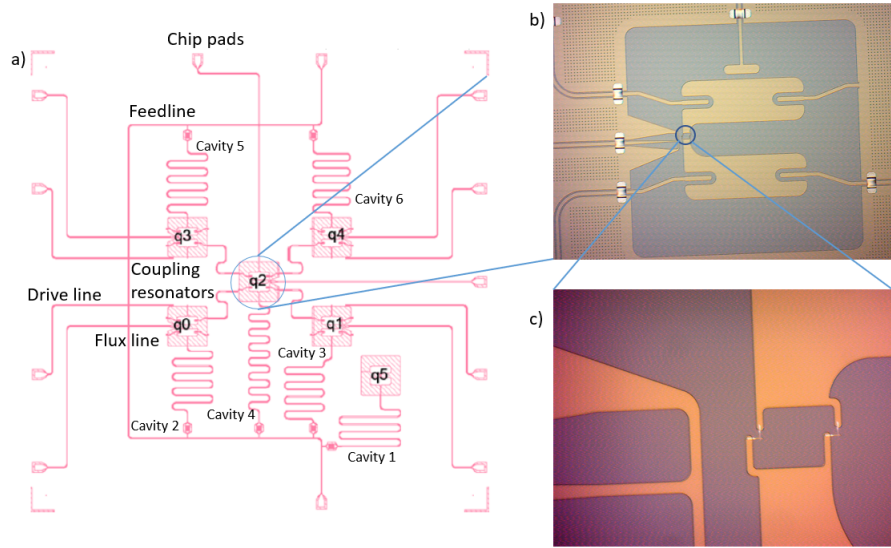


**Figure 28:** In a), qubit chip design analyzed in this work. Here highlighted five intercoupled transmon qubits and a single transmon-qubit, the corresponding readout resonators (cavities), the drive and the flux lines for qubit control and tuning, and the feedline for simultaneous qubit multiplexing readout. In b), SEM image of central qubit 2, while in c) we show a zoom on the DC-SQUID in the transmon. SEM images are courtesy of Seeqc quarters in London, while the circuit design has been provided by QuantWare.

onator. Each resonator is capacitively coupled through an elbow coupling to a transmission line used for readout, called feedline. It is designed to allow multiplexing, i.e. we can control multiple readout resonators by sending signal with different frequencies. The resonators are coupled to the feedline through elbow-shaped coupling capacitors, which allows maximizing the electric part of the signal.

The length and the shape of the resonator determine its characteristics, such as the resonance frequency and the quality factor, as discussed in section 3.3.

Resonators can be measured either in reflection or transmission. For a transmission measure, it is impossible to directly determine the internal losses of the resonator by probing the resonator's transmission due to the missing reference baseline [30]. In a reflection measurement instead, we can evaluate the losses due to the coupling with a transmission line, and thus the external quality factor. Therefore, we measure the resonators in reflection, by choosing a so-called notch type geometry [30], where the resonator is coupled to the transmission line, as shown in figure 4.1. In this case, the coupling quality factor  $Q_c$  takes into account the losses due to the coupling with the external environment through the feedline, while the internal

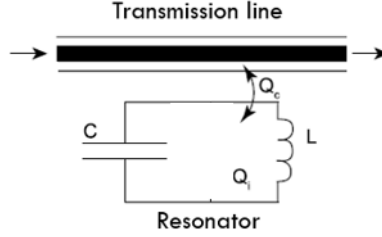


**Figure 29:** Coupling quality factor for a notch port geometry: an LC resonator is coupled to the transmission line [30]

quality factor  $Q_i$  takes into account the internal losses in the resonator. The characteristic parameters by design of qubits 2 and 4 and their readout cavities are reported in table 2.

Qubit	$\omega_{r, bare}$ (GHz)	$E_J$ (GHz)	$E_C$ (GHz)	$\omega_{01}$ (GHz)	$g$ (GHz)	$\chi$ (MHz)
2	7.6	16	0.27	5.6	1.18	0.737
4	8	21	0.27	6.5	0.108	1.18

**Table 2:** Design frequencies and energies of the qubits characterized in this thesis and bare frequencies of the corresponding cavities.

In order to protect the chip from environmental noise, it is provided of several shields. First, it is placed inside a package provided by Quantware, which consists of a copper cavity for infrared radiation protection. Then, we find a superconducting thin shield, which protects the chip from external magnetic radiations thanks to Meissner effect, discussed in section 2.2. Finally, the package is surrounded by cryoperm, a soft magnetic nickel-iron alloy, covered in copper, for infrared radiations protection. Cryoperm is superconducting, and specifically designed for magnetic shielding.

In order to reach the critical temperatures of the superconductors cited in this section, the chip is connected to the coldest plate of a dilution refrigerator, whose base temperature is 10 mK.

## 4.2 Dilution refrigerator

As discussed in Chapter 2, superconducting qubit characterization requires reaching temperatures down to 10 mK, a lot cooler than the transition temperature of the superconductors used in the circuit. This choice is made to protect the sample

from environmental noise. As discussed in section 3.1, qubits are very sensitive objects and external noise sources can induce decoherence and relaxation. Moreover, since the qubit frequencies usually fall in the few GHz range, temperatures far lower than 200 mK are needed in order to avoid transitions from the ground state to the first excited state in the transmon [11].

In order to reach this goal, we use a dry dilution cryostat, the Bluefors dilution refrigerator (DR) [40], shown in figure 30. The Bluefors is composed of six copper gold-plated plates, thermally decoupled one from each other by means of Stainless-Steel (SS) supports [40], as we can see in figure 30:

- the RT-plate at room temperature;
- the PT1, at  $\sim 50\text{ K}$ ;
- the PT2, at  $\sim 4.2\text{ K}$ ;
- the still plate, at  $\sim 700\text{ mK}$ ;
- the IAP-plate, at  $\sim 100\text{ mK}$ ;
- the MC-plate, at  $\sim 10\text{ mK}$ .

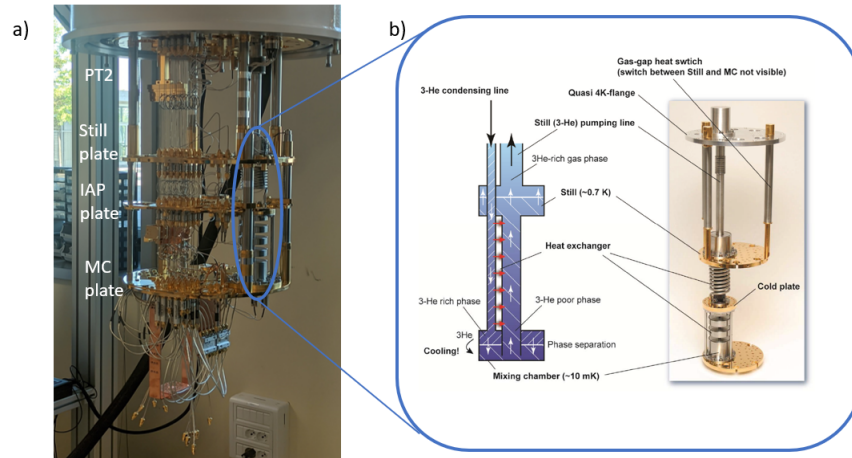


**Figure 30:** a) Bluefors dilution cryostat in the CESMA-Seeqc Quantum Joint Lab of the University of Napoli Federico II with the main cooling stages. b) Focus on the dilution unit of the cryostat and schematics of the main cryogenic stages in the dilution process.

First, the system must be placed in a vacuum chamber, an enclosure which thermally and mechanically protects all the cold parts of the system. Inside the common vacuum space, in order to thermally isolate it from its surroundings, there are

three steel shields and one copper shield for high frequency and infrared radiation. The refrigeration process uses a mixture of two isotopes of helium:  $^3\text{He}$  and  $^4\text{He}$ . When cooled below approximately  $870\text{ mK}$ , the mixture undergoes spontaneous phase separation and divides into a  $^3\text{He}$ -rich phase (the concentrated phase) and a  $^3\text{He}$ -poor phase (the diluted phase), as shown in figure 31. This separation is an endothermic process, that allows to lower the temperature to tens of millikelvin. The main cooling phases of the dilution refrigerator are: the precooling, the condensation, the dilution and the circulation.

- **Precooling:** First there is a cold trap at  $\sim 50\text{K}$ , which both cleans the  $^3\text{He}$ - $^4\text{He}$  mixture by freezing eventual contaminant particles and serves as heat exchanger. At this stage, the mixture is a gas, which is pre-cooled at the second cold plate (PT2) at  $< 4.2\text{K}$ , thanks to a Pulse Tube Refrigerator (PTR). At  $4.2\text{K}$ , the  $^4\text{He}$  becomes liquid. This is helped by different heat exchangers.
- **Condensation:** In order to start the condensation, the pressure of the helium mixture is raised to about 2 bar. The heat exchangers in the condenser line cool the pressurized mixture to low enough temperature for the  $^4\text{He}$  to condense (because of the Joule-Thomson effect). At this stage, the  $^3\text{He}$  is still gaseous, so the mixture passes through an impedance, where  $^3\text{He}$  undergoes isoenthalpic expansion and reaches its condensation temperature of  $1.7\text{ K}$ . The  $^3\text{He}$  and  $^4\text{He}$  mixture is now in the liquid phase.
- **Mixing and dilution:** Now the mixture is pumped by turbo and rotative pumps and then by a  $^3\text{He}$  compressor. In this way, the temperature drops below  $0.8\text{K}$ . As reported in the phase-diagram in figure 31, the phase separation occurs in the mixing chamber, due to the enthalpy difference between the concentrated (incoming) and the diluted (outgoing) liquid. The first liquid is pure  $^3\text{He}$ , the second one is predominantly  $^4\text{He}$  with a small fraction of  $^3\text{He}$ . The heat necessary for the dilution is the cooling power of the refrigerator, because this process is endothermic and removes heat from the mixing chamber environment. Therefore, the temperature of the plate at which the mixing chamber is thermally and mechanically anchored, the MC plate, is the coldest one, with a base temperature of  $10\text{ mK}$ .
- **Circulation:** After the phase separation, the diluted  $^3\text{He}$  flows from the mixing chamber to a chamber called still, located at the still plate. The  $^3\text{He}$  evaporates and circulates thanks to the pumping system towards the hottest plates, and then at room temperature. This phase is called circulation. On its way up, the diluted  $^3\text{He}$  cools the flowing concentrated  $^3\text{He}$  via the heat ex-

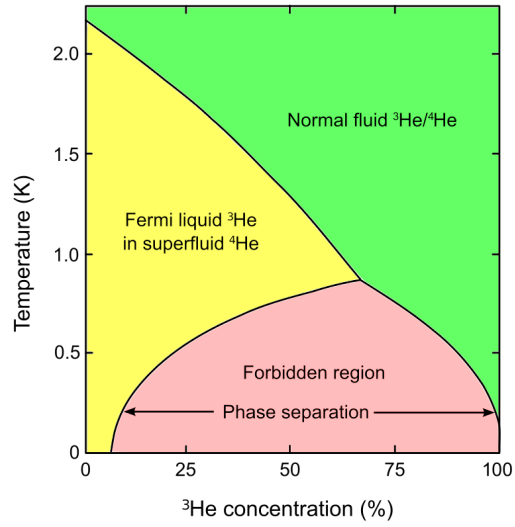


**Figure 31:** Phase-diagram of the  ${}^3\text{He}$ - ${}^4\text{He}$  mixture: dilution occurs under 0.8K. When the mixture reaches this threshold, we have the separation into a diluted and a concentrated phase.

changes and enters the still, restarting the cycle. This closed loop maintains the cooling process active.

### 4.3 Electronics and measurement protocols

In order to characterize transmon qubits, we exploited a wide range of investigation protocols that use radio-frequency (RF) signals, both continuous or made by complex sequences of pulses. The main motivation relies on the requirement to resonate with both the readout resonators and the qubit itself, characterised by frequencies of the order of 4-8 GHz. As follows, we will first report details about the cryogenic electronics employed in this thesis, then we will focus on the room-temperature electronics. Finally, we will give a comprehensive showcase of the measurement protocols employed, with a specific focus on coherence time-domain measurements.

#### 4.3.1 Cryogenic electronic setup

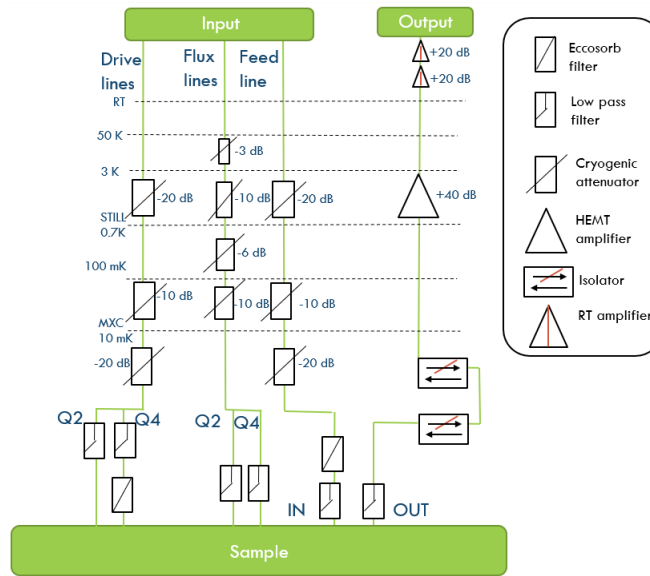


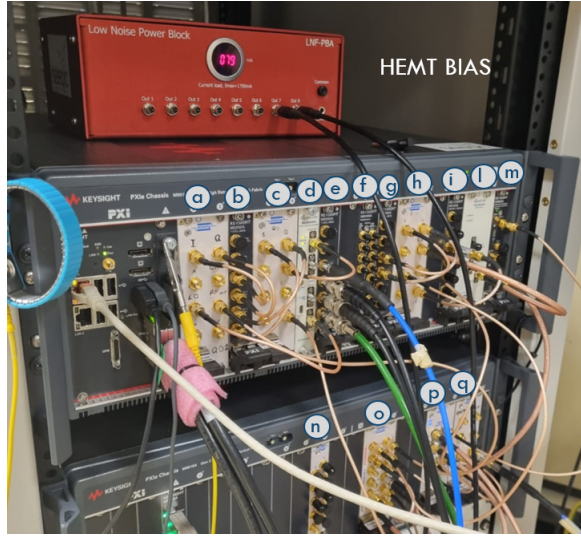
**Figure 32:** RF cryogenic setup: in input, we find the drive lines and the flux lines of qubit 2 and qubit 4, and the feedline, with all the corresponding attenuators and filters; in output, we have the isolators and filters, then the HEMT amplifier and the Room Temperature amplifiers.

The cryostat is provided of RF input and output lines, thermally anchored to the different plates of the cryostat. The input lines are made of stainless steel, while the output lines are made of superconducting Nb-Ti, from the 4K plate to the MC, and copper at higher temperatures. In superconducting transmon qubits, the main requirement is to work in a single-photon regime, for both the QND readout

and the control signals. Therefore, the input signals are attenuated by 50 dB by the attenuators placed on the plates of the cryostat. Moreover, the stainless steel of the input lines attenuates the signal by 10-20 dB in the 4-8 GHz range (figure 32). In addition, a complex scheme of low-pass filtering is implemented. We use 10 GHz low-pass coaxial RF filters for the feedline and the control lines, while a lower cutoff frequency is used for the flux lines. As a matter of fact, flux lines work either in a DC mode operation or in pulsed mode, with pulses frequencies much lower than 1 GHz. Additional eccosorb filters are mounted on a limited number of lines in order to cutoff spurious signals in the high-GHz regime ( $> 10$  GHz). Such filtering schematics is fundamental in order to suppress spurious stochastic noise arising from the interaction with the radiative environment, which may be detrimental for qubit coherence.

The signal response of qubit is typically very weak, so it needs to be amplified. We use a HEMT (High Electron Mobility Transistor) [41] amplifier at 4 K, biased by a power supply LNF-PBA from Low Noise Factory [42]. The HEMT works with 40 dB of amplification from 4 to 8 GHz. This amplifier introduces an additional noise source, which can cause disturbances and spurious waves reflected back to the qubit. Because of this, once the signal comes out of the sample, it passes through two isolators, which prevents the signal to be reflected back to the chip. This device introduces an attenuation of 20 dB on signals coming from room-temperature, and works in a frequency range up to 12 GHz. Finally, we have two amplifiers at room-temperature, with 20 dB amplification each.

### 4.3.2 Room temperature electronics setup



- a) Up conversion card for  $Q_2$
- b) AWG for  $Q_2$  and  $Q_4$
- c) Up conversion card for  $Q_4$
- d) Local oscillator for  $Q_2$  and  $Q_4$
- e) AWG for flux bias
- f) Clock
- g) AWG for readout
- h) Up and down conversion for readout
- i) Digitizer
- l) Local oscillator for readout
- m) VNA
- n) Multiplexer
- o) Attenuators
- p) Switching cards
- q) Amplificators

**Figure 33:** RF setup: Keysight rack with all the modules used for characterization of qubits, and HEMT bias power supply. In the legend are reported the corresponding labels. We note that in the measurements reported in this thesis, we did not use the clock card (f).

The room-temperature experimental setup is equipped with a highly compact and integrated PXI electronics provided by Keysight Technologies, shown in figure 33. The Keysight rack includes signal generation and measurement modules. By using this system, we can generate and measure both continuous and pulsed RF signals.

Continuous measurements use the Vector Network Analyzer (VNA) (figure 33 (m)) in order to perform spectroscopic measurements. This instrument allows measuring the scattering parameters of the device under test (DUT), the reflection and the transmission. The scattering parameters of an electromagnetic wave are mathematically defined as the component of the scattering matrix, related to the transmitted and reflected power at the two ports of a two-terminal DUT. The scattering matrix relates the incident ( $a_1$  and  $a_2$ ) electromagnetic components and the reflected ( $b_1$  and  $b_2$ ) waves at the port 1 and 2 of the DUT (figure 34), and reads as::

$$\begin{pmatrix} b_1 \\ b_2 \end{pmatrix} = \begin{pmatrix} S_{11} & S_{12} \\ S_{21} & S_{22} \end{pmatrix} \begin{pmatrix} a_1 \\ a_2 \end{pmatrix}. \quad (97)$$

Each element of the matrix is a complex number, and the VNA can acquire both real and imaginary parts of the signal. The measurement of the scattering pa-

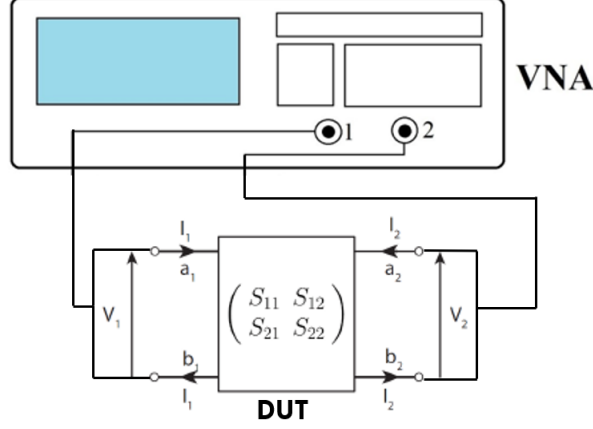


**Figure 34:** VNA schematics: the signal goes from port 1 to the device under test (DUT), and the VNA acquires both the transmitted and the reflected signal at port 1 and 2.

rameters allows having useful information on the readout resonators and the qubit spectroscopy.

In addition to spectroscopic measurements, qubit characterization also requires pulsed protocols in order to perform time-domain measurements. The most important time-domain characterization procedures covered in this thesis (section 4.3.4), like relaxation, Ramsey interferometry and Hahn-echo [7], requires the ability to generate pulses at the typical frequencies of the qubit and resonators, i.e. 4-8 GHz. Instead of using an RF pulse generator in the range of GHz, the signal can be obtained by mixing a Local Oscillator (LO), the higher frequency signal, generated by means of RF signal generators (figure 33 (d) and (l)), and the in-phase (I) and out-of-phase (Q) components of the output of an arbitrary waveform generator (AWG) [43]. The AWG used in the experimental setup, in figure 33 (b) and (g), is able to generate microwave signals with frequencies up to 400 MHz. So, its signal frequency  $\omega_{AWG}$ , also called IF frequency, is a few orders of magnitude smaller than the one of the LO. The mixing is performed by an IQ mixer, located in home-made cards in the Keysight chassis, in figure 33 (c) and (h), which gives two possible outputs:  $\omega_{RF1} = \omega_{LO} - \omega_{IF}$  and  $\omega_{RF2} = \omega_{LO} + \omega_{IF}$ . This process is known as *up conversion* [7], in figure 35. We can select one of these outputs thanks to single-sideband calibration [7].

In the same way, the signal coming out from the qubit circuit must be *down converted*, since it would be difficult for the electronic to read a GHz signal. As a matter of fact, the Keysight chassis is equipped with a Digitizer ADC (Analog to Digital Converter) with a sampling rate of 500 MSample/s, thus limiting the mea-

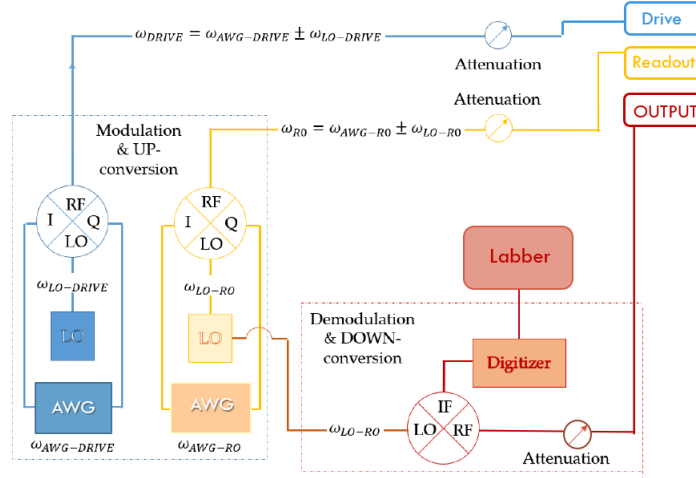


**Figure 35:** Schematics of the experimental setup for readout and drive pulsed measurements: in blue we have the up-conversion of the Drive signal, while in yellow the down-conversion of the Readout signal, both going to the cryostat lines; in red the Down-conversion of the output signal, which is measured with the digitizer and then is stored, manipulated and visualised with Labber [44]

surable frequency to  $500\text{ MHz}$  (figure 33 (i)). The output response of the DUT goes into a three-port mixer located in the home-made readout card in figure 33 (h), and is combined with the same LO of the readout input signal, used for the input signal *up conversion*. The output signal has the following frequency  $\omega_{IF}$ :

$$\omega_{IF} = |\omega_{out} - \omega_{LO}|, \quad (98)$$

which is in the range of  $500\text{ MHz}$ . The original form of the RO signal of the resonator is obtained by performing a Fast Fourier Transform of the down-converted signal. The results are stored and visualized through the Labber software [44].

### 4.3.3 Spectroscopy measurements

The characterization of transmon devices is fundamental for both the estimation of fundamental circuit parameters to be compared with the design specification, but also and most importantly to experimentally access to fundamental physical processes, such as decoherence effects hereby analyzed.

The most important parameters required in order to achieve this goal are: the readout resonator parameters, which determine the quality of the readout; the qubit parameters, including the qubit frequency, the fundamental energy scales  $E_J$  and  $E_C$ , and their tunability as a function of the flux.

In order to measure these experimental values, spectroscopy measurements are intensively used in literature [7]. Readout resonator spectroscopy uses single tone measurements. The input signal, generated by either the VNA port 1 (figure 34) in a continuous mode, or by the up-conversion card in a pulsed mode (figure 35) resonates with the readout resonators. The output signal is typically a Lorentzian whose dip corresponds to the resonance frequency. The amplitude of this resonance is linked to the resonator quality factor, discussed in sections 3.3 and 4.1, as:

$$Q = \frac{f_r}{\Delta f}, \quad (99)$$

where  $\Delta f$  is the Full Width at Half Maximum (FWHM) and  $f_r$  is the resonator frequency.

Single-tone spectroscopy also allows to measure the dispersive shift of the resonator given by the coupling with the qubit. If the power of the input signal is too large, the two-level system represented by the qubit is saturated. Therefore, the readout resonance frequency corresponds to the value in absence of the qubit, also known as bare state. If the power is sufficiently low, the resonator frequency will shift, recovering the dressed state and the dispersive shift (equation 57). As re-

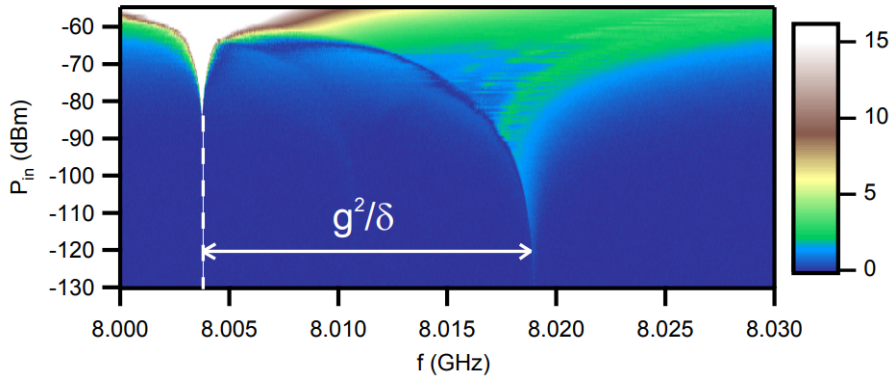


**Figure 36:** Cavity power spectroscopy [45]: colorplot of the amplitude of the readout signal as a function of the power and the frequency of the input signal. The dispersive shift depends on the coupling  $g$  and the detuning  $\delta$  [45].

ported in figure 36, the dispersive shift measurement allows obtaining information on the readout-qubit coupling strength  $g$ , once known the qubit-resonator detuning  $\Delta$ .

Single-tone spectroscopy of the readout resonator can also be performed as a function of an external flux field applied to the qubit. We change the flux in the loop by sending a DC current through the flux lines inductively coupled with the qubit on

chip. The current through the flux lines is generated by means of a voltage applied across the resistive input flux lines of the cryostat ( $R=50 \Omega$ ). The voltage offset is generated by dedicated AWG modules (figure 33 (e)). As reported in section 2.3, for a tunable transmon qubit, the transition frequency follows a cosinusoidal behaviour as a function of the flux. This also reflects in a cosinusoidal modulation of the readout resonator frequency in the dispersive regime, since the dispersive shift  $\chi$  is proportional to  $1/\omega_q(\Phi)$ . This measurement is fundamental in order to provide information on the split-transmon, like the SQUID asymmetry parameter  $d$ , and the relation between the flux voltage applied and a flux period  $\Phi_0$ , as we will discuss in chapter 5. Most importantly, it allows finding the flux sweet-spots, defined in sections 3.4 and 2.6, as the working points less sensitive to flux noise. For qubit spectroscopy measurements we send a *two-tone signal*, composed of an RF signal which is close to the frequency of the readout resonator in the dispersive regime, (readout tone), and an RF signal which sweeps in power and in frequency in order to excite the qubit (drive tone). The former is sent through the device feedline, and is used to excite and readout the qubit state, while the latter can be either sent through the feedline or dedicated qubit drive (QD) lines.

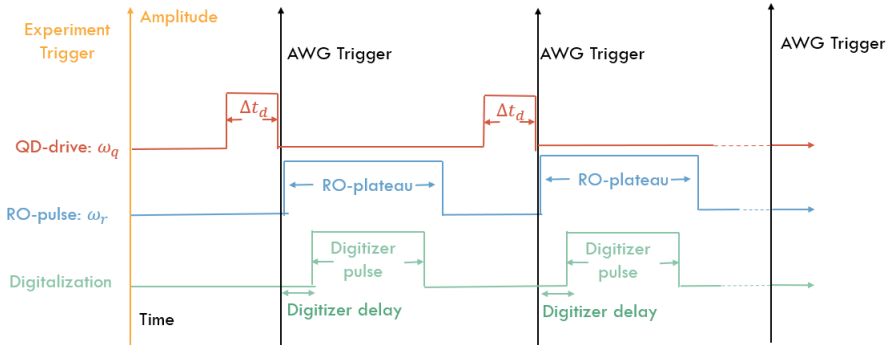


**Figure 37:** Trigger scheme for pulsed qubit spectroscopy measurements: the experiment trigger (in yellow), starts the experiment, the QD pulse (in red) is set to end at the AWG trigger (in black), the RO pulse (in blue) starts at the trigger, and the digitizer pulse (in green) starts after the trigger with a small delay.

Both the readout and drive tones are pulsed RF signals generated by up conversion. In order to perform the measurement, a trigger signal starts every experimental cycle. For each experiment period, we build a QD Gaussian pulse characterised by a finite plateau length  $\Delta t_d$ , and variable frequency, by combining into the IQ mixer two channels of the AWG cards, as described in section 4.3.2. We do the same for the square RO pulse, for which we set both the duration and the frequency. The AWGs are able to generate an internal trigger common with all their channels,

which we set to be delayed from the experiment trigger, as shown in figure 37. We then set the end of the QD pulse and the start of the RO pulse to be always aligned with the AWG trigger signal. In this way, no RO is performed without first having introduced a qubit drive pulse on the qubit. Finally, we digitize the output signal after down conversion (section 4.3.2), soon after the RO pulse. The acquisition process can be schematized as (figure 37):

- Trigger that starts the sequence;
- QD pulse starts with a delay;
- RO starts after QD pulse;
- The digitalization always occurs within a window inside the duration of the RO pulse.

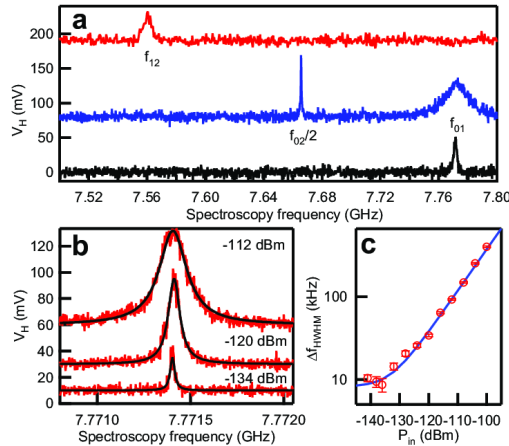


**Figure 38:** Qubit spectroscopy [45]:(a) qubit spectrum showing anharmonic energy levels where  $f_{12}$  is the transition frequency between the first excited state  $|1\rangle$  and second excited state  $|2\rangle$ ,  $f_{02}/2$  is the two-photon transition frequency between the ground state  $|0\rangle$  and  $|2\rangle$  and  $f_{01}$  is the transition between  $|0\rangle$  and  $|1\rangle$ . (b) The resonance peak of  $f_{01}$  as a function of the power. (c) Spectroscopic full width at half maximum linewidth versus driving power.

In two-tone spectroscopy measurements, we will measure a peak in the readout output signal when the frequency of the drive tone resonates with the transition frequency of the qubit. In fact, when  $\omega_d = \omega_q$ , the qubit goes from the ground state to the first excited state. On its way back, the qubit emits a photon, which is absorbed by the resonator, showing a maximum in the energy spectrum (figure 38 (a)). In addition, we observe that, by increasing the drive tone power the FWHM of

the transition frequency peak broadens, as shown in figure 38 (b) and (c), and additional peaks emerge. This is related to the possibility to excite higher order qubit transitions, which will occur at lower frequency, given the negative anharmonicity of the transmon. The separation between each peak in the qubit spectroscopy allows determining the charging energy  $E_c$ , as pointed out in equation 43.

As discussed for the resonator, we must study the qubit transition frequency's dependency with the flux by changing the flux inside the circuit. This allows giving another estimation of the flux sweet spot.

### 4.3.4 Time domain measurements

The experimental measurement of the transmon main circuit parameters by spectroscopy measurements is fundamental for the study of the decoherence in transmon qubits. However, in order to perform measurements on the relaxation and dephasing times, we need to move from the frequency domain to the time domain.

Typically, the first time domain measurement for a superconducting qubit is the

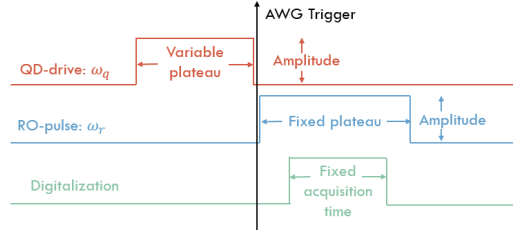


**Figure 39:** Rabi measurement protocol: we send a drive pulse of increasing duration, then we measure the qubit state by sending the readout and acquisition pulses. We note that the QD pulse ends at the AWG trigger, and the RO pulse starts at the AWG trigger.

measurements of Rabi oscillations, whose experimental protocol is reported in figure 39. Once the transition frequency of the qubit is found by means of the qubit spectroscopy, we send a pulse of variable duration in order to excite the qubit and induce coherent transitions between the ground and excited states, as predicted by the Rabi model [6]. It can be proven that a two-level system in the presence of an external perturbation, like the qubit drive signal, will oscillate between its states as a sinusoidal function of time [6]. We can represent the perturbation in terms of its amplitude  $A$  and frequency  $\omega_d$  and use the rotating frame representation introduced in section 2.7. In this way, the time dependent Schrödinger equation can be easily solved for the coefficients  $\alpha(t)$  and  $\beta(t)$  of the Bloch sphere representation. The probability for the ground state to be excited as a function of time is [6]:

$$P_e(t) = |C_e(t)|^2 = \frac{A^2}{\Omega_R^2 \hbar^2} \sin^2 \left( \frac{\Omega_R t}{2} \right), \quad (100)$$

where  $\Omega_R$  is the Rabi oscillation frequency. It depends on the amplitude of the perturbation signal and on the detuning  $\Delta = \omega_q - \omega_d$  between the qubit frequency and the drive frequency [7] as:

$$\Omega_R = \sqrt{\frac{A^2}{2} + \Delta^2}. \quad (101)$$

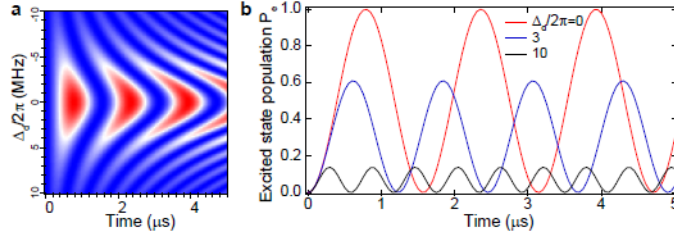


**Figure 40:** Rabi oscillations [7]: a) Rabi *Chevron* plot of the output signal as a function of the detuning between the qubit frequency and the drive frequency  $\Delta$  in units of  $2\pi$ , and the time duration of the drive pulse; b) Rabi oscillations with detuning  $\Delta = 0, 3$  and  $10$  in units of  $2\pi$ .

By increasing the detuning  $\Delta$ , the amplitude of the oscillation decreases and their frequency increases, according to equation 101. On resonance, the amplitude of the Rabi oscillations is maximum and the Rabi frequency is the smallest possible. An experimental outcome of this behavior is represented by the well-known *Chevron* plot, reported in figure 40 (a) (adapted from [7]), i.e. a colorplot of the Rabi oscillation as a function of both the frequency and the time duration of the Drive pulse. The centre of the *Chevron* plot identifies the drive frequency which resonates with the qubit (red curve in figure 40 (a), which reports Rabi oscillations for different values of the detuning  $\Delta$ ).

Another fundamental information given by Rabi oscillation measurement is the duration of the  $\pi$  pulse, which is the qubit drive plateau duration needed for the qubit to make a transition from the ground state to the first excited state [7]. From equation 101, we observe that the Rabi frequency grows with the amplitude  $A$  of the drive signal, thus the  $\pi$  pulse becomes shorter. For Quantum Gates implementation, we want a  $\pi$  pulse as short as possible, in order to have the largest number of gate implemented, but a pulse with large power can induce higher-order transitions, as depicted in figure 5.1.2 (b). Because of this, we have to find a compromise between the time duration of the  $\pi$  pulse and the optimal amplitude of the qubit drive signal [7].

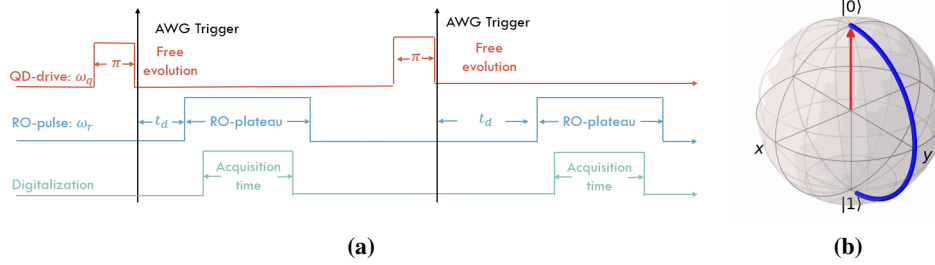


**Figure 41:** a)  $T_1$  measurement protocol: we send a  $\pi$  pulse to the qubit, which is set to end at the AWG trigger, then we wait (free evolution) for an increasing amount of time before the readout pulse, and the acquisition pulse, which is as usual inside the RO pulse. The readout pulse is set to start at a variable delay  $t_d$  from the AWG trigger. b) Qubit simulation of the  $T_1$  protocol measurement, the qubit starts in the ground state  $|0\rangle$ , then it is excited to  $|1\rangle$  with the  $\pi$  pulse.

Once the duration of the  $\pi$  pulse and the transition frequency are set, it is possible to perform decoherence measurements. The relaxation time  $T_1$  can be measured by sending a  $\pi$  pulse to excite the qubit and then waiting for it to return to the ground state, as shown in figure 41 (a). In figure 41 (b), we can observe an example of the  $T_1$  measurement protocol on the qubit, visualized on the Bloch sphere. This simulation is realized with the Python package Qutip [46].

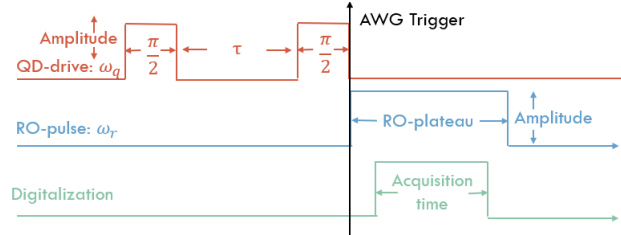


**Figure 42:** Ramsey measurement protocol: we send a  $\pi/2$  pulse, and we wait for the system to freely evolve for a time  $\tau$ . Then we send another  $\pi/2$  pulse that ends at the AWG trigger. We finally measure the qubit state by sending the readout pulse and the acquisition pulse.

For what concerns the study of dephasing processes in a transmon qubit, the most widely used experiment is based on the Ramsey interferometry, which is based on the following protocol (figure 42): we first prepare the qubit on the Bloch sphere equator, by sending a  $\frac{\pi}{2}$  pulse, i.e. a qubit drive signal with half the amplitude of a  $\pi$  pulse. Then, after waiting for a variable time (free evolution), we send another  $\frac{\pi}{2}$  pulse and finally measure the qubit state, as shown in figure 42. Since we let the qubit freely evolve in the equatorial plane, this measurement allows us to give a first estimation of the dephasing time of the qubit.

Ramsey interferometry is highly sensitive to the drive-qubit frequencies detuning

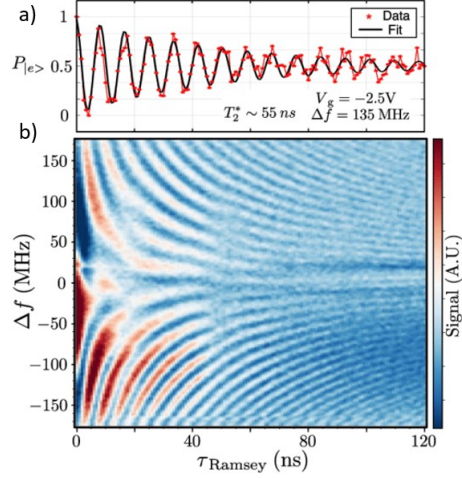


**Figure 43:** In a) Ramsey oscillation at  $\delta\omega = 135 \text{ MHz}$ . In b) Ramsey fringes colorplot of the free evolution time  $\tau_{\text{Ramsey}}$  and the detuning  $\Delta f$  [34].

$\delta\omega = \omega_q - \omega_d$ . In fact, from the Bloch-Redfield model, discussed in section 3.1, we know that the off-diagonal density matrix element depends on  $\delta\omega$  as [7]:

$$\rho_{10} = \alpha\beta^* e^{i\delta\omega t} e^{-\Gamma_2 t}. \quad (102)$$

Therefore, for delta  $\delta\omega \neq 0$ , Ramsey interferometry will give as a result a damped cosinusoidal free evolution, as shown in figure 43 (a), while for  $\delta\omega = 0$ , Ramsey oscillations become a pure exponential. An example of a typical Ramsey interferometry on superconducting qubit as a function of the free evolution time ( $\tau_{\text{Ramsey}}$ ) and the qubit drive frequency detuning  $\Delta f = \delta\omega$ , provides the famous Ramsey fringes, as reported in figure 43 (b). Data are adapted from [34].

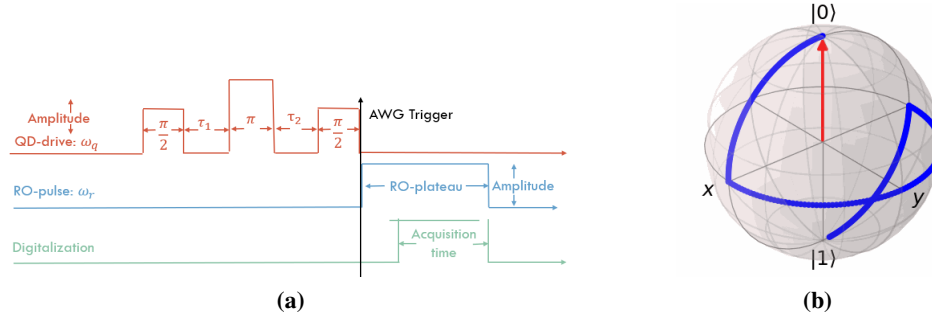


**Figure 44:** a)  $T_2$  Hahn-echo protocol: we send a  $\frac{\pi}{2}$  pulse, then let the qubit freely evolve for a time  $\tau_1$ . We send a  $\pi$  pulse to move the qubit on the equatorial plane, then wait for a time  $\tau_2$  for it to refocus. We finally send another  $\frac{\pi}{2}$  pulse that ends with the AWG trigger, when the Readout pulse starts, followed by the acquisition pulse. b) Qutip simulation for  $T_2$  Hahn-echo protocol: the qubit is prepared on the ground state identifies by the red arrow, then it is driven to the equatorial plane with a  $\pi/2$  rotation around the y-axis. After waiting a time  $\tau_2$ , it is refocused with a  $\pi$  pulse around the x-axis, and finally a rotation of  $\pi/2$  around the y-axis drives the qubit to the excited state. Then, RO and acquisition take place.

Finally, the coherence time  $T_2$  is measured by performing a spin echo measurement. In this protocol, we send a  $\frac{\pi}{2}$  pulse, so the qubit can freely evolve on the equatorial plane, then we send a  $\pi$  pulse for the qubit to refocus it on the equatorial plane, and finally another  $\frac{\pi}{2}$  pulse. This protocol is known as Hahn-echo  $T_2$  measurement, and it is reported in figure 44 (a). The introduction of the intermediate  $\pi$  pulse in the middle of a protocol similar to Ramsey interferometry, in fact, allows reducing the effect of dephasing and thus approach the theoretical limit in absence of dephasing, i.e.  $T_2 \simeq 2T_1$  [11], [7]. In figure 44 (b), we can observe an example of the Hahn Echo protocol visualized on the Bloch sphere. Qubit dynamics simulations are performed with the Python Qutip package [46].

## 5 Measurements and data analysis

In this chapter, we will report on our experimental outcomes, with a particular focus on noise and decoherence. The aim of this data analysis is to identify the main noise source of relaxation and dephasing. We used the Python library *scqubits* [12] for an estimate of the different decay times, based on the measured values for flux bias, charge offset,  $E_J$  and  $E_c$ . Then, we compared these results with the measured  $T_1$  and  $T_2$ . We will focus on qubits 2 and 4 of the chip, because they showed a very different behaviour for what concerns noise and decoherence.

First, we will report the spectroscopy measurements (section 5.1) in order to characterize the readout resonators (section 5.1.1) and the qubits (section 5.1.2). Then, in section 5.2, we will perform time domain measurements in order to evaluate and analyze the coherence times. Finally, we will observe how the coupling between these two qubits can affect their coherence properties (section 5.3).

### 5.1 Spectroscopy measurements

#### 5.1.1 Readout resonator spectroscopy

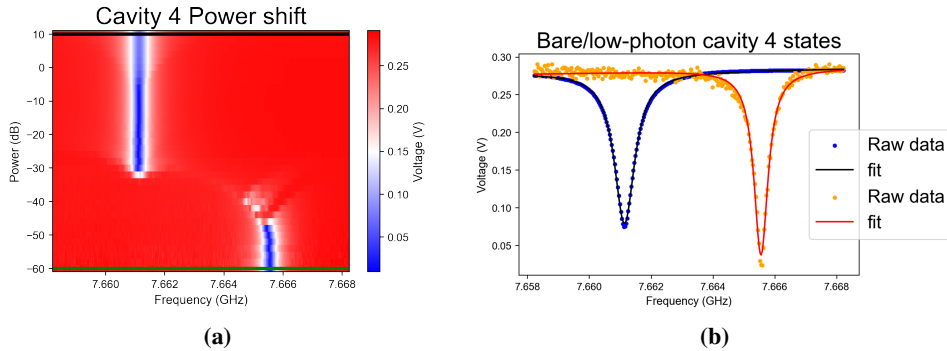


**Figure 45:** Power shift of cavity 4 coupled to qubit 2: a) colorplot of the transmission parameter  $S_{21}$  as a function of the frequency, on the x-axis, and the attenuation, on the y-axis, of the input signal; the color scale identifies the voltage magnitude in V, the black line identifies the bare state at power 10 dB, and the green line the low photon regime at -60 dB; in b), the straight line curves (in black and red) correspond to the fits of the bare resonance frequency at 10 dB (blue) and shifted resonance frequency at -60 dB (orange), respectively.

As discussed in the previous section, we first measure the power shift of the cavities. Cavity 4 is coupled to qubit 2, while cavity 6 to qubit 4, as shown in section 4.1. In figure 45 (a), we can observe the colorplot of cavity 4 power shift. The response of the resonator clearly indicates adsorption of photons, as shown in fig-

ure 28, in which a dip corresponding to the resonance frequency of the resonator arises. If the power is low enough, i.e. we are in the single photon regime, the readout frequency shifts, as pointed out in figure 45 (b). The same occurs for cavity 6 in figure 46.

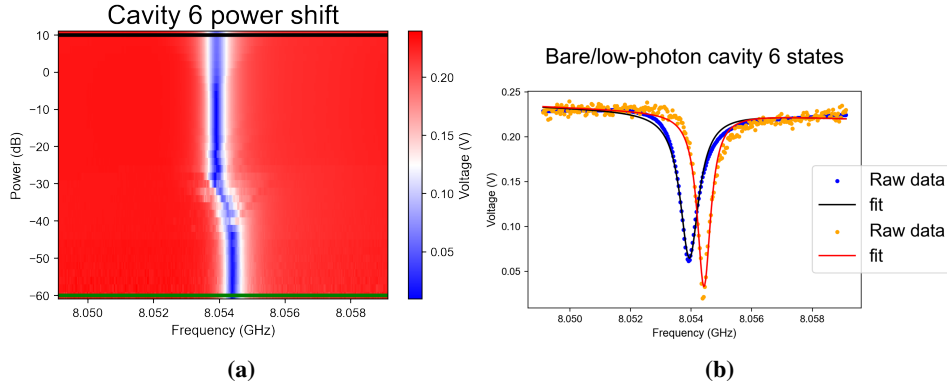


**Figure 46:** Power shift of cavity 6 coupled to qubit 4: a) on the x-axis we have the frequency of the input signal, and on the y-axis its attenuation, the color scale shows the voltage magnitude of the output signal in V, the black line identifies the bare state at power 10 dB, and the green line the low photon regime at -60 dB ; b) bare resonance frequency at 10 dB (blue) fitted with *resonator tools* [47] (the straight line in black) and shifted resonance frequency at -60 dB (orange), and its fit (the red straight line).

By performing a Lorentzian fit of the readout resonances with the Python library *resonator tools* [47], we evaluated the resonance frequency of the cavities and their quality factors, defined in equation 79. For cavity 4, we measured a bare frequency of  $\omega_r = 7.66113 \pm 0.00003 \text{ GHz}$ , with maximum error, given by the minimum step points acquisition of the VNA, and a shift of:  $\chi = 3.29 \pm 0.06 \text{ MHz}$ . The quality factors are:  $Q_l \simeq 10^4$ ,  $Q_i \simeq 10^5$  and  $Q_c \simeq 10^4$ . While, for cavity 6, the resonance frequency is  $\omega_r = 8.05394 \pm 0.00003 \text{ GHz}$ , and the dispersive shift  $\chi = 0.48 \pm 0.06 \text{ MHz}$ . The computed quality factors are:  $Q_l \simeq 10^4$ ,  $Q_i \simeq 10^5$  and  $Q_c \simeq 10^4$ .

Another important measurement to perform on cavities is flux spectroscopy, as described in section 4.3.3. Since the resonator is coupled to the qubit, its frequency will modulate with the external flux bias (section 2.6). By taking into account the dispersive shift in equation 57, and the expression of  $E_J$  for a split-transmon

(equation 95), we obtain:

$$\begin{aligned}\omega_{r,dressed} &= \omega_{r,bare} + \frac{g^2}{\Delta} = \\ &= \omega_{r,bare} + \frac{g^2}{|\sqrt{8E_C E_J} \cos \frac{\pi\Phi}{\Phi_0}| \sqrt{1 + d^2 \tan^2 \left( \frac{\pi\Phi}{\Phi_0} \right)} - \omega_{r,bare}}.\end{aligned}\quad (103)$$

In our measurements, we have assumed the transmon qubits to be symmetric, i.e.  $d=0$ . By using the Python library *lmfit* [48], based on the least square method, we performed a fit of the resonator frequency as a function of the flux, as shown in figure 47 (a). We used a fitting function of the type  $(a + b \sin(x))$ , according to equation 103. We obtained that the period of the oscillations, which corresponds to the flux required to introduce in the DC-SQUID two flux quanta  $\Phi_0$ , is  $3.22 \pm 0.06$  V, and the voltage at the flux sweet spot is  $\Phi_{sweetspot} = -0.15 \pm 0.01$  V.

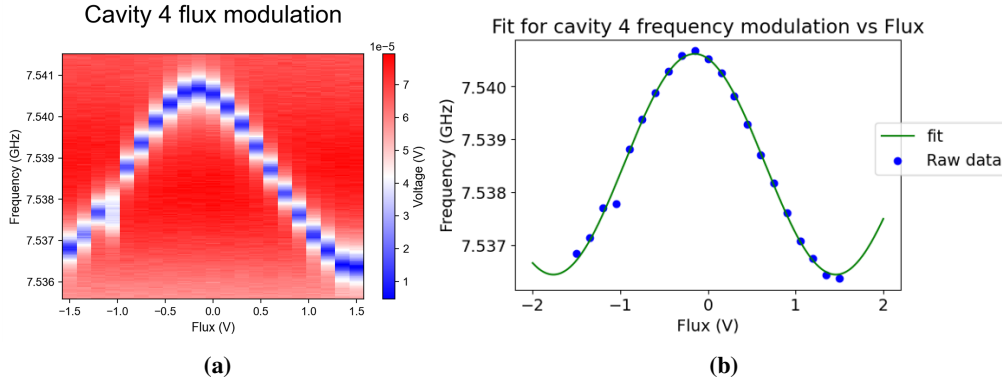


**Figure 47:** Cavity 4 coupled to qubit 2 flux spectroscopy: a) colorplot of the modulation of the transmitted signal as a function of the flux bias, on the x-axis, and the readout frequency, on the y-axis, the color scale identifies the voltage magnitude in V; b) sinusoidal fit (in green) of the readout frequency (in blue) extrapolated from (a) as a function of the flux.

The same procedure has been followed for the readout cavity of qubit 4, cavity 6, as shown in figure 48.

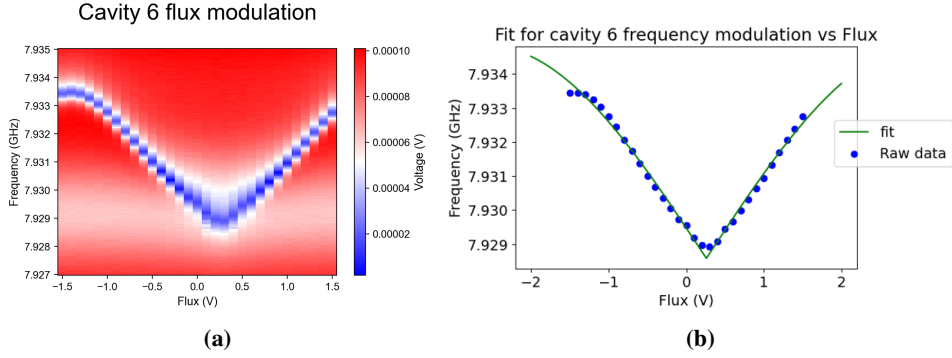


**Figure 48:** Cavity 6 coupled to qubit 4 flux spectroscopy: a) colorplot of the modulation of the transmitted signal as a function of the flux bias, on the x-axis, and the readout frequency, on the y-axis, the color scale identifies the voltage magnitude in V; b) sinusoidal fit (in green) of the readout frequency (in blue) extrapolated from (a) as a function of the flux.

We obtained that the period of the oscillation is  $5.7 \pm 0.6 V$ , and the flux sweet spot is at  $\Phi_{sweetspot} = -2.50 \pm 0.3 V$ . For both the readout cavity flux spectroscopy measurements, the errors are statistical.

In table 3, we report all the relevant quantities measured for the readout resonators with their errors. The measured values are consistent with the ones predicted by design (table 2).

Cavity spectroscopy analysis		
Quantity	Cavity 4	Cavity 6
Bare frequency (GHz)	$7.66113 \pm 0.00003$	$8.05394 \pm 0.00003$
$Q_l$	$10^4$	$10^4$
$Q_i$	$10^5$	$10^5$
$Q_c$	$10^4$	$10^4$
Shift (MHz)	$3.29 \pm 0.06$	$0.48 \pm 0.06$

**Table 3:** Cavity spectroscopy measurements: we here report the main quantities evaluated for cavities 4 and 6, the resonance frequencies, the quality factors and the dispersive shift.

## 5.1.2 Qubit spectroscopy

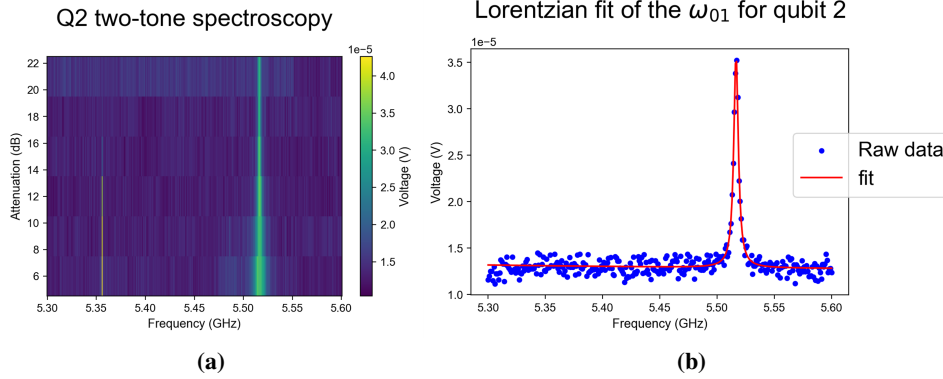


**Figure 49:** a) Qubit 2 power spectroscopy colorplot: output signal as a function of the qubit drive frequency, on the x-axis and power, on the y-axis, the color scale shows the voltage magnitude in V. b) fit (in red) for  $\omega_{01}$  transition, based on a Lorentzian function, of the voltage magnitude (in blue), measured at attenuation 10 dB, as a function of the QD frequency.

We performed a power spectroscopy on qubit 2 (figure 49 (a)) and qubit 4 (figure 50 (a)), by two-tone spectroscopy described in section 4.3.4, in order to determine the qubits transition frequencies. From these data, we can evaluate the resonance frequency  $\omega_{01}$  by performing a Lorentzian fit with the Python library *lmfit* [48], and using the function  $((\Gamma/(\Gamma^2 + (x - x_0)^2)))$ . Here,  $\Gamma$  is the resonance FWHM, and  $x_0$  is the resonance frequency. The fit of  $\omega_{01}$  at qubit drive (QD) attenuation 12 dB is reported in figure 49 (b). We obtained a resonance frequency of  $5.516 \pm 0.001$  GHz, with maximum error.

In the same way, we evaluated the resonance frequency of qubit 4, thanks to a Lorentzian fit shown in figure 50 (b), finding a resonance frequency of  $6.090 \pm 0.001$  GHz.

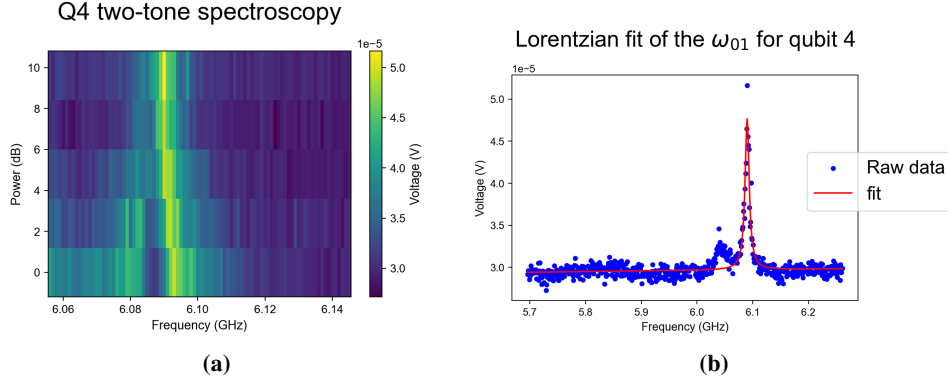


**Figure 50:** a) Qubit 4 power spectroscopy colorplot: output signal as a function of the qubit drive frequency, on the x-axis and power, on the y-axis. b) fit (in red) for qubit 4 resonance frequency, based on a Lorentzian function, of the voltage magnitude (in blue), measured at attenuation 10 dB, as a function of the QD frequency.

We observe that, since dephasing is related to the broadening of the transition frequency, from the amplitude of these resonances we can evaluate  $T_{\phi}^* = 2Q_r/\omega_r$ . We obtained  $T_{\phi}^* = 443 \pm 16 \text{ ns}$  for qubit 2 and  $T_{\phi}^* = 420 \pm 30 \text{ ns}$  for qubit 4, with statistical errors. In section 5.2.3 and 5.2.4, we will see that dephasing time measured through Ramsey and Hahn-echo measurements are much larger than the values here reported. We must stress that two-tone spectroscopy implies qubit drive pulses with an average length of the order of 10 to 50  $\mu\text{s}$ , i.e. comparable with typical relaxation time in transmon circuits, while for typical Ramsey and Hahn-echo sequences the drive pulses have typical length of few nanoseconds. Therefore, during this measurement, the qubit coherence may be particularly affected by the driving electromagnetic field. Moreover, the QD frequency is slightly different, a few MHz, from the optimal one measured through Rabi *Chevron* plot and Ramsey fringes, thus inducing dephasing.

In case of qubit 2, as we can see from figure 49 (a), we identified both the transition from the ground state to the first excited ( $\omega_{01}$ , the thicker line in the right) and the two photons transition from the ground state to excited to the second excited energy level ( $\omega_{02}/2$ , the thinner one on the left). If we take into account the expression of the anharmonicity discussed in section 2.7, we can compute it by using the measured  $\omega_{02}$  and  $\omega_{01}$  as  $\alpha = 2(\omega_{01} - \omega_{02}/2) = 322 \pm 4 \text{ MHz}$ , where the error is maximum. By design, the anharmonicity should be the same for every qubit, so we can use this result as a reference for qubit 4.

We now report the flux spectroscopy for qubit 2, following the protocol discussed in section 4.3.4. Having extracted the frequency of the peaks as a function of the flux bias, we can evaluate the flux sweet spot by fitting with equation 103 the qubit

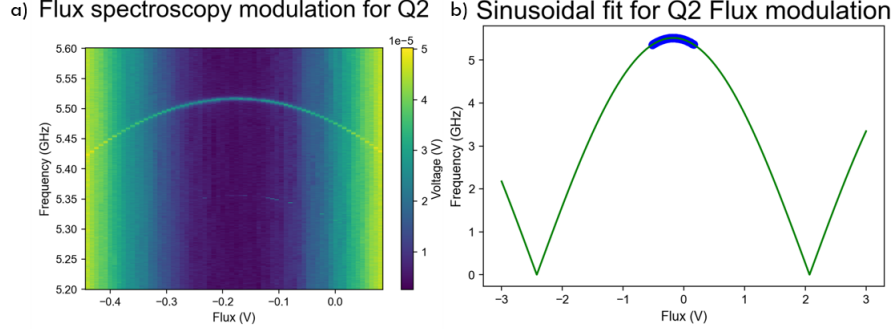


**Figure 51:** Qubit 2 flux spectroscopy: a) colorplot of the output signal as a function of the flux bias and the drive frequency, b) sinusoidal fit performed by using equation 103, of the qubit transition frequency as a function of the flux bias.

transition frequency  $\omega_{01}$  as a function of the flux bias (figure 63 (b)). We obtained the following results for qubit 2: the period of the oscillation is  $4.492 \pm 0.003 V$ , and the voltage at the flux sweet spot is  $\Phi_{sweetspot} = -0.1759 \pm 0.0002 V$ . These results are consistent with the ones obtained for cavity 4, reported in section 5.1.1. We repeated the same analysis for qubit 4, and found an oscillation period of  $5.67 \pm 0.01 V$  and a voltage at the flux sweet spot of  $-1.8 \pm 0.1 V$ . Here, the errors are statistical. This shows that the cavities are correctly coupled to the qubits, and that the qubit frequency modulates as predicted by theory.

We now report in table 4 all the relevant quantities measured in this section, which will be useful to understand the behaviour of the qubit and its coherence properties. From the resonance frequencies of the qubit and the readout resonator, we can evaluate the detuning  $\Delta$ , and thus the coupling  $g$ , which are consistent with the values expected by design. By knowing the transition frequency  $\omega_{01}$  and the anharmonicity  $\alpha$ , we are able to measure the charge energy  $E_C$  and the Josephson energy  $E_J$  (equations 33 and 43). From table 4, we note that their ratio is  $\simeq 50$ , showing that we are in the transmon regime (figure 12 (d)).

Qubit Spectroscopy analysis					
<i>qubit</i>	$\omega_{01}$ (GHz)	$E_J$ (GHz)	$E_C$ (GHz)	$\Delta$ (GHz)	$g$ (MHz)
2	$5.516 \pm 0.001$	$13.2 \pm 0.1$	$0.322 \pm 0.004$	$2.145 \pm 0.001$	$97 \pm 1$
4	$6.090 \pm 0.001$	$15.9 \pm 0.2$	$0.322 \pm 0.004$	$1.964 \pm 0.001$	$30 \pm 2$

**Table 4:** Qubit spectroscopy results: we here report the transition frequencies of qubit 2 and 4, their energies  $E_C$  and  $E_J$ , evaluated from equation 33, the detuning  $\Delta = \omega_r - \omega_{01}$  and the coupling  $\chi = g^2/\Delta$  evaluated from the cavities transition frequencies and their dispersive shift  $\chi$  in table 3.

## 5.2 Time evolution measurements

In this step of the qubits characterization, we aim at studying the evolution over time of qubits analyzed in this work, and measuring coherence times by performing the protocols described in section 4.3.4.

### 5.2.1 Rabi oscillations

In order to perform measurements of the coherence times, we must be able to excite the qubit by finding the duration of the  $\pi$  pulse. As discussed in section 4.3.4, the Rabi protocol makes the qubit oscillates between the ground and excited states as a function of the frequency  $\omega_d$  and the amplitude  $A$  of the drive (equation 100). As an example, we show the Rabi oscillations as a function of the frequency of the drive signal (*Chevron* plot) for qubit 4 in figure 52. As the drive frequency is on-resonance with the qubit frequency, the oscillation period decreases, while the oscillation amplitude is maximum. The centre of the *Chevron* plot, in fact, identifies the drive frequency resonant with the qubit, i.e.  $5.962 \pm 0.002$  GHz, with maximum error, which is consistent with the one measured through spectroscopy in section 5.1.2.

Rabi Chevron plot for Q4

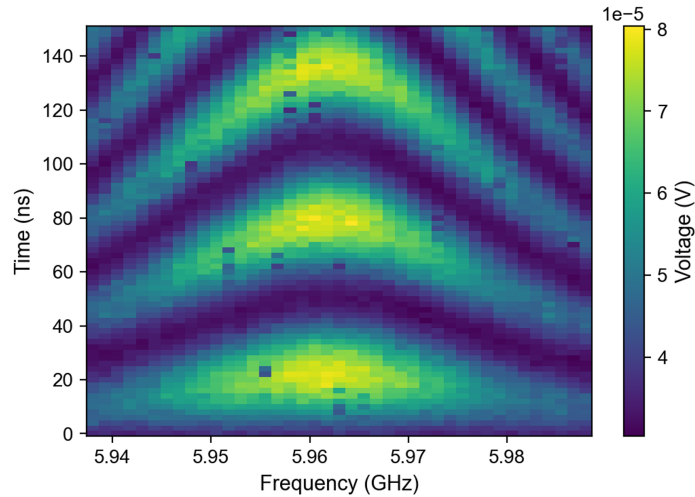


**Figure 52:** Qubit 4 Rabi *Chevron* plot: colormap of the voltage magnitude as a function of the QD pulse time duration (y-axis), and the QD frequency (x-axis).

On resonance with the qubit frequency, we performed a Rabi protocol at differ-

ent amplitudes of the QD power. As discussed in section 4.3.4, we expect that the period of the oscillation reduces when the qubit drive amplitude is increased (figure 53 (a)). We can estimate the duration of the oscillation semi-period, the  $\pi$  pulse by fitting the Rabi oscillation with the function  $(c + (a/b)^2(\sin(b \times x + d))^2)$ . The result is shown in figure 53 (b), where we found  $\pi_{pulse} = 17 \pm 1 ns$ , where the error is maximum, given by the resolution of the AWG.

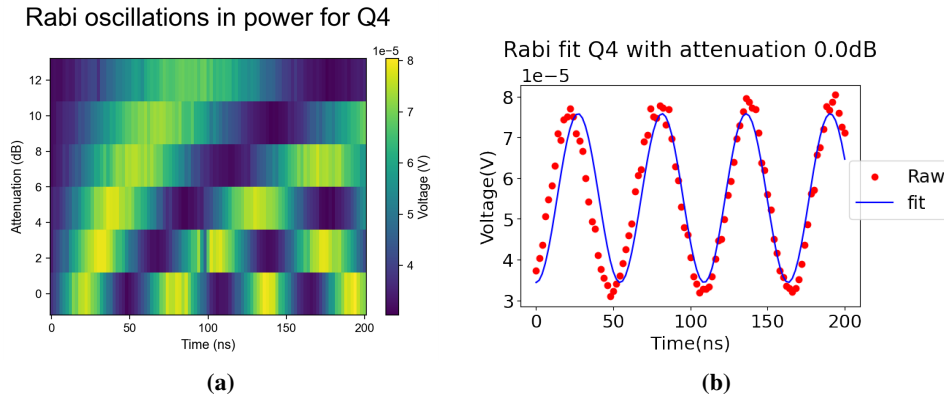


**Figure 53:** Qubit 4 Rabi oscillation in power: a) colorplot of the output signal as a function of the drive pulse attenuation in dB, on the y-axis, and the drive pulse time, on the x-axis; b) sinusoidal fit for Rabi oscillation at attenuation 0.0 dB.

We repeated the same measurements for qubit 2, first observing the *Chevron* plot in order to set the transition frequency, then evaluating the optimal  $\pi$  pulse duration by changing the drive pulse power. We found a transition frequency of  $5.517 \pm 0.001 GHz$ , and a semi-period of  $\pi_{pulse} = 25 \pm 1 ns$ , with maximum error, as shown in figure 54.

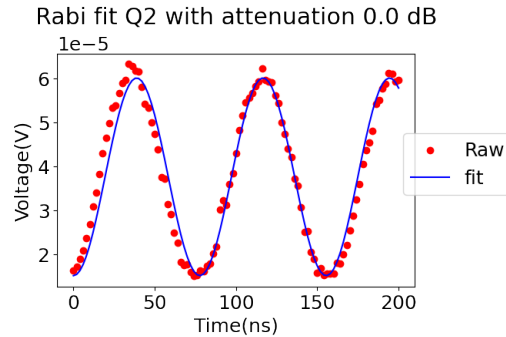


**Figure 54:** Qubit 2 Rabi oscillation frequency estimation: we performed a sinusoidal fit (in blue), with *lmfit* [48], of the Rabi oscillations (in red) at QD attenuation 0.0 dB.

### 5.2.2 Relaxation time

We now report the measurements of  $T_1$  for qubit 2 and qubit 4, by using the protocol described in section 4.3.4. We sent a  $\pi$  pulse to the qubit in order to excite the qubit, and then we let it freely evolve. In order to understand which noise source is more relevant, we compared our experimental results with the simulations performed by *scqubits* [12], described in section 3.1. Thanks to this library, we can simulate the transmon relaxation times by setting the parameters  $E_J$ ,  $E_C$  and  $d$  previously evaluated (table 4). We also must set the flux bias in units of the flux quantum, measured in sections 5.1.2, and 5.1.1. In figure 55 we show the exponential decay as a function of time for qubit 2. The decay time of this evolution will give an estimation of  $T_1$ .

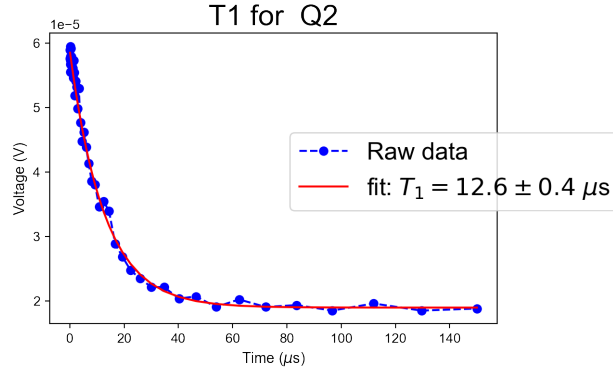


**Figure 55:**  $T_1$  exponential decay fit performed by *lmfit* [48] for Qubit 2: we evaluated the relaxation time with an exponential fit (in red) on the raw data (in blue).

We found a relaxation time  $T_1 = 12.6 \pm 0.4 \mu s$ , where the error is statistical. In order to evaluate the consistency of these experimental results, we evaluated the relaxation times caused by the main noise sources described in section 3.3. Since the chip is at cryogenic temperatures, i.e. 10 mK quasiparticle noise can be neglected (section 3.3). As discussed in section 3.3, two of the intrinsic relaxation channels for a transmon qubit are the spontaneous emission and the Purcell effect. From the qubit transition frequency, we can evaluate the resulting relaxation times  $T_1^{rad}$  and  $T_1^{Purcell}$ , by using equations 78 and 81, respectively, as discussed in section 3.3. By assuming the distance between the superconducting islands to be  $L \simeq 15 \mu m$  [11], and using the measured transition frequency measured in section 5.1.2, we obtained  $T_1^{rad} \simeq 4 ms$  for qubit 2. Since the total relaxation time measured for qubit 2 is of the order of  $10 \mu s$ , spontaneous emission is unlikely to be the main relaxation source.

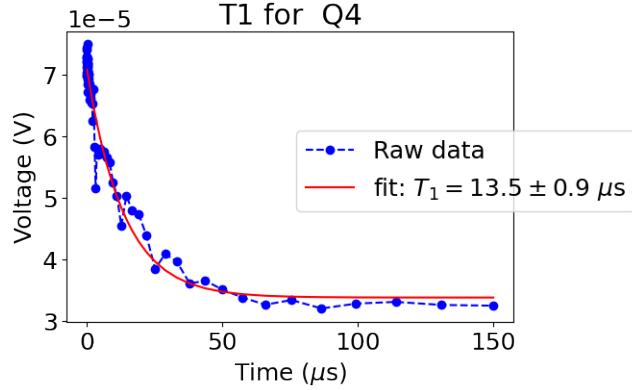


**Figure 56:** Exponential fit (in red) of the  $T_1$  protocol decay raw data (in blue) for Qubit 4.

For what concerns the Purcell decay time, within the readout parameters inspected in section 5.1.1 and 5.1.2, we obtain  $T_{Purcell} \simeq 100 \mu s$  for qubit 2. These results are consistent with the ones reported in literature [11]. Since these decay times are larger than the measured relaxation time of a transmon qubit of tens of  $\mu s$ , we can assume that spontaneous emission and Purcell effect do not determine the qubit coherence properties.

We now report the theoretical predictions for qubit 2 of the relaxation times due to flux bias noise and dielectric losses noise, computed by *scqubits* [12], based on equations 87 and 84 (section 3.3). For flux bias noise, we obtained a very large relaxation time of  $\simeq \infty$ , meaning that we exceeded the maximum value computed by the simulator, by using the standard values [11] of  $M = 400$ ,  $Z = 50$  [11].

For dielectric losses noise, we found a relaxation time that spans from  $10 \mu s$  to  $30 \mu s$ , based on equation 84, using a dielectric quality factor  $Q_{cap}$  that goes from  $10^5$  to  $10^6$ . [11]. This simulation suggests that the total relaxation time previously measured is dominated by the decay rate due to dielectric losses.

We repeated the same measurement for qubit 4, as shown in figure 56, and found a relaxation time of  $T_1 = 13.5 \pm 0.9 \mu s$ , where the errors are statistical.

The evaluated spontaneous emission time decay for qubit 4, is  $T_1^{rad} \simeq 3 ms$ , which is far larger than the measured  $T_1$ , proving that this decay channel can be neglected. From the cavity quality factor (section 5.1.1) and the qubit transition frequency (section 5.1.2), we measured the Purcell relaxation time for qubit 4 of  $T_{Purcell} \simeq 1 ms$ . This shows that Purcell noise does not significantly contribute to  $T_1$ . By making a *scqubits* [12] simulation of the other relaxation times, we found that the flux coupling noise is  $\simeq \infty$ . While, the decay time due to dielectric losses is  $\simeq 10 - 30 \mu s$ , for  $Q_{cap} = 10^5 - 10^6$ , showing that, also in this case, this is the

main source of energy relaxation.

<b>Relaxation times</b>		
$T_1$ measured( $\mu s$ )	$T_{1,Q_2} = 12.6 \pm 0.4$	$T_{1,Q_4} = 13.5 \pm 0.9$
<i>Relaxation channel</i>	$T_1$ for qubit 2 ( $\mu s$ )	$T_1$ for qubit 4 ( $\mu s$ )
Spontaneous emission	4000	3000
Purcell effect	100	1000
Dielectric losses	10 – 30	10 – 30
Flux bias	$\infty$	$\infty$

**Table 5:** Relaxation channel analysis for qubit 2 and 4: we here report the decay times evaluated by using the model discussed in section 3.3.

### 5.2.3 Ramsey interferometry

As discussed in section 4.3.4, Ramsey interferometry measurement allows evaluating the coherence time of the qubit,  $T_2^*$ , and the qubit transition frequency. We performed the Ramsey protocol for qubit 2, described in section 4.3.4, while changing the frequency of the qubit drive pulse. Thus, we observe the Ramsey fringes in figure 57. In order to give another estimation of the qubit frequency, we draw a line at the middle of the modulation and found that the transition frequency for qubit 2, according to Ramsey interferometry, is approximately  $\omega_{Q_2} = 5.51645 \pm 0.00003 \text{ GHz}$ , with maximum error, which is consistent with the one measured by means of the spectroscopy (section 5.1.2) and the Rabi protocol (section 5.2.1).

## Ramsey fringes for Q2

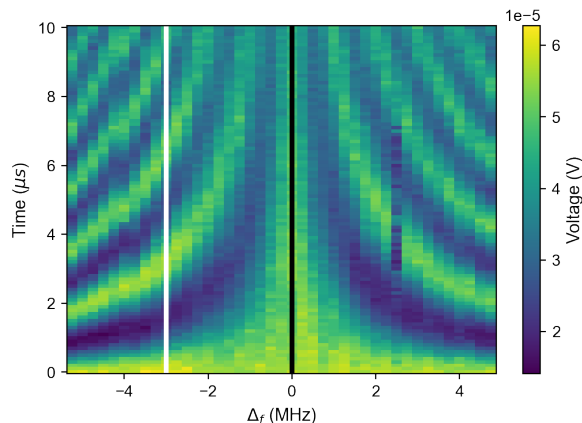


**Figure 57:** Qubit 2 Ramsey fringes: colormap of the voltage magnitude, in the color scale, as a function of the QD frequency (x-axis), and the QD plateau duration (y-axis). The black line identifies the resonance frequency of the qubit, while the white line corresponds to a detuning of  $2.99 \pm 0.01$  MHz.

We performed a fit on the Ramsey decay to evaluate  $T_2^*$ . Since we want to observe dephasing, we choose two measurements, one done off-resonance and one done on-resonance. We expect the dephasing time on-resonance to be a pure exponential, as pointed out in section 4.3.4. So, we used *lmfit* [48] to perform an exponential fit (figure 58) with a trivial function of the type  $(a + b \times e^{-(x/c)})$ , obtaining  $T_{2,on}^* = 12 \pm 3$   $\mu s$ . Ramsey's oscillation off-resonance can be fitted by a function of the type  $(\sin x \times e^{-x^2})$ , as shown in figure 58. By fitting a Ramsey oscillation with detuning  $\delta\omega = 2.99 \pm 0.001$  MHz, we obtained a dephasing time of  $T_{2,off}^* = 8.4 \pm 0.4$   $\mu s$ . Here, all the errors are statistical. As one can notice, pushing the drive signal off-resonance with the qubit frequency introduces dephasing effects, which results in a decrease of  $T_2^*$ . This is consistent with the lower  $T_2^*$  obtained from qubit spectroscopy fit in section 5.1.2, in which the drive-qubit detuning was of the order of 5 MHz.

We repeated the same procedure for qubit 4. By performing an off-resonance Ramsey measurement for qubit 4, with a detuning of  $\delta\omega = 0.574 \pm 0.001$  MHz, and fitting this oscillation with *lmfit*, we obtained a dephasing time of  $T_{2,off}^* = 6.0 \pm 0.4$   $\mu s$ , where the errors are statistical.

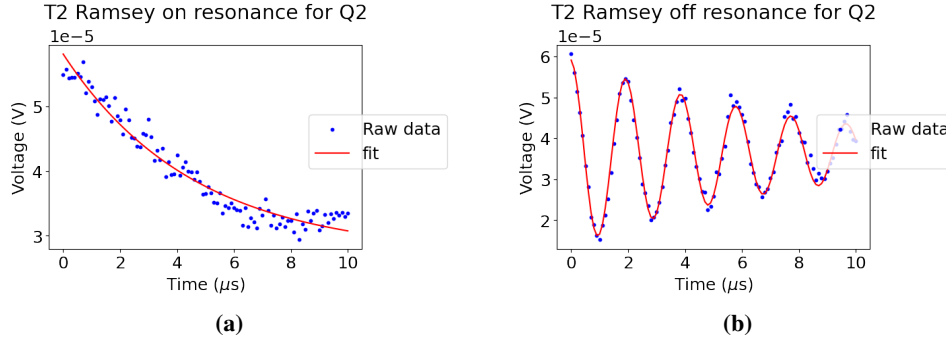


**Figure 58:** Fitting of the Ramsey oscillations for qubit 2 on resonance (a) and off resonance (b). In blue, we have the raw data, while in red the fitting.

### 5.2.4 Hahn Echo

Finally, we studied the coherence time of qubit 2 and 4 with Hahn-Echo measurement, as described in section 4.3.4.

Following the protocol in figure 44 (a), we measured the longitudinal relaxation for qubit 2. Having set the flux at approximately the flux sweet spot for qubit 2, measured in section 5.1, the dephasing time due to flux noise should be large enough to have, according to equation 66,  $T_2 \simeq 2 T_1$ .

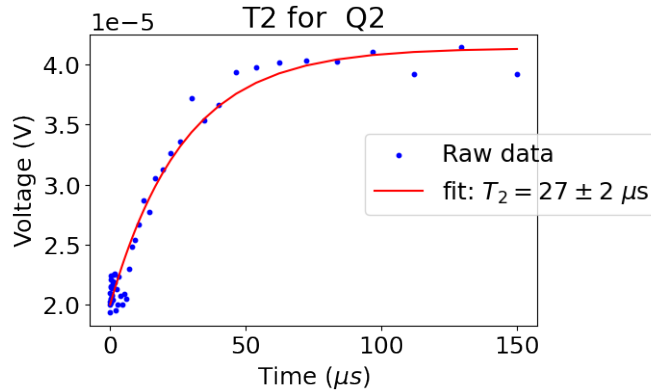


**Figure 59:** Hahn Echo measurement for qubit 2: exponential fit (in red), of the voltage magnitude (in blue) as a function of time for qubit 2.

We fit the Hahn-Echo decay with a pure exponential, as shown in figure 59, thus providing an estimation of  $T_2 = 26 \pm 2 \mu s$ , where the error is statistical. This is consistent with the ideal value  $T_2 \simeq 2 T_1$ , proving that dephasing is suppressed.

In order to evaluate the consistency of this measurement, we computed the dephasing times for qubit 2 with *scqubits* [12]. In this case, we set the flux in the SQUID at  $\Phi/\Phi_0 = 0.003 \pm 0.001$  from the sweet spot, which is the flux used in our measurements. We found the following dephasing times for the main dephasing channels, described in section 3.4: for flux noise  $T_{\phi,flux} \simeq 330 \mu s$ , while for critical current noise  $T_{\phi,critical\ current} \simeq 1600 \mu s$ . For this evaluation, we used the standard values of the noise amplitude [11] and the values of  $E_J$ ,  $E_C$  and  $d$  measured in section 5.1.2. These results confirm that the dephasing times are sufficiently large to not contribute to  $T_2$ . By making a simulation of  $T_2$  as a function of flux (figure 60), we observe that the predicted coherence time, for the flux bias set in our measurements, is consistent with the experimental one.

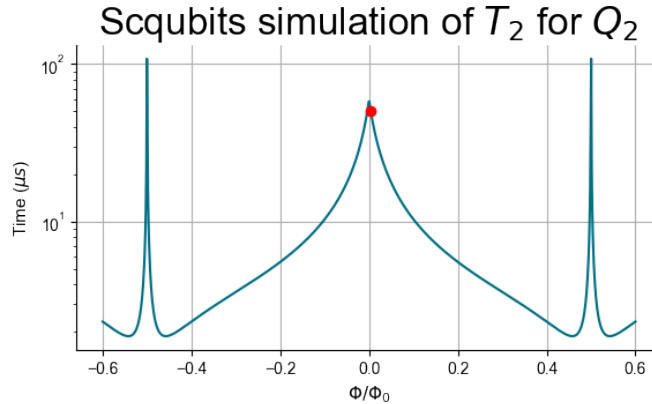


**Figure 60:** *Scqubits* [12] simulation for qubit 2 of the total  $T_2$  as a function of the flux bias in units of the flux quantum. In red, the dephasing times computed for  $\Phi/\Phi_0 = 0.004$ , as in our measurement.

In the end, for state-of-the-art split-transmon qubit, as qubit 2, dephasing can be successfully suppressed by working at the sweet-spot. This result is very important for the implementation of single and two-qubits gate, in which we need the qubit to remain coherent as long as possible.

We repeated the same measurement for qubit 4. In this case, the flux sweet spot is larger than the maximum value of the flux bias that we can apply in our experiment. So, we set the flux as close as possible to the sweet spot, namely at  $\Phi/\Phi_0 = 0.089 \pm 0.001$ .

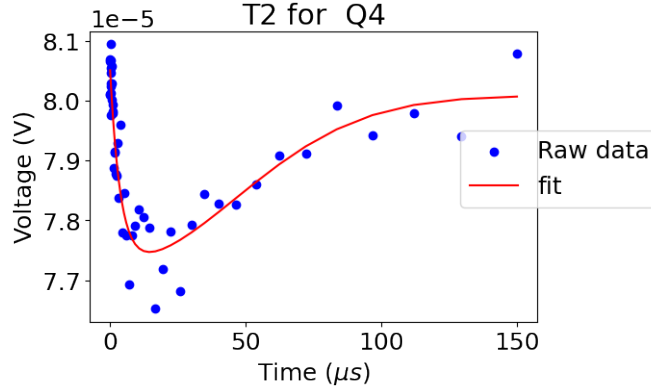


**Figure 61:** Hahn Echo measurement for qubit 4: Gaussian exponential fit (in red) of the voltage magnitude (in blue) for qubit 4 as a function of time.

However, when performing a  $T_2$  Echo measurement on qubit 4 (figure 61), we noted that the decay featured both an exponential and a Gaussian behaviour for small sequence duration times. As discussed in section 3.2, dephasing caused by  $1/f$  flux noise is characterized by a Gaussian decay. Because of this, we performed a fit with a function of the type:  $e^{-t/\tau} e^{-t^2/\sigma^2}$ , as shown in figure 61. The resulting Gaussian and exponential decays are:  $T_{\phi,Gauss} = 65 \pm 11 \mu s$  and  $T_{2,exponential} = 3.7 \pm 0.8 \mu s$ , with statistical errors. This fit shows us that the effective exponential decay time for qubit 4 is smaller than the relaxation time measured in section 5.2.2, thus we are far from the theoretical limit  $T_2 \simeq 2T_1$ . As a matter of fact, for qubit 4, the longitudinal decay is determined by the dephasing time.

From section 3.4, we know that  $T_{\phi}$  is linked to the flux noise amplitude  $A_{\Phi}$ . It can be proved that the Gaussian dephasing time depends on the flux noise amplitude as  $\Gamma_{2,Gauss} = \frac{\sqrt{A_{\Phi/\Phi_0} \ln 2}}{\hbar} \frac{\partial E_{01}}{\partial \Phi/\Phi_0}$  [49], [25]. By using this expression and the Gaussian decay rate measured before, we obtained a noise amplitude of  $A_{\Phi/\Phi_0} = (3 \pm 2) \times 10^{-6}$ . Having performed a simulation of  $T_2$  at this noise amplitude, we obtained a decay time of  $T_2 \simeq 4 \mu s$ , which is consistent with  $T_{2,measured} = 3.7 \pm 0.8 \mu s$ .

## Scqubits simulation of $T_2$ and $T_{\phi, flux}$ for $Q_4$

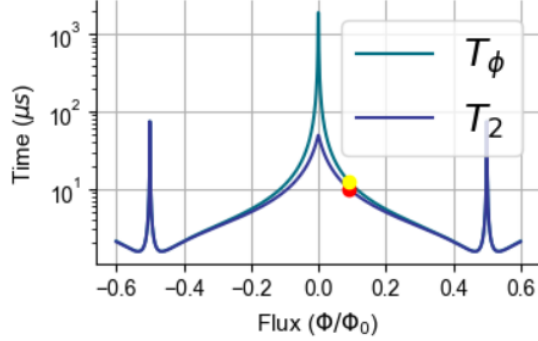


**Figure 62:** *Scqubits* [12] simulation of  $T_2$  (in blue) and  $T_{\phi, flux}$  (in green) for qubit 4 as a function of the flux bias in units of the flux quantum ( $x$ -axis), the red dot is the expected  $T_2$  and the yellow one the expected  $T_{\phi, flux}$  for  $\Phi/\Phi_0 = 0.089$ , as in our measurements.

As we can see from figure 62, the dephasing time due to flux completely dominates the total coherence time behaviour as a function of the flux, and contributes consistently with the values of  $T_2$ . This result shows that, by introducing a noise source in our system, we have drastically changed its coherence times, as described by the Bloch-Redfield model (section 3.1). If we compare the coherence times measured for qubit 2 and qubit 4, we observe that, for the former decoherence is dominated by  $T_1$ , due to dielectric losses only, while for the latter, dephasing introduced by flux noise makes the coherence time  $T_2$  much shorter. In both cases, we used the qubit as a noise detector in order to understand the effect of flux noise and dielectric losses noise. Therefore, the study of noise sources is fundamental to understand the physics behind qubits. Moreover, by identifying the main noise source, in our case the flux in the SQUIDs, one could try to optimize it and improve the qubit performances.

### 5.3 Avoided level crossing as noise spectroscopy

In order to observe  $Q_2 - Q_4$  coupling, it is necessary to performed avoided level crossing measurement, as discussed in section 2.9, by putting them into resonance. As observed in section 5.1.2, we can change the qubit frequency by applying a flux bias. Since qubit 4 has a higher frequency than qubit 2 (table 4), we flux tune its frequency, while qubit 2 is fixed. By performing a flux spectroscopy on qubit 4, as the two frequencies approaches, we observe the avoiding of the energy levels, as shown in figure 63. The eigenstates of the system are a combination of the excited and ground states of each qubit. Because of this, when the two qubits

interact, we observe the appearance of the symmetric  $|\psi_s\rangle$  and asymmetric  $|\psi_a\rangle$  entangled wavefunctions, and finally the excited state  $|ee\rangle$ , as pointed out in section 2.9. Another manifestation of the coherence of the interaction between the two qubits is the observation of dark states [50], i.e. the spectroscopy signal disappears because of destructive interferences. The spectroscopic drive is antisymmetric and therefore unable to drive any transitions to the symmetric state, resulting in a dark state, as we can see from the opening of a gap in the spectrum in figure 63.

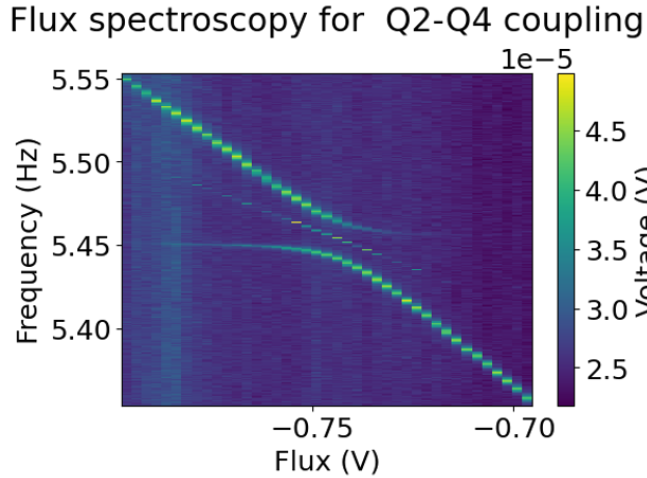


**Figure 63:**  $Q_2$ - $Q_4$  Avoided level crossing: colormap of the voltage magnitude (showed in the color scale) as function of the QD frequency, on the y-axis, and the flux bias, on the x-axis.

As done for the two-tone spectroscopy analysis performed on single qubit 2 and qubit 4, the analysis of the qubit frequency spectrum allows to evaluate the dephasing time of qubit 4 as a function of the flux.

We performed a Lorentzian fit of the qubit spectra to obtain the qubit transition frequencies and the quality factors with *lmfit* [48], based on a function of the type  $(\Gamma/(\Gamma^2+(x-x_0)^2))+(\Gamma^*/(\Gamma^{*2}+(x-x_0^*)^2))$  [51], where  $\Gamma$  and  $\Gamma^*$  are the FWHM of the resonances, and  $x_0$  and  $x_0^*$  are the resonance frequencies. Qubit frequencies as a function of the flux are reported in figure 64 (a). From this measurement, we can evaluate the coupling factor  $J$  between the two qubits (figure 64 (b)), as the energy difference between  $|\psi_s\rangle$  and  $|\psi_a\rangle$ . The measured coupling factor is of the order of tens of MHz, which is consistent with literature examples [23]. The quality factors can be computed as  $Q = x_0/\Gamma$ . As discussed in section 5.1.2, this quality factor is related to the frequency broadening, and thus to the dephasing time as  $T_\phi^* \simeq 2Q/\omega_r$ , reported in figure 64 (c).

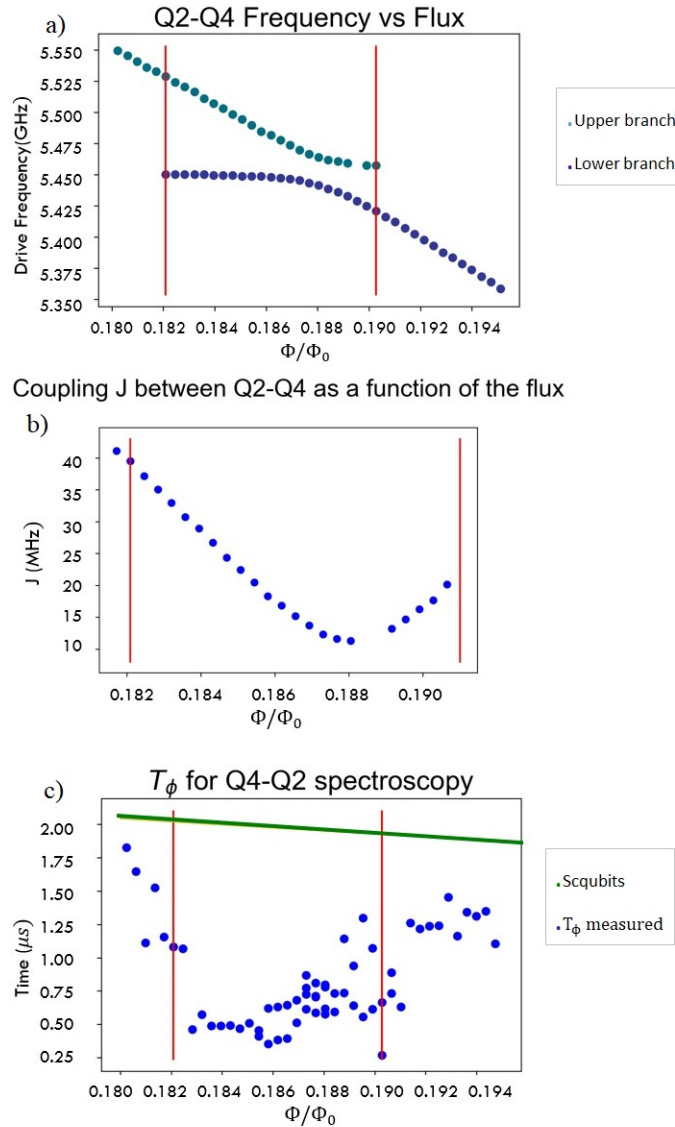


**Figure 64:** a) Extracted resonance frequency (y-axis) as a function of the flux bias in units of the flux quantum (x-axis). b) Coupling parameter  $J$  (y-axis) as a function of the flux (x-axis) in units of the flux quantum. c) Comparison between the measured dephasing times (in blue) and the ones predicted by *scqubits* [12] (in green), as a function of the flux bias on the x-axis in units of the flux quantum. The red lines indicate the beginning of the interaction, and the final acquired flux point.

During the coupling, the coherence properties of qubit 4 do not follow the B-R model. Instead of a standard  $1/f$  dependence on flux predicted by the *scqubits*

[12] simulation (figure 64 (c) in green), we observe that the dephasing time shows a sudden drop close to the avoided level crossing (the blue points in figure 64 (c)). Moreover, from figure 64 (c), we note that the slope of the simulated  $T_\phi$  is less pronounced compared to the experimental data. This comparison could suggest that the flux noise power spectral density may depend on the frequency as  $S(\omega) \propto 1/\omega^\nu$ , with  $\nu$  different from 1. In literature, it has been demonstrated that possible values for  $\nu$  may range from 0.8 to 1 [7].

This analysis shows us that the coherence properties of a single-qubit can be rightfully described with a two level system model as discussed in section 3.1, but drastically change when we consider a two-qubit system, in which the qubit states are mixed, and the B-R model fails. This highlights the importance of the study of the main fundamental noise-fluctuations mechanisms in superconducting quantum circuits.

## 6 Conclusions

Throughout this work, we have described Josephson-based superconducting qubits, with a specific focus on transmon qubits. We have investigated the effect of noise on transmon devices from an experimental point of view, and we compared our data within well-known theoretical models for decoherence mechanisms in superconducting transmon devices. We pointed out experimental protocols for the study of the decoherence mechanisms in a state-of-the-art device, such as relaxation time  $T_1$  measurements, Ramsey interferometry, and  $T_2$  Hahn Echo. By performing these measurements, we compared these results with the theoretical predictions obtained with the python library *scqubits* [12].

This self-consistent analysis highlighted that the most relevant noise sources for the device analyzed in this work, within a joint experiment between Quantware, Seeqc-EU and the University of Napoli Federico II, were: the dielectric losses for relaxation, and the flux bias for dephasing, particularly relevant far from the flux sweet-spots. Specifically speaking, Hahn-echo measurements, characterized by a Gaussian decay, rather than a pure exponential decay, have been compared with the theoretical simulations of dephasing times in order to extract the amplitude of flux noise, providing a consistent and comparative way to extract information on the flux noise. This self-consistent method for the noise characterization of a single split-transmon allows to identify, on a certain extent, the main decoherence sources by using the qubit as a noise detector.

Finally, we have investigated on the decoherence processes occurring in a two-qubit system, and we have experimentally observed that the dephasing time of the qubits decreases during the coupling. This behaviour can be explained with the fact that, by coupling the qubits, other sources of decoherence and dissipation arise. In addition, the behaviour of the measured dephasing time as a function of the flux was not consistent with a  $1/f$  dependency of the power spectral density for flux noise.

The evaluation of the exact low-frequency dependence of noise power spectral densities is of immeasurable importance, in order to understand the microscopic and quantum nature of the noise in superconducting qubits. Therefore, my study confirms the need of developing novel simulation tools for the study of decoherence mechanisms in superconducting qubits. The extension to multi-qubit systems dynamics is a mandatory step for advances in the understanding of such phenomena in scalable superconducting quantum processors. Moreover, the results provided in this work are of fundamental importance for the engineering of the transmon qubit design. Once the most relevant noise sources are identified, in our case dielectric losses and flux noise, they can be minimized by searching for novel materials, fabrication conditions and circuit design.

## References

- [1] Göran Wendin. Quantum information processing with superconducting circuits: a review. *Reports on Progress in Physics*, 80(10):106001, 2017.
- [2] Ivan Kassal, James D. Whitfield, Alejandro Perdomo-Ortiz, Man-Hong Yung, and Alán Aspuru-Guzik. Simulating chemistry using quantum computers. *Annual review of physical chemistry*, 62:185–207, 2011.
- [3] C.H. Ugwuishiwu, U.E Orji, C.I. Ugwu, and C.N. Asogwa. An overview of quantum cryptography and shor’s algorithm. *Int. J. Adv. Trends Comput. Sci. Eng*, 9(5), 2020.
- [4] Christopher Portmann and Renato Renner. Security in quantum cryptography. *Reviews of Modern Physics*, 94(2):025008, 2022.
- [5] Dylan Herman, Cody Googin, Xiaoyuan Liu, Alexey Galda, Ilya Safro, Yue Sun, Marco Pistoia, and Yuri Alexeev. A survey of quantum computing for finance. *arXiv preprint arXiv:2201.02773*, 2022.
- [6] Claude Cohen-Tannoudji, Bernard Diu, and Frank Laloe. Quantum mechanics, volume 2. *Quantum Mechanics*, 2:626, 1986.
- [7] Philip Krantz, Morten Kjaergaard, Fei Yan, Terry P. Orlando, Simon Gustavsson, and William D. Oliver. A quantum engineer’s guide to superconducting qubits. *Applied Physics Reviews*, 6(2):021318, 2019.
- [8] Elizabeth Gibney. Hello quantum world! google publishes landmark quantum supremacy claim. *Nature*, 574(7779):461–463, 2019.
- [9] Diogo Cruz, Romain Fournier, Fabien Gremion, Alix Jeannerot, Kenichi Komagata, Tara Tasic, Jarla Thiesbrummel, Chun Lam Chan, Nicolas Macris, Marc-André Dupertuis, et al. Efficient quantum algorithms for ghz and w states, and implementation on the ibm quantum computer. *Advanced Quantum Technologies*, 2(5-6):1900015, 2019.
- [10] Antonio Barone and Gianfranco Paternò. Josephson effects: Basic concepts. In *Advances in Superconductivity*, pages 183–195. Springer, 1983.
- [11] Jens Koch, M. Yu Terri, Jay Gambetta, Andrew A. Houck, David I. Schuster, Johannes Majer, Alexandre Blais, Michel H. Devoret, Steven M. Girvin, and Robert J. Schoelkopf. Charge-insensitive qubit design derived from the cooper pair box. *Physical Review A*, 76(4):042319, 2007.

- [12] Peter Groszkowski and Jens Koch. Scqubits: a python package for superconducting qubits. *Quantum*, 5:583, 2021.
- [13] Anton Frisk Kockum and Franco Nori. Quantum bits with josephson junctions. In *Fundamentals and Frontiers of the Josephson Effect*, pages 703–741. Springer, 2019.
- [14] Michael Tinkham. *Introduction to superconductivity*. Courier Corporation, 2004.
- [15] John Bardeen, Leon N. Cooper, and John Robert Schrieffer. Theory of superconductivity. *Physical review*, 108(5):1175, 1957.
- [16] HMAR Maruf, M.R. Islam, and FUZ Chowdhury. Analogy between ac josephson junction effects and optical phenomena in superconductors. *Bangladesh Journal of Physics*, 23:105–113, 2018.
- [17] Francesco Tafuri. *Fundamentals and frontiers of the Josephson effect*, volume 286. Springer Nature, 2019.
- [18] Konstantin K. Likharev. *Dynamics of Josephson junctions and circuits*. Routledge, 2022.
- [19] Yang Gao, Xi Gao, Jie Ren, Siqi Li, Xue Zhang, Hui Zhang, Qian Lin, Minghui Niu, Weifeng Shi, Liliang Ying, et al. Josephson junction parameters extraction method for the rclsj model. *Physica C: Superconductivity and its Applications*, page 1354076, 2022.
- [20] D. Massarotti, Niladri Banerjee, R. Caruso, G. Rotoli, M.G. Blamire, and F. Tafuri. Electrodynamics of josephson junctions containing strong ferromagnets. *Physical Review B*, 98(14):144516, 2018.
- [21] Jean Frederic Isingizwe Nturambirwe. Superconducting quantum interference device (squid) magnetometers: Principles, fabrication and applications. *Postgraduate diploma assay*, May, 2010.
- [22] Kunihiro Inomata, Tsuyoshi Yamamoto, P.M. Billangeon, Y. Nakamura, and J.S. Tsai. Large dispersive shift of cavity resonance induced by a superconducting flux qubit in the straddling regime. *Physical Review B*, 86(14):140508, 2012.
- [23] S. Filipp, M. Göppl, J.M. Fink, M. Baur, R. Bianchetti, L. Steffen, and A. Wallraff. Multi-mode mediated exchange coupling in cavity qed. *arXiv preprint arXiv:1011.3732*, 2010.

- [24] R.J. Schoelkopf, A.A. Clerk, S.M. Girvin, K.W. Lehnert, and M.H. Devoret. Qubits as spectrometers of quantum noise. In *Quantum noise in mesoscopic physics*, pages 175–203. Springer, 2003.
- [25] G. Ithier, E. Collin, P. Joyez, P.J. Meeson, Denis Vion, Daniel Esteve, F. Chiarello, A. Shnirman, Yu Makhlin, Josef Schrieffer, et al. Decoherence in a superconducting quantum bit circuit. *Physical Review B*, 72(13):134519, 2005.
- [26] Long B. Nguyen, Yen-Hsiang Lin, Aaron Somoroff, Raymond Mencia, Nicholas Grabon, and Vladimir E. Manucharyan. High-coherence fluxonium qubit. *Physical Review X*, 9(4):041041, 2019.
- [27] W.C. Smith, A. Kou, X. Xiao, U. Vool, and M.H. Devoret. Superconducting circuit protected by two-cooper-pair tunneling. *npj Quantum Information*, 6(1):1–9, 2020.
- [28] S.E. Rasmussen, K.S. Christensen, S.P. Pedersen, L.B. Kristensen, T. Bækkegaard, N.J.S. Loft, and N.T. Zinner. Superconducting circuit companion—an introduction with worked examples. *PRX Quantum*, 2(4):040204, 2021.
- [29] Martin Göppl, A. Fragner, M. Baur, R. Bianchetti, Stefan Filipp, Johannes M. Fink, Peter J. Leek, G. Puebla, L. Steffen, and Andreas Wallraff. Coplanar waveguide resonators for circuit quantum electrodynamics. *Journal of Applied Physics*, 104(11):113904, 2008.
- [30] Sebastian Probst, F.B. Song, Pavel A. Bushev, Alexey V. Ustinov, and Martin Weides. Efficient and robust analysis of complex scattering data under noise in microwave resonators. *Review of Scientific Instruments*, 86(2):024706, 2015.
- [31] J. Verjauw, A. Potočnik, M. Mongillo, R. Acharya, F. Mohiyaddin, G. Simion, A. Pacco, Ts. Ivanov, D. Wan, A. Vanleenhove, et al. Investigation of microwave loss induced by oxide regrowth in high-q niobium resonators. *Physical Review Applied*, 16(1):014018, 2021.
- [32] Guofeng Chen and Matteo Rinaldi. High-q x band aluminum nitride combined overtone resonators. In *2019 Joint Conference of the IEEE International Frequency Control Symposium and European Frequency and Time Forum (EFTF/IFC)*, pages 1–3. IEEE, 2019.

- [33] Q. He, P. OuYang, H. Gao, S. He, Y. Li, Y. Wang, Y. Chen, X. Dai, and L.F. Wei. Low-loss superconducting aluminum microwave coplanar waveguide resonators on sapphires for the qubit readouts. *Superconductor Science and Technology*, 35(6):065017, 2022.
- [34] Joel I-Jan Wang, Daniel Rodan-Legrain, Landry Bretheau, Daniel L. Campbell, Bharath Kannan, David Kim, Morten Kjaergaard, Philip Krantz, Gabriel O. Samach, Fei Yan, et al. Coherent control of a hybrid superconducting circuit made with graphene-based van der waals heterostructures. *Nature nanotechnology*, 14(2):120–125, 2019.
- [35] Martin A. Wolff, Lukas Splitthoff, Thomas Grottke, Simon Vogel, and Carsten Schuck. Nanophotonic tantalum pentoxide devices for integrated quantum technology. In *2020 Conference on Lasers and Electro-Optics (CLEO)*, pages 1–2. IEEE, 2020.
- [36] Gianluigi Catelani, Robert J. Schoelkopf, Michel H. Devoret, and Leonid I. Glazman. Relaxation and frequency shifts induced by quasiparticles in superconducting qubits. *Physical Review B*, 84(6):064517, 2011.
- [37] R.M. Lutchyn, L.I. Glazman, and A.I. Larkin. Kinetics of the superconducting charge qubit in the presence of a quasiparticle. *Physical Review B*, 74(6):064515, 2006.
- [38] Rolf Landauer. Spatial variation of currents and fields due to localized scatterers in metallic conduction. *IBM Journal of research and development*, 1(3):223–231, 1957.
- [39] Richard Versluis, Stefano Poletto, Nader Khammassi, Brian Tarasinski, Nadia Haider, David J. Michalak, Alessandro Bruno, Koen Bertels, and Leonardo DiCarlo. Scalable quantum circuit and control for a superconducting surface code. *Physical Review Applied*, 8(3):034021, 2017.
- [40] BF-LD-Series.
- [41] LNF-PBA Datasheet.
- [42] LNF-LNC48CDatasheet.
- [43] Keysight M3202A AWG.
- [44] Labber.

- [45] Hanhee Paik, David I. Schuster, Lev S. Bishop, Gerhard Kirchmair, Gianluigi Catelani, Adam P. Sears, B.R. Johnson, M.J. Reagor, Luigi Frunzio, Leonid I. Glazman, et al. Observation of high coherence in josephson junction qubits measured in a three-dimensional circuit qed architecture. *Physical Review Letters*, 107(24):240501, 2011.
- [46] Qutip.
- [47] Resonator tools.
- [48] Non-Linear Least-Squares Minimization and Curve fitting.
- [49] F. Yoshihara, K. Harrabi, A.O. Niskanen, Y. Nakamura, and Jaw Shen Tsai. Decoherence of flux qubits due to  $1/f$  flux noise. *Physical review letters*, 97(16):167001, 2006.
- [50] Johannes Majer, J.M. Chow, J.M. Gambetta, Jens Koch, B.R. Johnson, J.A. Schreier, L. Frunzio, D.I. Schuster, Andrew Addison Houck, Andreas Wallraff, et al. Coupling superconducting qubits via a cavity bus. *Nature*, 449(7161):443–447, 2007.
- [51] Ziyang Zhang, Matteo Dainese, Lech Wosinski, and Min Qiu. Resonance-splitting and enhanced notch depth in soi ring resonators with mutual mode coupling. *Optics express*, 16(7):4621–4630, 2008.
- [52] M.D. Hutchings, Jared B. Hertzberg, Yebin Liu, Nicholas T. Bronn, George A. Keefe, Markus Brink, Jerry M. Chow, and B.L.T. Plourde. Tunable superconducting qubits with flux-independent coherence. *Physical Review Applied*, 8(4):044003, 2017.
- [53] Gerd Hammer, Stefan Wuensch, Markus Roesch, Konstantin Ilin, Erich Croll, and Michael Siegel. Coupling of microwave resonators to feed lines. *IEEE transactions on applied superconductivity*, 19(3):565–569, 2009.
- [54] Tzyy-Jiann Wang, Po-Kuang Chen, Yan-Ting Li, and An-Ni Sung. Athermal high-q tantalum-pentoxide-based microresonators on silicon substrates. *Optics & Laser Technology*, 138:106925, 2021.
- [55] Fumiki Yoshihara, Yasunobu Nakamura, Fei Yan, Simon Gustavsson, Jonas Bylander, William D Oliver, and Jaw-Shen Tsai. Flux qubit noise spectroscopy using rabi oscillations under strong driving conditions. *Physical Review B*, 89(2):020503, 2014.

- [56] Jonas Bylander, Simon Gustavsson, Fei Yan, Fumiki Yoshihara, Khalil Harrabi, George Fitch, David G. Cory, Yasunobu Nakamura, Jaw-Shen Tsai, and William D. Oliver. Noise spectroscopy through dynamical decoupling with a superconducting flux qubit. *Nature Physics*, 7(7):565–570, 2011.
- [57] Richard P. Feynman, Tony Hey, and Robin W. Allen. *Feynman lectures on computation*. CRC Press, 2018.
- [58] Walther Meissner and Robert Ochsenfeld. Ein neuer effekt bei eintritt der supraleitfähigkeit. *Naturwissenschaften*, 21(44):787–788, 1933.
- [59] S.M. Anton, Clemens Müller, J.S. Birenbaum, S.R. O’Kelley, A.D. Fefferman, Dmitri S. Golubev, G.C. Hilton, H-M Cho, K.D. Irwin, Frederick C. Wellstood, et al. Pure dephasing in flux qubits due to flux noise with spectral density scaling as  $1/f^\alpha$ . *Physical Review B*, 85(22):224505, 2012.
- [60] P. Kumar, S. Sendelbach, M.A. Beck, J.W. Freeland, Zhe Wang, Hui Wang, C. Yu Clare, R.Q. Wu, D.P. Pappas, and R. McDermott. Origin and reduction of  $1/f$  magnetic flux noise in superconducting devices. *Physical Review Applied*, 6(4):041001, 2016.
- [61] W.C. Stewart. Current-voltage characteristics of josephson junctions. *Applied physics letters*, 12(8):277–280, 1968.
- [62] Sourav Biswas. *Phase Dynamic Regime in  $\mu$ -SQUIDs & Its Optimization for Probing Nanomagnetism*. PhD thesis, Indian Institute of Technology Kanpur, 2019.